Kondo and magnetic sublattices in Ce compounds - a spectroscopic X-ray study

Georg Poelchen

To cite this version:

Georg Poelchen. Kondo and magnetic sublattices in Ce compounds - a spectroscopic X-ray study. Physics [physics]. Université Grenoble Alpes [2020-..], 2022. English. NNT : 2022GRALY071 . tel-04114473

HAL Id: tel-04114473
https://theses.hal.science/tel-04114473v1

Submitted on 2 Jun 2023

THÈSE

Pour obtenir le grade de

DOCTEUR DE L'UNIVERSITÉ GRENOBLE ALPES

École doctorale : PHYS - Physique
Spécialité : Physique de la Matière Condensée et du Rayonnement
Unité de recherche : European Synchrotron Radiation Facility

Kondo et sous-réseaux magnétiques dans les composés du Ce - une étude spectroscopique aux rayons X

Kondo and magnetic sublattices in Ce compounds - a spectroscopic X-ray study

Présentée par :

Georg POELCHEN

Direction de thèse :

Nicholas BROOKES European Synchrotron Radiation Facility	Directeur de thèse
Kurt KUMMER European Synchrotron Radiation Facility	Co-encadrant de thèse

Rapporteurs :

Sébastien BURDIN
Maître de conférences HDR, Université de Bordeaux
Claudia DALLERA
Professeur associé, Politecnico di Milano

Thèse soutenue publiquement le **29 novembre 2022**, devant le jury composé de :

Olivier ISNARD Professeur des Universités, Université Grenoble Alpes	Président
Sébastien BURDIN Maître de conférences HDR, Université de Bordeaux	Rapporteur
Claudia DALLERA Professeur associé, Politecnico di Milano	Rapporteure
Marco GRIONI Professeur associé, Ecole Polytechnique Fédérale de Lausanne	Examinateur
Amélie JUHIN Directeur de recherche, CNRS - Délégation Paris-Centre	Examinatrice
Clemens LAUBSCHAT Professeur, Technische Universität Dresdenn	Examinateur

Résumé

Ce travail de thèse présente des études menées sur $CeRh_2Si_2$ et $CeCo_2P_2$, deux composés intermétalliques à base de Cérium , par spectroscopie d'absorption, d'émission photoélectrique et de diffusion inélastique résonante de rayons X issus du rayonnement synchrotron, en combinaison avec des calculs ab-initio de structure de bande. En étudiant les effets de différentes terminaisons de surface, ces mesures nous permettent une meilleure compréhension et interprétation de la physique du Cérium $4f$, sensible aux effets de surface et combinée au magnétisme du cobalt en volume.

Dans la première étude présentée, la dépendance en température des réponses spectrales du Ce $4f$ en surface et en volume a été explorée par spectroscopie de photoémission résolue en angle (ARPES) dans le réseau Kondo antiferromagnétique $CeRh_2Si_2$. Des schémas $4f$ caractéristiques d'une hybridation faible (à la surface) et forte (en volume) ont été mis en évidence par l'étude des spectres des surfaces terminées par du Ce et du Si dans une large gamme de température. La dépendance en température du pic associé au niveau de Fermi diffère fortement pour ces deux terminaisons, ce qui suggère une différence significative de la température de Kondo en surface et en volume. Cette différence pourrait s'expliquer par une levée de dégénérescence du champ cristallin fortement réduite à la surface, entraînant une température de Kondo effective plus élevée résultant d'une dégénérescence effective accrue du moment local. De plus, des forces d'hybridation différentes pourraient jouer sur les intensités du pic $4f$ au niveau de Fermi. La possibilité de mesurer des surfaces bien distinctes ouvre ainsi la voie pour directement tester de manière quantitative les théories à N-corps qui lient la spectroscopie et les propriétés de transport, en volume et en surface séparément.

Contrairement au $CeRh_2Si_2$, le composé $CeCo_2P_2$ ne montre aucun signe dans son volume de la physique des fermions lourds. Mais nos mesures de photoémission résolue en angle, qui sont sensibles à la surface, suggèrent que la physique des 4f change considérablement proche de la surface. Nous proposons que cela soit directement lié à la brisure de symétrie du sous-réseau du cobalt ordonné antiferromagnétiquement, entraînant l'apparition d'un champ magnétique effectif créant des états Ce $4f$ partiellement occupés polarisés en spin proches de la surface. Les mesures en température indiquent des variations importantes de l'intensité des $4f$ au niveau de Fermi, compatibles avec un scénario de type Kondo.

A la surface, l'interaction particulière entre les sous-réseaux du cobalt $3d$ magnétique et du Ce $4f$ mène à la physique des fermions lourds, alors que l'absence totale de physique des moments localisés $4f$ loin de la surface se traduit par une densité d'états réduite au niveau de Fermi dans le volume. Habituellement dans les composés métalliques, la durée de vie des magnons de haute fréquence est fortement réduite par les interactions avec le continuum de Stoner. Cependant, de par cette densité réduite dans le volume, les magnons du sous-réseau de cobalt

du composé $CeCo_2P_2$ subsistent jusque dans le régime du térahertz. Plus précisément, nos calculs ab-initio prédisent une suppression des excitations Stoner de basse énergie, ce que nous avons vérifié expérimentalement par diffusion inélastique résonante de rayons X. Par comparaison, le comportement typique de magnon fortement amorti observé habituellement dans les systèmes métalliques se retrouve dans le composé à structure identique $LaCo_2P_2$. Sur la base de ces observations, nous proposons le système La/$CeCo_2P_2$ comme un candidat potentiel pour des études plus poussées en vue d'aboutir à des dispositifs métalliques quantiques magnoniques.

Summary

In this work, the two different Ce-based intermetallic compounds $CeRh_2Si_2$ and $CeCo_2P_2$ have been studied by means of synchrotron radiation spectroscopic (X-ray absorption and photoelectron emission spectroscopy) and resonant inelastic X-ray scattering methods in combination with ab-initio band structure calculations. The measurements allowed for an improved understanding and interpretation of surface sensitive Ce-$4f$ physics by studying distinct surface terminations and their effects, while being combined in the bulk with Co $3d$ magnetism.

In the first presented study, angle-resolved photoemission spectroscopy (ARPES) was used to explore the temperature dependence of the Ce-$4f$ spectral responses for surface and bulk in the antiferromagnetic Kondo lattice $CeRh_2Si_2$. Distinct spectra from the Ce- and Si-terminated surfaces were studied in a wide temperature range revealing characteristic $4f$ patterns for weakly (surface) and strongly (bulk) hybridized Ce, respectively. The terminations exhibit different temperature dependences of the Fermi level peak suggesting that the effective Kondo temperatures at the surface and in the bulk differ significantly. The origin of this difference might lie in a greatly reduced crystal–electric-field (CEF) splitting at the surface resulting in a larger effective Kondo temperature due to a higher local-moment effective degeneracy. Additionally, different hybridization strengths could further influence the $4f$ peak intensities at the Fermi level. The possibility of measuring distinct surfaces lays the foundation for directly testing quantitatively many-body theories that link spectroscopy and transport properties for both the bulk and the surface, separately.

In contrast to $CeRh_2Si_2$, the $CeCo_2P_2$ compound shows no signs of heavy-fermion physics in the bulk. But our surface sensitive angle-resolved photoemission measurements suggest that the $4f$ physics significantly change near the surface. We propose that this is a direct result of the symmetry breaking of the antiferromagnetically ordered cobalt sublattice resulting in an effective magnetic field which in turn leads to partially occupied and spin-polarized Ce $4f$ states near the surface. The temperature-dependent measurements reveal strong changes of the $4f$ intensity at the Fermi level in accordance with the Kondo scenario.

At the surface, the particular interplay between the magnetic Co $3d$ and the Ce $4f$ sublattice leads to heavy-fermion physics, while the complete absence of local-moment $4f$ physics away from the surface region results in a reduced density of states at the Fermi level in the bulk. Usually, in metallic compounds the lifetime of high-frequency magnons is strongly reduced due to interactions with the Stoner continuum, however, due to the reduced density in the bulk, long-living magnons on the Co sublattice of $CeCo_2P_2$ can exist up to the terahertz regime. In detail, our first-principle calculations predict a suppression of low-energy spin-flip Stoner excitations, which we experimentally verified by resonant inelastic X-ray scattering measurements. In comparison, the isostructural $LaCo_2P_2$ compound exhibits the typical strongly damped magnon behavior usually observed in metallic systems. Based on these observations, we propose the La/$CeCo_2P_2$ system as a suitable

candidate for further studies on the way to metallic magnonic quantum devices.

Contents

1 Introduction

> "H. Suhl has been heard to say that no Hamiltonian so incredibly simple has ever previously done such violence to the literature and to national science budgets."
>
> — *P. W. Anderson about the impurity Anderson model, Nobel lecture [1]*

In solids under normal conditions, the most influential and important electrons are the weakly-bound valence electrons which are responsible for the transport and thermodynamic properties due to their low-energy excitations. However, a macroscopic system usually contains valence electrons in the order of at least 10^{22}, which makes the study of the interacting system impossible. In spite of this, many solid systems can be well described theoretically by considering the electrons in a sea of non-interacting particles. But this picture breaks down when each electron has a complex influence on its neighbors that cannot be described anymore by a mean field theory. These so called strong correlations are responsible for a large number of fascinating (and also technologically useful) electronic and magnetic phases ranging form metal-insulator transitions and high-temperature superconductivity to heavy-fermion physics and complex magnetic structures [2].

One famous effect, where strong correlations play an important role, is the so called Kondo effect, which describe the increase in the resistivity for very low temperatures due to scattering at magnetic impurities [3]. This effect was first observed in gold samples which contained magnetic impurities in 1934 [4]. The correlations are an effect of incompletely filled $3d$ or $4f$ shells where the on-site Coulomb repulsion is large in comparison to the kinetic energy and band width.

In the following, the focus will be on systems with an incompletely filled $4f$ shell, the so called lanthanides Ln (also called rare-earth or $4f$ elements) [5], where the $4f$ shell is increasingly filled starting from lanthanum to lutetium. The special properties of the $4f$ shell become apparent when considering the radial density of the $4f$ shell as shown in Figure 1.1 [6]. In comparison to the $n = 5$ and $n = 6$ shells, the $4f$ shell is strongly localized closed to the core and thus contains a strong atomic character. Thus, a partial filling of this $4f$ shell can give rise to a huge magnetic moment, which, in combination with other elements, is used for instance in permanent magnets like in the famous neodymium-iron-boron alloys [7]. On the other hand, when two different $4f$ configurations are close in energy as it is the case for the configurations close to empty, half-filled or completely filled $4f$ shells, then low energy excitations and hybridizations can lead to different phases and a competition between magnetic order and Kondo screening.

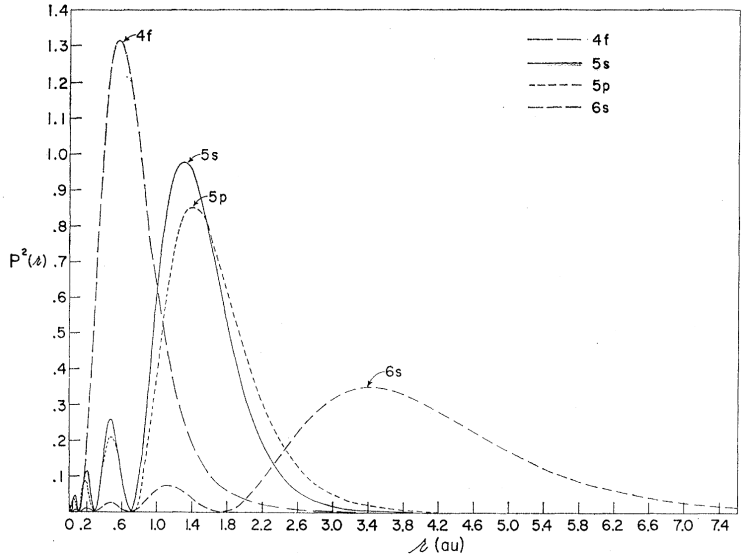

Figure 1.1: Radial charge density of $P^2(r)$ with respect to r for Gd$^+$ based on Hartree-Fock calculations [6].

Thus, the seemingly simple case of a single $4f$ electron of Ce^{3+} becomes complicated, which makes Ce-based compounds a work horse to explore the influence of strong electron correlations [8]. Most of these intermetallic systems contain Ce in a mixed-valent state close to the trivalent configuration Ce $4f^1(5d6s)^3$ with possible contributions from the $4f^0(5d6s)^4$ and $4f^2(5d6s)^2$ configuration. While the $4f$ double occupancy is highly unfavorable due to the strong Coulomb repulsion and thus its contribution typically small, the tetravalent $4f^0$ configuration lies energetically close to the Ce $4f^1$. The magnetic properties are thus influenced by the competition between the non-magnetic $4f^0$ and the $4f^1$ ($J = 5/2$) configuration.

Early experiments indeed showed such an instability when studying Ce under pressure. This well-known Ce $\gamma - \alpha$ transition, first interpreted as valency change [9], can be seen in the Kondo volume collapse picture as transition from localized (γ) to a band-like itinerant (α) Ce [10–12]. After the first observation of heavy-fermion behavior [13], photoemission spectroscopy became an important tool to study Ce based materials since it probes the spectral function. With the advent of angle-resolved photoemission spectroscopy (ARPES), k-resolved measurements and measurements of the Fermi surface became possible. In the same way our theoretical understanding improved with new models and more feasible dynamical mean field theory (DMFT) calculations [14]. However, for real systems, direct comparisons between theory and measurements remain in many cases still challenging due to additional effects like crystal-electric-field splittings, spin-orbit couplings, lattice relaxations and surface effects, while additionally very low temperatures are commonly not reachable for dense Kondo lattices with DMFT. Even more challenging and interesting are the interaction of different local-moment Kondo or magnetic sublattices.

But another big obstacle in many photoemission measurements is the missing knowledge about the surface properties. For the very soft X-ray regime (also called vacuum ultra violet regime), the measurements are very sensitive to surface effects and thus relaxations, terminations and surface states can strongly influence the taken spectra. Our study on $CeRh_2Si_2$ shows how different surface terminations can show different $4f$ physics, while our study on $CeCo_2P_2$ nicely presents how the properties close to the surface can strongly differ from the bulk properties. While at the surface of $CeCo_2P_2$ both magnetism on the Co as well as local moments on the Ce exist, the bulk exhibits only Co magnetism. Using resonant inelastic X-ray scattering (RIXS) measurements, the spin excitations on the Co sublattice were studied.

In the next chapter (Chapter 2), the basic concepts of the atomic electron structure and band structure are discussed. Additionally, both the density functional theory as well as the model Hamiltonians of the impurity Anderson model and Heisenberg model and their respective connections to the heavy-fermions and magnons are introduced. However, all introductions are brief and will be focused only on the parts essential for this thesis.

After that, Chapter 3 will give a short overview on the used spectroscopic and scattering methods starting from X-ray absorption spectroscopy, then discussing ARPES and finally given a brief introduction to RIXS.

The main Chapter 4 will present our results based on our ARPES measurements for $CeRh_2Si_2$ and $CeCo_2P_2$. After a short introduction on photoemission measurements on Ce-based compounds, the measurements and discussion of $CeRh_2Si_2$ will be presented and followed by the $CeCo_2P_2$ surface study combining ARPES, X-ray dichroism and density functional theory (DFT) calculations. After considering the surface of $CeCo_2P_2$, Chapter 5 will discuss the spin excitations in the bulk. For comparison, the results will be presented together with our measurements of the isostructural $LaCo_2P_2$. Finally, Chapter 6 will give a combined summary and outlook.

2 Fundamental concepts

This chapter is devoted to the presentation of a number of important concepts and theoretical descriptions which form the basis of the performed studies.

2.1 Atomic orbitals and many-body physics

The basis of solid state physics is the quantum mechanical description of the system by considering the eigenvalue problem of the Hamilton H, called Schrödinger equation [15, 16],

$$H\psi_N = E_N\psi_N \tag{2.1}$$

where ψ_N and E_N are the many-body wave functions and energies. The Hamiltonian H can generally written in the non-relativistic form

$$\begin{aligned} H =& T_e + T_n + V_{e-e} + V_{n-n} + V_{e-n} && (2.2) \\ =& \sum_{i=1}^{N_e} \frac{-\hbar^2}{2m_e}\nabla^2_{r_i} + \sum_{j=1}^{N_n} \frac{-\hbar^2}{2m_n}\nabla^2_{R_j} + \sum_{k,l,k\neq l} \frac{1}{2}\frac{e^2}{|r_k - r_l|} && \\ &+ \sum_{m,n,m\neq n} \frac{1}{2}\frac{Z_m Z_n e^2}{|R_m - R_n|} + \sum_{p,q,p\neq q} -\frac{1}{2}\frac{Z_p e^2}{|R_p - r_q|} && (2.3) \end{aligned}$$

where T_e and T_n are the kinetic energies for electrons and nuclei while V_{e-e}, V_{n-n} and V_{e-n} are the Coulomb interactions for electrons, nuclei and electron-nucleus interaction. In the explicitly written form, the electrons are described by their positions r_i, mass m_e and charge $-e$ and the nuclei by R_i, m_n and their charge $Z_i e$. For the study of the electronic structure, the movement of the nuclei can usually assumed to be fixed in the time scale of the electrons. This so called Born-Oppenheimer approximation [17] simplifies the many-body Hamiltonian which then only contains the decoupled electronic problem.

Famously, this Hamiltonian is not solvable for a system with more than one electron and has thus lead to the large development of different methods to circumvent this problem. In general, these methods can be differentiated into two different approaches. First, one can replace the Hamiltonian H by a model Hamiltonian designed to treat a specific problem of interest. In Section 2.4 the Anderson impurity model will be discussed which can successfully describe the electronic structure of strongly correlated electrons, while in Section 2.5 the Heisenberg Hamiltonian will be used as basis for introducing spin waves. In the second approach, one tries to neglect and simplify certain contributions to H and the many-body wave function ψ_N starting from Equation (2.2). Using the Hartree approximation, the many-body wave function is rewritten as product function of the single-particle wavefunctions [18, 19]. Using a Slater determinant, an antisymmetrization of the approximated many-body wave function can be achieved and solved by an self-consistent iteration scheme yielding the Hartree-Fock wave functions of the system [20]. For the treatment of electron correlations, a linear combination of Slater determinants is possible leading to the so called configuration interaction method [21]. And in the density functional theory, the electron density alone will be varied to determine the ground state by approximating the exchange correlation potential as discussed in Section 2.3.

However, before discussing the interaction of multiple atoms in a crystal, let us first shortly refresh the properties of a single atom. Starting from Equation (2.2), the atomic Hamiltonian H for N electrons of mass m and charge $-e$ in the rest frame of the nucleus with charge Ze can be written as

$$H = \sum_{i=1}^{N} \frac{-\hbar^2}{2m}\nabla^2 - \frac{Ze^2}{r_i} + \xi(r_i)\vec{l}_i \cdot \vec{s}_i + \sum_{i \neq j} \frac{1}{2} \frac{e^2}{|r_i - r_j|} \tag{2.4}$$

where the spin-orbit interaction is included as $\xi(r_i)\vec{l}_i \cdot \vec{s}_i$, but the hyper fine interaction with the nucleus neglected [22]. To get a single-particle Hamiltonian h_i, the electrons are treated as moving interdependently in a radial field $V_{\text{rad}}(r_i)$ which approximates both the repulsion and the screening of the nucleus by the other electrons while any additional terms can be treated later perturbatively (i.e. spin-orbit interaction). This so called central field approximation [23] leads to independent single-electron wave functions ψ^i, where the radial and angular parts can be separated $\psi^i_{nlm_l} = R^i_{nl} Y^i_{lm_l}$. Here, the nlm_l are the indices which describe the state ψ and are usually called principal quantum number n, orbital (angular momentum) quantum number l and magnetic quantum number m_l while Y_{lm_l} is a spherical harmonic. Since $V_{\text{rad}}(r_i)$ is a radial field, all m_l states are degenerate for the same n and l. Lastly, the spin which so far has been ignored, needs to be added by multiplication with the the spin functions with quantum numbers $m_s = \pm\frac{1}{2}$. These quantum numbers form the basis for the description of the electronic states and specify the electronic configuration of the system.

Including now electrostatic and spin-orbit interactions as first-order correction yields an additional split of the electronic configuration into levels. For simplicity, we consider only the Russell-Saunders (or LS) coupling here where the spin-orbit coupling is weak in comparison to the couplings between spins or orbital angular momenta, the corresponding many-body wave function are characterized by the quantum numbers $L = \sum m_l$, $S = \sum m_s$, M_L and M_S. When the spin-orbit interaction couples orbital angular and spin momenta, the total angular momentum $\vec{J} = \vec{L} + \vec{S}$ is conserved and J becomes a good quantum number. For example for a single $4f$ shell containing only one electron (trivalent cerium electron configuration) [24], then following the Hund's rules, the maximum $L = 3$

and $S = \frac{1}{2}$ lead to antiparallel configuration $J = |L - S| = \frac{5}{2}$ with the lowest energy while the parallel configuration $J = L + S = \frac{7}{2}$ would be separated in energy by the spin-orbit coupling strength.

While the introduction into the atomic electron properties is an important basis especially for core-level spectroscopy, all interatomic interactions have been neglected so far. Before discussing valence electrons and bands in the next section, one important model for strongly localized electrons is the concept of a crystalline electric field (CEF). Here, the presence of the ions surrounding the atom is described by an effective potential V_{CF} which further lifts the $2J + 1$ degeneracy of the spin-orbit split states. For treatment as additional perturbation, V_{CF} is usually expanded in terms of spherical harmonics

$$V_{\mathrm{CF}} = \sum_{k=0}^{\infty} \sum_{m=-k}^{k} A_{km} \underbrace{\sqrt{\frac{4\pi}{2k+1}} Y_{km}}_{C_{km}} \tag{2.5}$$

where A_{km} are the expansion coefficients. Foremost, the crystal potential follows the crystal symmetry which strongly reduces the number of A_{km}. A number of different conventions exist for the exact definition of these so called crystal-field coefficients were the radial integral over r^k is sometimes factored out. Another representation are the Stevens parameters based on the Stevens approximation were mixing between different J values is neglected [25]. This approximation is in most cases reasonable for trivalent cerium where the strength of the spin-orbit coupling is stronger than the crystal field. Hence, the $4f$ shell ($n = 4$, $l = 3$) occupied by one electron in the trivalent Ce is first split by spin-orbit interaction in the $J = \frac{5}{2}$ and $J = \frac{7}{2}$ levels and each level can be further split by a crystal potential.

However, independent of the strength and symmetry of the crystal field potential, the time-reversal symmetry prevents the splitting of levels beyond double degeneracy if the system contains an odd number of fermions. In case of trivalent cerium, this so-called Kramer´s theorem [26] thus allows for a maximal splitting of the $J = \frac{5}{2}$ level in three crystal-field Kramers pair states.

2.2 Formation of bands

The atomic approach is suited for describing core electrons, however the central field as well as crystal field approximations break down when there is an (non-negligible) overlap of orbitals with the ones of neighboring atoms. While these interactions can be accounted for in the ligand field theory by allowing electron transfers between different atoms, a suitable approach for crystals is the utilization of the crystal symmetry. Here, instead of using a central potential, a periodic crystal potential is used for the independent-particle approximation. For a lattice a translation vector $\vec{T} = n_1\vec{a}_1 + n_2\vec{a}_2 + n_3\vec{a}_3$ with the primitive lattice vectors $\vec{a}_i$

and $n_i \in \mathbb{Z}$ can be defined. Hence, both Hamiltonian and potential are invariant under the translation by $\vec{T}$ and the solutions of the Schrödinger equation have the form [27]

$$\psi_{\vec{k}}(\vec{r}) = e^{i\vec{k}\vec{r}} u_{\vec{k}}(\vec{r}) \tag{2.6}$$

consisting of a plane wave term with a wave vector $\vec{k} = (k_x, k_y, k_z)$ and a periodic function with the same periodicity of the crystal $u_{\vec{k}}(\vec{r}) = u_{\vec{k}}(\vec{r} + \vec{T})$.

Because of the periodicity of $u_{\vec{k}}$, part of the plane wave´s periodicity can be absorbed in u if $\vec{k}$ becomes larger than any of the primitive reciprocal lattice (wave) vectors. In detail, a reciprocal lattice vector $\vec{G}$ can be defined as $e^{i\vec{G}\vec{T}} = 1$. Based on this definition, corresponding primitive reciprocal lattice vectors $\vec{b}_i$ to the primitive lattice vectors a_i can be found and $\vec{G} = \sum_{i=1}^{3} n_i \vec{b}_i$. Then, for the Bloch function follows

$$\psi_{\vec{k}}(\vec{r}) = e^{i\vec{k}\vec{r}} u_{\vec{k}}(\vec{r}) = e^{i(\vec{k}+\vec{G})\vec{r}} \underbrace{e^{-i\vec{G}\vec{r}} u_{\vec{k}}(\vec{r})}_{u_{\vec{k}+\vec{G}}(\vec{r})} = \psi_{\vec{k}+\vec{G}}(\vec{r}) \tag{2.7}$$

because $e^{-i\vec{G}\vec{r}} u_{\vec{k}}(\vec{r})$ is a new periodic function by definition of $\vec{G}$. In this way, all Bloch function can be shifted by a reciprocal lattice vector $\vec{G}$ into a single zone called Brillouin zone based on the reciprocal primitive lattice units. In this reduced zone scheme, the backfolded eigenfunctions by different $\vec{G}_n$ are now described by a single $\vec{k}$ and labeled by an additional index n. The corresponding eigenenergy dispersions $\varepsilon_n(\vec{k})$ are then called bands with the band index n with the entirety of all bands being called band structure.

Finally, in the same matter as for the atomic states, the band states are filled from lowest to highest energy by the available electrons leading to occupied bands below the Fermi level and unoccupied states above the Fermi level E_F. At finite temperature, the occupation follows the Fermi-Dirac distribution (FDD) $f(\varepsilon)$ [28, 29], which gives the probability for a state at energy ε to be occupied by an electron,

$$f(\varepsilon) = \frac{1}{e^{(\varepsilon - E_\mathrm{F})/(k_\mathrm{B}T)} + 1} \tag{2.8}$$

with T being the temperature and k_B the Boltzmann constant.

2.3 Density functional theory

The basis of DFT is again the general Equation (2.2) after the Born-Oppenheimer approximation. The three contributing terms will be called for simplicity now T for the kinetic, V for the electron potential and U for the electron-electron interaction. For N electrons, the corresponding Schrödinger equation can then be formulated as

$$H\psi = (T + V + U)\,\psi = \left(\sum_{i}^{N} \left(\frac{-\hbar^2}{2m_i} \nabla_i^2 \right) + \sum_{i}^{N} V\left(\vec{r}_i\right) + \sum_{i \neq j}^{N} \frac{1}{2} U\left(\vec{r}_i, \vec{r}_j\right) \right) \psi = E\psi \tag{2.9}$$

The aim of the DFT method now is to map the many-body problem on a non-interacting electron problem without interaction U.

The key for this approach is to reformulate the many-body Hamiltonian by the electron density $n(\vec{r})$ using the Hohenberg-Kohn theorems [30], which prove that to a given ground state electron density $n_0(\vec{r})$, the potential $V(\vec{r})$ is uniquely defined and thus the ground state wave function $\psi_0 = \psi[n_0]$, too. This formulation holds for non-degenerate ground states but can be extended to degenerate ground states, too [31, 32].

In particular, the ground state energy can be expressed as density functional and divided into the contributing terms:

$$E_0 = E[n_0] = T[n_0] + V[n_0] + U[n_0] \tag{2.10}$$

with $T[n_0]$, $V[n_0]$ and $U[n_0]$ being the ground-state expectation values of T, V and U as functionals of n_0. By defining a universal function $F[n] = T[n] + U[n]$ that it is valid in the same way as $T[n]$ and $U[n]$ for any number of particles and and any external parameters, the energy functional can be expressed as

$$E[n] = F[n] + V[n] = F[n] + \int V(\vec{r}) n(\vec{r})\, \mathrm{d}\vec{r} \tag{2.11}$$

which would yield the ground state energy E_0 for the correct density n_0. Because of the long range Coulomb interaction, $F[n]$ can be reformulated as

$$F[n] = \frac{1}{2} \int \frac{n(\vec{r}) n(\vec{r}\,')}{|\vec{r} - \vec{r}\,'|} \,\mathrm{d}\vec{r}\,\mathrm{d}\vec{r}\,' + T_\mathrm{s}[n] + E_\mathrm{xc}[n] \tag{2.12}$$

with $T_\mathrm{s}[n(\vec{r})]$ being the kinetic energy of a system of non-interacting electrons with the density $n(\vec{r})$ and $E_\mathrm{xc}[n(\vec{r})]$ is the exchange and correlation energy of an interacting system with density $n(\vec{r})$.

Now, minimizing $E[n]$ in Equation (2.11) using Equation (2.12) by assuming a stationary density $\int \delta n(\vec{r})\, \mathrm{d}\vec{r} = 0$ leads to

$$\int \delta n(\vec{r}) \left(\underbrace{V(\vec{r}) + \int \frac{n(\vec{r}\,')}{|\vec{r} - \vec{r}\,'|} \,\mathrm{d}\vec{r}\,' + \frac{\delta E_\mathrm{xc}}{\delta n(\vec{r})}}_{V_\mathrm{s}} + \frac{\delta T_\mathrm{s}}{\delta n(\vec{r})} \right) \mathrm{d}\vec{r} = 0 \tag{2.13}$$

resulting in the same form as obtained for a system of non-interacting electrons with an potential V_s. Hence, by solving a system of N one-particle Schrödinger equations (Kohn-Sham equations) [33]

$$\left(-\frac{1}{2}\nabla^2 + V_\mathrm{s}(\vec{r})\right)\varphi_i(\vec{r}) = \varepsilon_i(\vec{r})\varphi_i(\vec{r}) \tag{2.14}$$

one obtains

$$n_s(\vec{r}) = \sum_{i=1}^{N} |\varphi_i(\vec{r})|^2 \tag{2.15}$$

where N is the number of electrons. Therefore, by defining $n(\vec{r}) = n_s(\vec{r})$, the many-body Schrödinger equation of N electrons can instead be solved by a system of N one-particle Schrödinger equations. The ground state density $n_0(\vec{r})$ can be obtained solving Equation (2.14) and Equation (2.15) self-consistently using the definition of V_s in Equation (2.13). Finally, it has to be noted that a similar approach can be done using the Dirac equation instead of the Schrödinger equation leading to the relativistic density functional theory.

However, this method so far simply shifts the complexity of the electron-electron interaction into the term for the exchange and correlation energy $E_\mathrm{xc}[n(\vec{r})]$ which is not known in the general case. However, a number of approximations exist for the exchange and correlation functional. A simple and widely-used approximation is the linear density approximation (LDA) where the exchange and correlation functional depends only on the density at the coordinate where it is evaluated (local correlation) with

$$E_\mathrm{xc}^\mathrm{LDA}[n(\vec{r})] = \int \varepsilon_\mathrm{xc}(n)n(\vec{r})\,\mathrm{d}\vec{r} \tag{2.16}$$

It assumes a slowly changing density $n(\vec{r})$ and the exchange-correlation energy ε_xc is in most cases derived directly from the homogeneous electron gas. In this case, $E_\mathrm{xc}[n]$ can be split in the exchange and correlation term and an analytical solution is available for exchange term $E_\mathrm{x}[n]$ and a number of different approaches for the correlation term $E_\mathrm{c}[n]$.

In the generalized gradient approximation (GGA), the exchange and correlation energy is expanded in terms of the gradient of the density to account for non-homogeneity of the electron density [34]. This way, corrections to the exchange and correlation energy based on the changes in the density away from the coordinate are possible. By taking even higher terms than n and ∇n into account, more complex and potentially more accurate descriptions of the exchange and correlations energy can be achieved. Further, by including exact exchange energies calculated from Hartree–Fock theory (hybrid functionals [35]), in special cases a better description can be achieved for a higher computational cost.

Finally, the here presented approach is often expanded by employing two spin densities $n_\downarrow$ and $n_\uparrow$ to account for spin-polarized systems. In this approach, the exchange and correlation energy depend on both spin densities $\varepsilon_\mathrm{xc}(n_\downarrow, n_\uparrow)$.

2.4 Local moments and Kondo interaction

The previous sections were devoted to the band model by describing the electrons in a one-electron theory like in DFT. However, when the electron correlation can no longer be described in such a picture due to complex influences of the electrons with each other, the electrons are called strongly correlated and their behavior is governed by many-body effects. While for core electrons the shells are fully occupied and strongly localized and their behavior well described in the atomic picture, the incompletely filled but still localized d and f electrons often show strong correlation effects due to their great on-site Coulomb repulsion. In the following, a very short introduction into phenomena linked to these strong correlations is given. A detailed and comprehensive introduction can be found in a number of books like Hewson 1993 [36].

2.4.1 Single impurity Anderson model

One effective model which describes the interaction between a single localized level (impurity state) with the creation operator $f^\dagger$ and an on-site Coulomb repulsion U and the conduction band with creation operator $c^\dagger$ is the so called single impurity Anderson model [37]

$$H = \sum_{k,\sigma} \varepsilon_k c^\dagger_{k\sigma} c_{k\sigma} + \sum_\sigma \varepsilon_f f^\dagger_\sigma f_\sigma + U f^\dagger_\uparrow f_\uparrow f^\dagger_\downarrow f_\downarrow + \sum_{k,\sigma} V_k (f^\dagger_\sigma c_{k\sigma} + h.c.) \tag{2.17}$$

where V defines the hybridization between the states. While this Hamiltonian only describes the interaction of a single impurity state with the conduction electron, it offers a wide variety of regimes and properties. The Anderson impurity model can further be expanded from a single impurity state to a periodic model with the implications discussed in Section 2.4.2, already the single impurity case offers a wide variety of regimes and concepts for understanding also Kondo lattice systems.

Firstly, the atomic case with only small hybridization shows different regimes for the impurity level. In case of no occupancy of the impurity level, the energy from the impurity is 0. In the case of a single occupancy $|\sigma\rangle = f^\dagger_\sigma |0\rangle$, the energy is ε_f and in case of a double occupancy, the energy is $2\varepsilon_f + U$. With the usual case of $U > 0$, the empty impurity state regime is thus stabilized for $\varepsilon_f \gg 0$ while a local moment regime is stabilized for $\varepsilon_f \ll 0$. The case were different occupations are very close in energy is called the intermediate regime. For the case of the local moment regime and a small but finite V, the two different local moment states with different spin can mix due to hopping with the conduction band. This problem was famously treated by Schrieffer and Wolf [38] who froze out the charge fluctuation on the impurity model leading to

$$H = \sum_{k,\sigma} \varepsilon_k c^\dagger_{k\sigma} c_{k\sigma} - \sum_{k,k'} J_{kk'} \vec{s}_{kk'} \vec{S}_f \tag{2.18}$$

with $\vec{S}_f$ being the spin of the impurity, $\vec{s}_{kk'} = \sum_{\sigma,\sigma'} c^\dagger_{k'\sigma'} \vec{\sigma} c_{k\sigma}$ and the coupling constant $J_{kk'}$ which can connected to the Anderson model. Reducing $J_{kk'}$ to the conduction electrons $J_{k_\mathrm{F}k'_\mathrm{F}} = J_\mathrm{K}$ leads to the classical Kondo Hamiltonian (also $s-d$ interaction Hamiltonian or Zener Hamiltonian [39]) $H = \sum_{k,\sigma} \varepsilon_k c^\dagger_{k\sigma} c_{k\sigma} - J_\mathrm{K} \vec{s} \cdot \vec{S}_f$ where the conduction electrons scatter at the spin of the impurity with an antiferromagnetic coupling $J_\mathrm{K} < 0$.

The Kondo model is useful to discuss magnetic interactions in real systems. The perturbative treatment to third order [3] revealed an additional contribution $\sim J_\mathrm{K} \rho \log\left(\left|\frac{k_\mathrm{B}T}{D}\right|\right)$ (with band width D and density of states ρ) to the resistivity that for the antiferromagnetic coupling scheme $J_\mathrm{K} < 0$ leads to extra scattering term which increases as the temperature is lowered. While this was able to explain the resistance minimum observed in metals with impurities [4], the resistivity diverges for $T \to 0$ which became known as the Kondo problem [40]. The temperature at which the perturbation theory breaks down has become known as the Kondo temperature T_K given by

$$T_\mathrm{K} \sim e^{-1/(|J_\mathrm{K}|\rho)} \tag{2.19}$$

Solving this problem was a big undergoing starting from the so called poor man's scaling approach of Anderson [41], which was basis for the renormalization group method [42]. Exact results were found using the Bethe Ansatz for one dimension [43, 44]. The essence of what is happening below T_K can also be interpreted in the framework of the Landau theory of Fermi liquids described by Nozières [45]. Below T_K, the impurity is screened out by conduction electrons leading to an non-magnetic impurity called the Kondo singlet. Low energy excitations can be interpreted as quasiparticles with enhanced masses m^* due to the Kondo interaction which means that $1/m^*$ should be connected to T_K. The density of states should hence form a narrow peak for these quasiparticles above the Fermi level with a width proportional to T_K which is known as the Kondo resonance (Abrikosov-Suhl resonance) [46, 47]. Far above T_K, the magnetic impurities are no longer screened leading back to an isolated magnetic moment.

2.4.2 Periodic lattice

The so far discussed models focus on a single impurity or diluted impurities which do not interact with each other. In a lattice of impurities however, the local moments can interact indirectly through an induced Friedel oscillation in the conduction electrons called Ruderman-Kittel-Kasuya-Yosida (RKKY) interaction [48–50]. In dense local moment systems this normally leads to an ordered antiferromagnet (AFM) state with a Néel temperature $T_\mathrm{N} \sim J^2 n$. This magnetically ordered ground state is obviously in direct competition to the non-magnetic Kondo screened state where the local moments are quenched as discussed for the single impurity. This was phenomenologically compared by Doniach [51] and shown as Doniach phase diagram in Figure 2.1. For small $|J|$, the RKKY interaction is dominating leading to an magnetic ground state while for larger $|J|$ the system transitions to the Fermi-liquid spin-compensated ground state while crossing a quantum critical point.

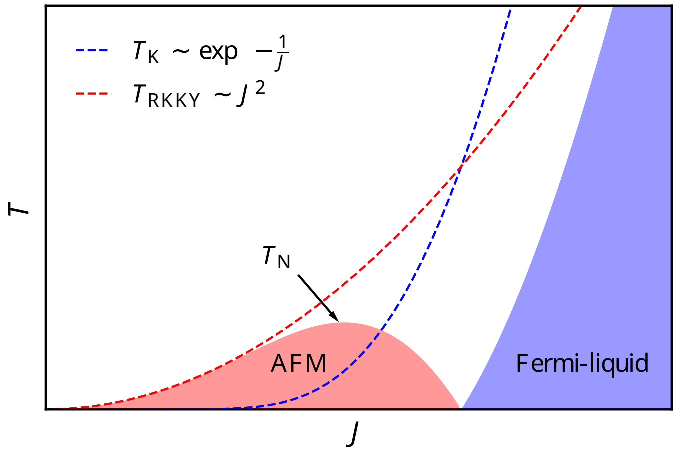

Figure 2.1: Doniach phase diagram showing the quadratic scaling of the RKKY interaction and the exponential scaling of the Kondo interaction. For small J, the RKKY interaction dominates leading to a magnetic ground state while for large J the Kondo interaction dominates resulting in a non-magnetic ground state. For $T = 0$, the phase diagram crosses a quantum critical point between the two phases.

Besides the magnetic ground state, another effect occurs when going to a dense Kondo lattice. Going back to the Fermi-liquid picture of Nozières, the single impurity quasiparticles can form a coherence below a coherence temperature T_coh which, in contrast to the single impurity case, leads to coherent scattering reducing the resistivity rapidly. Due to the effective mass enhancement observed in such Kondo lattice systems, these systems are also commonly called heavy-fermion or heavy-electron systems [52].

2.5 Spin excitations

In the previous section, the coupling of magnetic moments was discussed both in the case of the Kondo model in screening of the impurity spin as well mentioned in the RKKY interaction. This section will focus on the a magnetic ground state and will discuss the possible spin excitations. Starting point is the Heisenberg exchange Hamiltonian [53]

$$H = -\frac{1}{2}\sum_{i,j} J_{ij}\vec{S}_i\vec{S}_j \tag{2.20}$$

with the exchange coupling J between spins $\vec{S}_i$ at sites i. Rewriting this equation with raising and lowering operators $S^{\pm} = S^x \pm iS^y$ becomes

$$H = -\frac{1}{2}\sum_{i,j} J_{ij} S_i^z S_j^z - \frac{1}{4}\sum_{i,j} J_{ij}\left(S_i^+ S_j^- + S_i^- S_j^+\right) \tag{2.21}$$

For understanding spin excitations, the most simple case is a linear chain of spins with nearest neighbor interaction $J_{i,i+1} = J$ and ferromagnetic coupling $J > 0$, which simplifies the sums in Equation (2.21) to

$$H = -J\sum_i S_i^z S_{i+1}^z - \frac{1}{2}J\sum_i \left(S_i^+ S_{i+1}^- + S_i^- S_{i+1}^+\right) \tag{2.22}$$

As can be seen, the ground state is ferromagnetic since $J > 0$ and defined as $|0\rangle$ with $S_i^z |0\rangle = \frac{1}{2}|0\rangle$ and the ground state energy $E_0 = -NJ/4$ with N begin the number of sites. Looking at the state with a single spin flip at site j defined as $|j\rangle = S_j^- |0\rangle$, then one can see

$$H|j\rangle = \left(E_0 + \frac{J}{2}\right)|j\rangle - \frac{J}{2}|j+1\rangle - \frac{J}{2}|j-1\rangle \tag{2.23}$$

that $|j\rangle$ is not an eigenstate of H. Instead, the flipped spin can stay at the same site or hop between sites behaving like a quasiparticle or collective excitation. Thus, in a particle picture a logical step would be a plane-wave Ansatz which corresponds to the more general Bethe Ansatz [54] which is commonly used to solve Heisenberg Hamiltonians. The plane-wave Ansatz then yields the solution for the energy dispersion for an infinite chain with

$$E(q) = 2J\sin^2\frac{qa}{2} + E_0 \tag{2.24}$$

where q is the momentum and a the spin spacing. Hence, the excitations of magnetic ground states are not single spin flips but collective excitations called magnons. The antiferromagnetic case is more complicated since the alternating spin state state is not an eigenstate of the Heisenberg chain Hamiltonian [55].

For solving complex systems with more than nearest neighbor interaction and in more than one dimension, one common tool is the linear spin wave theory. Here, the Heisenberg Hamiltonian of Equation (2.21) will be transformed using the Holstein-Primakoff transformation which maps bosonic annihilation and creation operators to the spin operators [56]. In the linear spin wave theory, only the lowest order of the boson operators are kept which strongly simplifies the calculation. This approximation holds well as long as the spin is large and close to its classical value as well as at low temperatures.

In Figure 2.2, the dispersion relation of the spin excitations for the ferromagnetically and antiferromagnetically ordered Heisenberg chain is shown. The calcu-

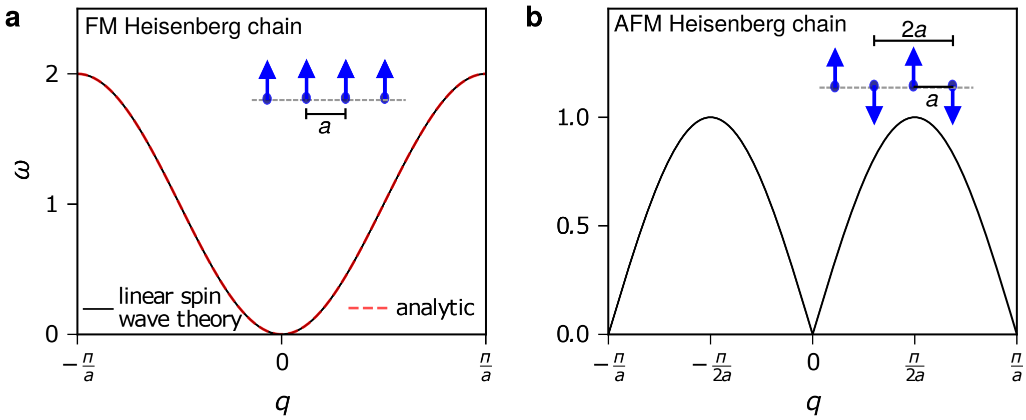

Figure 2.2: Results for the magnon excitation energy dispersion (ω with $\hbar = 1$) calculated with the linear spin wave theory implemented in SpinW for the (a) ferromagnetic and (b) antiferromagnetic Heisenberg spin-1/2 chain with nearest neighbor exchange coupling $J = \pm 1$. For the ferromagnetic case, the analytical solution of Equation (2.24) is added.

lation were performed using the linear-spin-wave-theory code SpinW [57]. For the ferromagnetic ordering, the analytical solution of Equation (2.24) is added, showing no difference between both results. There are two main differences in the dispersion between the ferromagnetic and antiferromagnetic configuration, namely the behavior for $|q| \to 0$ and the size of the reciprocal lattice. For $|q| \to 0$, the ferromagnetic configuration shows a typical parabolic behavior for long wavelength excitations. On the other hand, the typical behavior for the antiferromagnetic configuration is a linear dependence of ω with respect to small $|q|$. Additionally, the dispersion is already periodic in the interval $-\frac{\pi}{2a}$ to $\frac{\pi}{2a}$ instead of $-\frac{\pi}{a}$ to $\frac{\pi}{a}$. The reduced size of the reciprocal lattice constant is a direct result of the increase of magnetic unit cell. While the spacing of the spins of the chain is a (corresponding to the crystal unit cell), the translational symmetry with respect to the spin is only achieved by a translation of $2a$ (corresponding to an enlarged magnetic unit cell). This concept is important when comparing magnetic systems with the same lattice constants but different magnetic unit cells.

3 Measuring with X-rays

This chapter briefly introduces the applied X-ray spectroscopic and scattering methods.

3.1 Introduction

In the previous chapter, a number of concepts like electronic levels and electronic configurations, bands and quasiparticle excitations were discussed, however their properties only become visible or well defined when the electronic system is probed or perturbated by external influences. One of the most common, important and influential interactions is the one between electronic systems and photons. This interaction is not only the basis for our visual world around us but also the basis for a large number of different measurement techniques ranging from the usage of radio frequencies over the visible light to hard X-rays.

Our three used methods use photon energies in the ultra violet (UV) and soft X-ray range. In this energy range, the foundation for the description of the interaction between light and matter is the minimal coupling which is adequate to describe the interaction of an electron with momentum operator $\vec{p}$ with a weak electromagnetic field $\vec{A}$. For the most simple and non-relativistic case this leads to

$$H = \frac{\left(\vec{p} - \frac{e}{c}\vec{A}\right)^2}{2m} = \frac{\vec{p}^2}{2m} \underbrace{- \frac{e}{2mc}\left(\vec{p}\vec{A} + \vec{A}\vec{p} - \frac{e}{c}\vec{A}^2\right)}_{H_{\text{int}}} \tag{3.1}$$

Here, H_{int} can now be treated perturbatively to determine the transition probability per unit of time $W_{i\to f}$ up to second order [58]

$$W_{i\to f} = \frac{2\pi}{\hbar}\left| \langle f|\, H_{\text{int}}\, |i\rangle + \sum_m \frac{\langle f|\, H_{\text{int}}\, |m\rangle \, \langle m|\, H_{\text{int}}\, |i\rangle}{E_i - E_m} \right|^2 \delta(E_f - E_i) \tag{3.2}$$

from an initial state $|i\rangle$ to the final state $|f\rangle$ with an intermediate state $|m\rangle$ and their corresponding energies E_i, E_f and E_m. The first term is the famous Fermi's Golden rule [59] term which usually strongly dominates the transition probability because the second order term consists of two transitions. However, based on the denominator in Equation (3.2) for the second order term, its contribution can become significant and even dominating for a resonant process with $E_m \approx E_i$.

Looking back at H_{int} and $\vec{A}$, the vector potential for a polarization α can be expressed in second quantization in terms of creation $a^\dagger_{\vec{k}\alpha}$ and annihilation operators $a_{\vec{k}\alpha}$

$$\vec{A}(r,t) = \sqrt{\frac{2\pi\hbar c^2}{V}} \sum_{\vec{k}} \frac{\hat{\epsilon}_{\vec{k}\alpha}}{\sqrt{\omega_{\vec{k}}}} \left(a_{\vec{k}\alpha} e^{i\vec{k}\vec{r}} + a^\dagger_{\vec{k}\alpha} e^{-i\vec{k}\vec{r}} \right) \tag{3.3}$$

with the polarization vector $\hat{\epsilon}_{\vec{k}\alpha}$. Based on the Coulomb gauge (or using dipole approximation) $\nabla\vec{A} = 0$, H_{int} simplifies to

$$H_{\text{int}} = -\underbrace{\frac{e}{mc}\vec{A}\vec{p}}_{\sim a_{\vec{k}}} + \underbrace{\frac{e^2}{2mc^2}\vec{A}^2}_{\sim a^\dagger_{\vec{k}'} a_{\vec{k}}} \tag{3.4}$$

Looking only at the photon annihilation terms, this shows the two important processes when using photons to probe a sample. The first term is linear in $\vec{A}$ and thus correspond to single-photon processes like the absorption of the photon while the second term describes two-photon processes due to being quadratic in $\vec{A}$ like scattering since a photon can be annihilated and created.

3.2 X-ray absorption spectroscopy

3.2.1 Transition rates and selection rules

As discussed above, when photons are used to probe a sample, the photon can be absorbed. This process is dominated by the first order term in Equation (3.2) corresponding to Fermi's Golden rule. Combining this with Equation (3.3) and focusing only on the photon absorption term with the annihilation operator, the transition rate of the photon absorption can be written as

$$W_{i\to f} = \frac{2\pi}{\hbar} \left| \sqrt{\frac{2\pi\hbar c^2}{V}} \frac{e}{mc} \sum_{\vec{k}} \frac{1}{\sqrt{\omega_{\vec{k}}}} \langle f | \, a_{\vec{k}\alpha} \hat{\epsilon}_{\vec{k}\alpha} e^{i\vec{k}\vec{r}} \vec{p} \, | i \rangle \right|^2 \delta(E_f - E_i) \tag{3.5}$$

At the moment, the states $|i\rangle$ and $|f\rangle$ are the combined product space of N electrons $\left|\psi^N\right\rangle$ and n photons $|n\rangle$. In the same way, the energies E_i and E_f can be separated into the contribution from electrons E^N and of the photons. For simplicity, considering that all photons have the same momentum $\vec{k}$ and polarization α, then the transition probability can be simplified to

$$W_{i\to f} = \frac{4\pi^2}{V} \frac{e^2}{m} \frac{1}{\omega_{\vec{k}}} n_{\vec{k}\alpha} \left| \left\langle \psi^N_f \right| \hat{\epsilon}_{\vec{k}\alpha} e^{i\vec{k}\vec{r}} \vec{p} \left| \psi^N_i \right\rangle \right|^2 \delta(E^N_f - E^N_i - \hbar\omega_{\vec{k}}) \tag{3.6}$$

which can be further simplified by using the dipole approximation which assumes that the vector potential stays approximately constant in comparison to the length scale of the atom $e^{i\vec{k}\vec{r}} \approx 1$. This results in

$$W_{i\to f} \sim \left|\left\langle \psi_f^N \right| \hat{\epsilon}\vec{p} \left|\psi_i^N\right\rangle\right|^2 \delta(E_f^N - E_i^N - \hbar\omega) \tag{3.7}$$

The absorption cross section would be proportional to the sum of the transition rates over all final states $\left|\psi_f^N\right\rangle$. The absorption spectrum, which is the absorption intensity with respect to the incoming photon energy $\hbar\omega$, could then be interpreted in the most basic form as a mapping of the available final states. This means that for a general photon energy in the X-ray regime, the energy is large enough so that the photon can be absorbed by transferring the energy to a (valence or core) electron which gets excited to an unbound state far above E_F, a so called photoelectron state. If the photon energy is now continuously increased, the process stays the same and the absorption intensity only varies slightly. However, at some point, the photon energy reaches a point at which the energy is large enough to excite electrons from a deeper lying core level at which the number of final states skyrockets because the number of final states now includes additional states with a core hole in the previously not excitable core level. Such a jump is called an absorption edge. These edges are labeled alphabetically starting from K for the principle quantum number $n = 0$ of the core state and increasing for larger n. Directly at such an edge, the excitation energy is not necessarily large enough to directly excite the electron to an unbound vacuum level but instead only to the unoccupied states directly above E_F. Thus, in principle, the absorption process could also be sensitive to the electronic configuration of the valence states, however, the final state now contains a core hole which changes the electronic potential (core hole effect). Additionally, transitions to different final states have different probabilities which are known as the so called selection rules.

The dipole selection rules are a direct result of the matrix element $\left\langle \psi_f^N \right| \hat{\epsilon}\vec{p} \left|\psi_i^N\right\rangle$ of Equation (3.7) for atomic wavefunctions where both initial and final state belong to the same Hamiltonian H with a potential V for which $[V, \vec{r}] = 0$, then $\vec{p} = \frac{im}{\hbar}[H, \vec{r}]$ and can thus be replaced by $\vec{r}$. The usage of atomic wavefunctions allows for the separation in radial and angular part and additionally utilizing the rotational invariance can significantly simplify the calculation. Hence, the transition between a state $|JM_J\rangle$ and $\left|J'M_J'\right\rangle$ can be formulated by representing the components of the position operator $\vec{r}$ in the spherical tensor operators $T_q^{(1)}$ with $q \in \{-1, 0, 1\}$ for the different light polarizations resulting in the Wigner-Eckart theorem

$$\langle JM_J| T_q^{(1)} |J'M_J'\rangle = (-1)^{J-M} \begin{pmatrix} J & 1 & J' \\ -M_J & q & M_J' \end{pmatrix} \left\langle J \middle\| T_q^{(1)} \middle\| J' \right\rangle \tag{3.8}$$

which describes the coupling between the angular momenta by the $3J$ symbol combined with the reduced matrix element which does not depend on M, M_J'

and q [60]. The resulting dipole selection rules thus follow from the angular momentum conservation and read that the change of total angular momentum $\Delta J = 0, \pm 1$ with $J + J' \geq 1$ and $\Delta M_J = q$, thus dependent on the polarization of the X-rays. For no coupling between orbital angular and spin momentum, the excitation of electron absorbs the angular momentum of the photon leading to a change $\Delta l = \pm 1$ while $\Delta s = 0$. However, when spin and orbital angular momenta couple due to a strong spin-orbit interaction, only the total angular selection rules for J hold true and the momentum of the photon can be transferred also to the spin of the electron, which forms the basis of using the polarization dependence to investigate magnetic ordering in form of X-ray magnetic circular dichroism (XMCD) and X-ray magnetic linear dichroism (XMLD) spectroscopy.

For XMCD spectroscopy, the difference in the X-ray absorption between left and right circular polarized light is used, usually either for the $L_{2,3}$ edge of $3d$ elements or the $M_{4,5}$ edge of the lanthanides. The corresponding $3d$ or $4f$ valence states can be responsible for magnetism and thus can show an imbalance between spin up and down states which again can lead to different transition probabilities between the spin polarized excitation electron for different circular polarizations. The matrix element for the difference is proportional to the expectation value of the scalar product between propagation vector of the photon and the magnetization, meaning that the strongest XMCD signal will be observable if magnetization and the propagation vector are collinear. Using sum rules, it is possible to infer the orbital angular and spin momenta [61–63]. In contrast, the XMLD signal uses two oppositely linear polarized lights and is sensitive to the square of the magnetization $\langle M^2 \rangle$ meaning that it will also be sensitive to antiferromagnetic ordering. But besides the magnetic origin, linear dichroism is also sensitive to general crystal anisotropy, often called natural linear dichroism.

Lastly, for completeness, the here presented formalism can also be expressed in correlation functions which can offer in many cases an intuitive representation of the absorption process since the correlation or Green's functions can be understood as propagators. The idea will be presented shortly here in an oversimplified way. Starting from the Fermi's Golden rule Equation (3.7), the squared matrix element can be rewritten with the dipole approximation as $\langle \psi_i^N | T^\dagger | \psi_f^N \rangle \langle \psi_f^N | T | \psi_i^N \rangle$ where T is in the general case a transition operator, in the case of X-ray absorption the product of creation and annihilation operator (for excited electron and core hole). The delta function on the other hand can be expanded to the imaginary part of the Green's function $G = (E - H + i\Gamma/2)^{-1}$ which will also include a finite lifetime Γ to the excited state. Summation over all final states $|\psi_f^N\rangle$ will then lead to

$$\sum_f W_{i \to f} \sim \operatorname{Im} \left\langle \psi_i^N \middle| T^\dagger G(\hbar\omega + E_i) T \middle| \psi_i^N \right\rangle \tag{3.9}$$

where the Green's function propagates over all possible final states excited by absorption of $\hbar\omega$ [64].

3.2.2 Measurement techniques

The intensity of the X-ray absorption process has so far been introduced theoretically, however, the experimental measurement of the absorption intensity has not been discussed so far. Directly measuring the absorption is difficult and the most direct method would be measuring the attenuation of the X-rays by transmission through the sample. In the soft X-ray regime, the transmission mode is not possible for bulk samples since the X-ray mean free path is too small. Instead the X-ray absorption cross section has to be measured indirectly by measuring the decay of the created core hole.

Primarily two channels are responsible for the decay of the core hole state. In both processes, the core hole is filled by an electron of a higher shell, but the energy of the transition can either be radiated out by a photon in the fluorescent decay channel or transferred to an other electron which is ejected from the atom in the Auger decay channel. Measuring either of these decay channels can give information about the absorption cross section.

From the theoretical standpoint, measuring the Auger electron yield is the clearest way to get information about the absorption process. The energy of the ejected Auger electron is clearly defined depending only on the transition energy to the core hole state and not on the incoming photon energy. However, the mean free path of the Auger electrons is usually very small (see universal curve in Figure 3.2) in the order of 20 Å for energies in the range of 1000 eV. This mean that measuring the Auger electron yield is rather sensitive to the surface region. In comparison, the corresponding mean free path of the X-rays is in the order of 1000 Å, meaning that there are no saturation effects and the number of created cores holes in the first 20 Å should thus be equal to the absorption cross section.

On the other hand, the fluorescent decay channel can be used as basis for the X-ray absorption spectroscopy by measuring the emitted photon intensity. In contrast to the Auger electron yield, this method is not surface sensitive due to the comparably long mean free path of the created photon, but has a number of other difficulties. Firstly, the Auger decay channel dominates for all lighter atoms and usually all edges besides high energetic K edges. While the mean free path of the emitted photon is large, it is in the same order as the incoming X-rays meaning that saturation effects can strongly alter the fluorescence yield signal in case of non-diluted samples. Additionally, the emitted photons can be reabsorbed called the self-absorption effect which can strongly influence the spectral shape. These effects make the interpretation of the fluorescence yield cloudy for dense materials.

In difference to directly measuring one of the two decay channels, the most common technique is the measurement of the total electron yield, which means that, in contrast to the Auger electron yield, all escaping electrons are counted. Thus, secondary electrons created in the cascade processes of the Auger electrons dominate the total electron yield signal. While the total electron yield is thus connected to the X-ray absorption cross section, the specific process, the probing depth and surface sensitivity are only approximately known. The advantage of this yield is the large signal and a simple way of detection by measuring the electric drain current from ground to sample that compensates for the electric charge leaving the sample in the form of emitted electrons. The probing depth varies depending on the sample properties with a lower bound being the Auger electron mean free path of around 20 Å for energies in the range of 1000 eV. The upper bound is due to the created secondary electrons cloudy, but should still be in the same order of magnitude as for the Auger electrons. For instance, measurements on clean Ni $L_{2,3}$ edge suggest that mean probing depth is around 25 Å [65]. Thus, for the interpretation of the total electron yield signal, the surface sensitivity generally needs to be considered.

3.3 Photoemission spectroscopy

3.3.1 Spectral function and three-step model

The basis of the photoemission spectroscopy is again the absorption of a photon in the same way as for the X-ray absorption spectroscopy discussed above. However, in the (angle-resolved) photoemission spectroscopy, the energies (and emission angles) of the emitted photoelectrons are measured. The emission of a photoelectron, the so called photoelectric effect, was first observed by Hertz [66] and explained by Einstein in 1906 [67]. In the single particle picture, the photon with energy $\hbar\omega$ is absorbed by an electron which then gets ejected from the sample if its energy is larger than the work function Φ. From energy conservation, the kinetic energy of the emitted electron E_{kin} is then

$$E_{\text{kin}} = h\nu - E_{\text{bin}} - \Phi \tag{3.10}$$

where the binding energy E_{bin} is defined as the energy difference from the Fermi level E_{F}. Schematically, this relation is sketched in Figure 3.1(a) visualizing the idea to effectively use photoemission spectroscopy to map the occupied density of states.

Starting from the photon absorption expressed in Fermi's Golden rule in Equation (3.7), the matrix element can can be expressed in the one-particle states ψ_k as

$$\left\langle \psi_f^N \middle| H_{\text{int}} \middle| \psi_i^N \right\rangle \sim \sum_{k,l} \left\langle \psi_f^N \middle| \underbrace{\langle \psi_l | H_{\text{int}} | \psi_k \rangle}_{\sim M_{kl}} c_k^\dagger c_l \middle| \psi_i^N \right\rangle \sim \sum_{k,l} M_{kl} \left\langle \psi_f^N \middle| c_l^\dagger c_k \middle| \psi_i^N \right\rangle \tag{3.11}$$

Now, the photoelectron which will be measured needs to be separated from the N-particle final state $\left|\psi^N\right\rangle$. This is not trivial and the most common approach is the so called sudden approximation which assumes that the photoelectron is removed imminently (suddenly) from the system neglecting any screening of the photoelectron by the rest of the system. The final state can thus be expressed

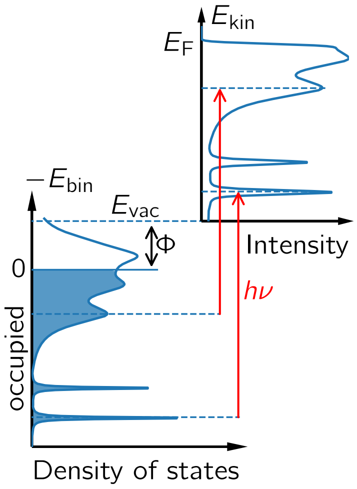

Figure 3.1: Photoelectric process with two excitations indicated by red arrows with an photon energy $h\nu$. E_{bin} defines the energy scale in the solid in respect to E_{F} while E_{kin} stands for the kinetic energy of photoelectron ejection from the sample. The work function Φ denotes the energy difference between E_{F} and the vacuum level E_{vac}.

as $\left|\psi_f^N\right\rangle = c_f^\dagger \left|\psi_m^{N-1}\right\rangle$, where the photoelectron with the creation operator $c_f^\dagger$ is added to one of the $\left|\psi_m^{N-1}\right\rangle$ eigenstates in which the system collapses during measurement. Additionally, since the single particle final state is unoccupied in the initial state $c_f \left|\psi_i^N\right\rangle = 0$, only matrix elements M_{kf} are of interest. Neglecting the off-diagonal elements, the transition rate can then be formulated as

$$W_{i\to f} \sim \sum_k \left(\left|M_{kf}\right|^2 \sum_m \left| \left\langle \psi_m^{N-1} \right| c_k \left| \psi_i^N \right\rangle \right|^2 \delta\left(E_m^{N-1} + E_k^e - E_i^N - \hbar\omega\right) \right) \tag{3.12}$$

where the second term with the sum over m is called the one-particle spectral function for electron removal A_k. It becomes apparent that in case of a non-interacting electron system, the sum over m reduces to a single particle term $k = m$ with the single-particle function ψ_k and corresponding energy E_k which has to directly correspond to the difference $E_k = E^N - E^{N-1}$. Hence, comparing this with the delta function term, one can find that the energy of the photoelectron subtracted by the photon energy $E_k^e - \hbar\omega = -E_k^{N-1} + E_i^N = -E_k$ meaning that measuring the energy of the photoelectron allows determining the binding energy in the initial state and thus the single-particle band structure. However, with strong correlations, multiple states $\left|\psi_m^{N-1}\right\rangle$ will contribute leading to different energies of the photoelectron and thus broadening and satellites in the spectra.

However, the direct calculation of the transition rate is difficult since the photoemission effect happens at a solid-vacuum interface. Hence, neither initial nor final state can be assumed to be a Bloch state near the surface. Only deep within the bulk, an approximation as Bloch state holds true while the photoelectron in vacuum far outside can be approximated by plane waves. In between however, inverse low-energy electron diffraction (LEED) wavefunctions have to be used. In LEED experiments, incoming monochromatic electrons are scattered and the scattered waves sum up to yield the LEED diffraction pattern. Thus, by using the inverse process with the reverse LEED state as the final state into which an initial Bloch state is excited, the photoemission process can be treated. However, since these calculations in one step are difficult, a simpler phenomenological approach is often chosen where the process is divided into three sequential steps [68].

The first step is the optical excitation in the bulk between two Bloch states for the photoelectron. In the very soft X-ray or UV-ARPES regime, the momentum of the photon is small in comparison to the electron momenta and can be neglected. Hence, the momentum relation $\vec{k}_f = \vec{k}_i + \vec{G}$ and energy relation $E_f(\vec{k}_f) = E_i(\vec{k}_i) + \hbar\omega$ hold true for some reciprocal lattice vector $\vec{G}$ and the single particle states $|\psi_i\rangle$ and $|\psi_f\rangle$. In this way, the matrix element $M_{if} = \langle\psi_f| H_{\text{int}} |\psi_i\rangle$ is similar to the X-ray absorption matrix element and thus modulates the spectral intensity depending on the orbital character and photon polarization as well as photon energy and geometric setup. On the other, the spectral function contains all information on the electronic structure and many-body effects.

The second step is the travel of the electron to the surface which can be simplified strongly by assuming that the frequency, or inverse lifetime, of the excited electrons in the bulk is isotropic (k independent). Hence, it only affects the absolute intensity of the photoelectrons with a given energy without changing the k distribution. Because of the finite electron mean free path inside the sample as shown in Figure 3.2, the soft X-ray photoelectron spectroscopy is a surface-sensitive technique. For the Ce $4f$ enhancing photon energy of around 121 eV, the inelastic mean free path is only about 5 to 10 Å. This means that surface effects play an important role and one has to be careful when inferring bulk properties from ARPES measurements.

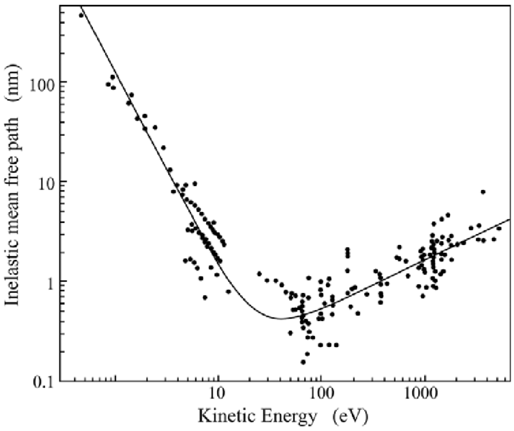

Figure 3.2: Inelastic mean free path of photoelectrons with universal curve [69]

The last step of the three step model is the transmission of the photoelectron through the surface into the vacuum. For this, the electron has to overcome the surface potential. As a result, only the momentum component parallel to the surface is conserved, which can then be indirectly measured. To gain insight into the k_z values, an inner potential has to be modeled. However, for UV-ARPES, the measured spectra show not only the bands for one k_z but the projected bulk bands due to the uncertainty of k_z according to the Heisenberg uncertainty principle. As a consequence, the reciprocal three-dimensional space gets collapsed along the surface normal k_z into a two-dimensional surface plane. Speaking in terms of unit cells, the bulk Brillouin zone gets folded into a surface Brillouin zone (SBZ).

Based on these three steps, the measured ARPES intensity can thus be formulated as [69]

$$I(\vec{k}, E, T) = I_0(\vec{k}, h\nu, \vec{A}) f(E, T) A(\vec{k}, E) \tag{3.13}$$

with $I_0(\vec{k}, h\nu, \vec{A})$ the summed matrix element depending on $\vec{k}$, the photon energy $h\nu$, as well as the the electromagnetic field $\vec{A}$. Because of the third step, the momentum is being conserved only parallel to the surface, $\vec{k} = \vec{k}_{\|}$. The photon energy dependence of the matrix elements allows to study different emissions with different photon energies. Finally, by multiplying with the Fermi-Dirac distribution, the intensity I accounts for the temperature broadening and the occupation of thermally occupied states. Similar to the case of X-ray absorption, the spectral function A can be expressed in the Green function formalism usually in the Lehmann representation [70], however, from a formulation here will be refrained.

3.3.2 Angle-resolved measurements

The most common setup for measuring the momentum and kinetic energy E_{kin} of the photoelectron is the usage of an hemispherical electron analyzer. Before entering the analyzer, the photoelectrons are slowed down and focused in a lens system. The photoelectrons then enter the analyzer through the entrance slit after which they are deflected by an electrostatic field between the two hemispheres. Only electrons in a certain energy range are able to pass and are dispersed onto a micro-channel plate. While traversing the analyzer, the polar angle of the electrons is conserved allowing a two-dimensional imaging of the photoemission intensity with respect to the energy and emission angle on the detector.

While E_{kin} can be transformed into E_{bin} using Equation (3.10), the momentum of the photoelectron $\vec{p}^{\,e}$ can be determined using

$$p_x^e = \sqrt{2mE_{\text{kin}}} \cos\varphi \sin\theta \quad p_y^e = \sqrt{2mE_{\text{kin}}} \sin\varphi \sin\theta \quad p_z^e = \sqrt{2mE_{\text{kin}}} \cos\theta \tag{3.14}$$

with the angles defined as in Figure 3.3. As discussed in the third step of the three-step model, the k_z component is not conserved due to the translation symmetry breaking at the surface. On the other hand, $k_{\|}$ is conserved with $\hbar k_x = p_x^{e^-}$ and $\hbar k_y = p_y^{e^-}$. Thus, the spectral function can be mapped in energy and in the parallel momentum component.

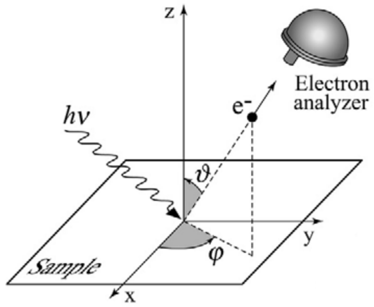

Figure 3.3: The geometry of an ARPES experiment with an photon beam of energy $h\nu$ exciting an photo electron e^- which is detected by an electron analyzer [69].

3.4 Resonant inelastic X-ray scattering

3.4.1 Kramers-Heisenberg formula and low-energy excitations

In X-ray absorption and photoelectron emission spectroscopy, a photon is absorbed. However, resonant inelastic X-ray scattering (RIXS) is, as the name suggests, a scattering process meaning a photon-in photon-out process. As discussed in Equation (3.4), the interaction Hamiltonian contains a term linear in $\vec{A}$ which thus allows for photon absorption or emission, while the second term is quadratic in $\vec{A}$ and thus has a even number of creation and annihilation operators allowing for scattering processes. Indeed, in the non-resonant case the term quadratic in $\vec{A}$ is responsible for scattering processes. However, in the resonant case, the second order term in Fermi's Golden rule dominates which contains the resonant excitation to an intermediate state $|m\rangle$ which then decays to the final state $|f\rangle$ as presented in Equation (3.2). This means that the resonant scattering is indeed linear in $\vec{A}$. Again, the electronic system can be decoupled from the photon states leading again to the electronic many-body states ψ^N. Rewriting the interaction Hamiltonian by the transition operator T, the cross section for the resonant scattering with the incoming photons $\hbar\omega_k$ and outgoing photons $\hbar\omega_{k'}$ can be written using the Kramers-Heisenberg formula as [71]

$$\frac{\mathrm{d}^2\sigma}{\mathrm{d}\hbar\omega_{k'}\,\mathrm{d}\Omega_{k'}} \sim \sum_f \left| \sum_m \frac{\left\langle \psi_f^N \right| T^\dagger \left|\psi_m^N\right\rangle \left\langle \psi_m^N \right| T \left|\psi_i^N\right\rangle}{E_i - E_m + \hbar\omega_k + i\frac{\Gamma_m}{2}} \right|^2 \delta\left(E_i^N - E_f^N + \hbar\omega_k - \hbar\omega_{k'}\right) \tag{3.15}$$

Based on this equation, the RIXS process can be explained. First, the initial state $\left|\psi_i^N\right\rangle$ absorbs a photon resulting in a highly excited state with a deep core hole $\left|\psi_m^N\right\rangle$. This intermediate state decays quickly into the final state $\left|\psi_f^N\right\rangle$ via the two decay channels already discussed for the X-ray absorption spectroscopy, the Auger decay or fluorescence decay. For RIXS, only the radiative decay channel is relevant emitting a photon $\hbar\omega_{k'}$. If the initial and final states are identical, then the system scatters elastically. There are two processes that describe the change of energy and momentum between absorbed and emitted photons, the direct RIXS and the indirect RIXS process. In the direct RIXS process, a core electron transitions after absorption of the photon to an empty valence state. The core hole is subsequently annihilated by the decay of a different valence electron, which leaves the final state with an electron-hole excitation in the valence band [72]. According to energy and momentum conversation, this electron-hole excitation has a momentum $\vec{q} = \vec{k'} - \vec{k}$ and and energy $\hbar\omega_q = \hbar\omega_k - \hbar\omega_{k'}$. This allows for the study of small excitations close to elastic process $\hbar\omega_k \approx \hbar\omega_{k'}$. The advantage of using soft X-rays and exciting a intermediate state with a core hole instead of using visible light as done in Raman scattering are the large photon momenta in RIXS. A photon of 2 eV has a wave vector $k = 0.001\,\text{Å}^{-1}$, thus negligible to excitations in a Brillouin zone of multiple Å. On the other hand, using photon energies around 1000 eV, the photon momentum $k = 0.5\,\text{Å}^{-1}$ allows for a maximal momentum transfer of $q = 2k = 1\,\text{Å}^{-1}$ which is in the order of the primitive reciprocal lattice vectors of usual crystalline systems. Thus, by measuring both the direction and energy of the emitted photon, the dispersion of the excitation can be measured in a sizable part of the Brillouin zone in RIXS.

Since the first step of the RIXS process is X-ray absorption, the same matrix element as in Equation (3.8) defines the transition rate meaning that in the dipole approximation, the selection rules have to be satisfied, too. However, there exists another, more complicated process, called the indirect RIXS process, where the absorbing core electron transitions to an empty state several eV above the Fermi level and then decays back to fill the core hole. Neglecting the core hole state, the process is an elastic scattering. However, the intermediate core hole potential influences the valence states leading to shake-up excitations which can thus be measured using RIXS.

The typical excitations that are studied using X-ray RIXS have excitation energies below a few to tens of eV. The kind of excitation depends on the sample but also on the chosen absorption edge, photon polarization and geometry. The most common excitations will be discussed in the following. The first one are crystal-field and orbital excitations which are result of the orbital degrees of freedom of the valence electrons. If different orbital configurations are split in energy (e.g. by a crystal-electric field), the corresponding excitations are transitions between the different levels. In case of d states, these transitions are called dd excitations.

Another class of excitations are the collective excitations like magnons and phonons. As already discussed in case the case of the X-ray absorption, the photon has a angular momentum which can be transferred to the electron and via spin-orbit coupling resulting in an spin excitation with $\Delta S_z = 1$ or even $\Delta S_z = 2$ (magnon and bimagnon excitations). On the other hand, phonon excitations are a result of the charge disequilibrium due to the extra valence electron in the intermediate state which can generate lattice vibrations.

Lastly, one other contribution is the so called fluorescence feature. Such a feature does not depend on the incoming photon energy $\hbar\omega_k$ and is instead a result of the decay of shallow core electron into the deep core hole state. Hence, the emission $\hbar\omega_{k'}$ from such a transition only depends on the energy difference between the two states.

3.4.2 Setup

In contrast to soft X-ray absorption, where in most cases only either the fluorescence photons (which can be measured by a diode) or the total electron yield (measuring the current draw of the sample), the energy of the outgoing photons has to be determined when measuring RIXS. For this, a large spectrometer is needed when measuring in the soft X-ray regime due to the restrictions of X-ray optics which require gratings for the energy dispersion. The RIXS spectrometer of ID32 of the ESRF is shown exemplary in Figure 3.4.

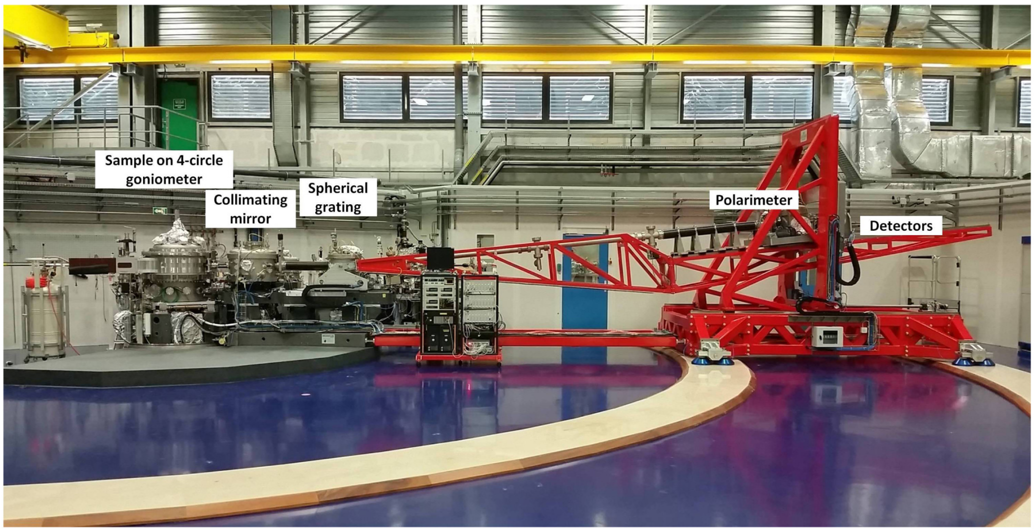

Figure 3.4: View of the RIXS spectrometer of ID32 at the ESRF showing the sample chamber and the spectrometer arm. The red metal structure of the spectrometer arm is moved with the help of air pads on top of the spherically arranged marble tiles on the floor [73].

This spectrometer consists of one main sample chamber and the three chambers of the spectrometer arm under vacuum with base pressures below 10^{-8} mBar. The monochromatic X-ray beam enters the first chamber which contains the four-circle Huber diffractometer allowing for a full rotation of the sample and orientation of the sample in the θ - $2\theta'$ scattering geometry. Connected to this chamber is the load lock with sample storage and the first chamber of the spectrometer arm containing a collimating parabolic mirror from which the outgoing photons are directed onto the spherical gratings in the second chamber of the spectrometer arm. The spherical gratings scatter in vertical direction into the third chamber which is mounted at the end of the spectrometer arm. This chamber contains the CCD detectors, one for the direct beam and a second one which can be used in combination with a multilayer for polarization dependent measurements. For measuring different scattering geometries, the spectrometer arm is movable in an 100° range. The first two chambers are situated on a granite base which can function as an air pad. The metal structure of the spectrometer arm is moved via eight air pads on top of a circular ring of marble tiles. A special pumped ribbon section connected with a bellow allows for the movable connection between the sample chamber and the spectrometer arm. This large mobile spectrometer arm makes it possible to measure for high-resolution spectra for variable photon energies in the soft X-ray regime up to 1600 eV covering a large scattering angle interval. For a full discussion of the ID32 beamline as an state-of-the-art RIXS spectrometer see [73].

4 Surface Kondo sublattices in Ce-based intermetallics

This chapter presents the main results of our ARPES study starting with the Kondo lattice system $CeRh_2Si_2$ followed by our results on the tetravalently-behaving $CeCo_2P_2$. The $CeRh_2Si_2$ study is a continuation of my Master's thesis project and the here presented study is published in G. Poelchen et al., Unexpected differences between surface and bulk spectroscopic and implied Kondo properties of heavy fermion $CeRh_2Si_2$, *npj Quantum Mater.* **5***, 70 (2020). The ARPES results on $CeCo_2P_2$ are published in G. Poelchen et al.,* Interlayer Coupling of a Two-Dimensional Kondo Lattice with a Ferromagnetic Surface in the Antiferromagnet $CeCo_2P_2$, *ACS Nano* ***16****, 3, 3573-3581 (2022). Sections and figures of these publications are included without additional citation.*

The studied samples were grown by the groups of C. Geibel and C. Krellner, while I, together with my collaborators, performed the ARPES measurements. I further performed all the here presented data analysis and in case of $CeRh_2Si_2$ the DFT and model calculations. In case of $CeCo_2P_2$, the final calculations presented here were performed by A. Ernst and I.P. Rusinov.

4.1 Heavy-fermion physics in Ce-based systems

4.1.1 Introduction

With the first observation of heavy-fermion physics in $CeAl_2$ [13], Ce-containing compounds received new interest to study its many-body physics. In $CeAl_2$, unusual low-temperature properties were observed like a very large Sommerfeld coefficient $\gamma = 1620\,\mathrm{mJ\,mol\,K^{-2}}$. Since a large Sommerfeld coefficient is connected to enhanced effective electron masses, the observed $4f$ physics were interpreted as quasiparticle mass enhancements in the single impurity Anderson model as discussed in Section 2.4.

The focus on more materials and new measurement techniques led to a fast and large improvement of the theoretical understanding, but also raised new questions particularly between the different energy scales of the single impurity T_K and the formation of coherence connected to a dense Kondo lattice (see Section 2.4.2) and its coherence temperature. The formation of coherence can be observed in the classic example of La-doped $CeCu_6$ which has a resistivity maximum at around 10 K (see Figure 4.1). However, the doping of La destroys the coherence and leads to a continuous crossover to the single impurity behavior with an increasing resistivity when lowering the temperature. A large number of theoretical works focus on the relationship between the different energy scales and the connected exhaustion problem [74–77] and the link to experimental measurements is still cloudy.

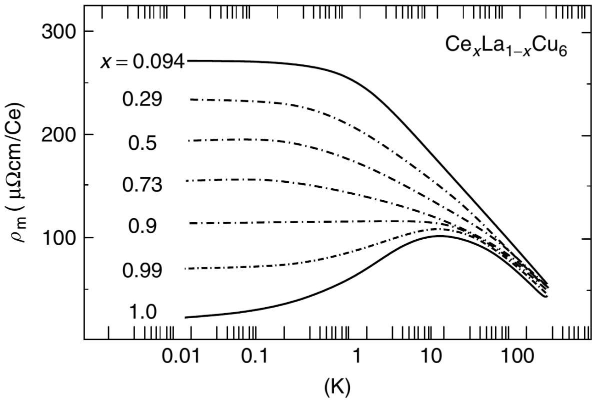

Figure 4.1: Resistivity of $Ce_xLa_{1-x}Cu_6$ for different doping concentrations x. In case of diluted Ce, the resistivity increases when lowering the temperature. With increasing Ce concentration x, a coherent scattering develops reducing the resistivity for very low temperatures ([8], data originally from [78]).

Besides the study of the Kondo/Anderson lattice systems, the class of heavy-fermion superconductors [79–81] after the discovery of the superconducting properties in $CeCu_2Si_2$ [79] as well as the recent exploration of Kondo insulators [82] and Weyl–Kondo semimetals [83] keep the research interest in Ce-based systems high.

4.1.2 Photoemission studies

One important method for the above discussed study of Ce-based systems is the (UV/very soft X-ray) photoemission spectroscopy described in Section 3.3. Here, the first big breakthrough was the utilization of the resonant photoemission process enhancing the $4f$ emission [84]. Using the $4d \rightarrow 4f$ excitation energy at around 121 eV, the emission from $4f$ states becomes enhanced due to a large matrix element for the deexcitation channel from the intermediate state via an $4f$ photoelectron. This made it possible to determine the $4f$ ionization peak at a binding energy of around 2 eV. In combination with bremsstrahlung isochromat spectroscopy (BIS) it became thus possible to fully measure the $4f$ spectral function for electron removal and addition, which was an important milestone for understanding Ce $4f$ physics. A full theoretical description in the degenerate impurity Anderson model by Gunnarsson and Schönhammer made it possible to identify the sharp peak at the Fermi level as the so called Kondo resonance [64]. Measured spectra and calculation are shown together in Figure 4.2.

While a steady improvement of the resolution allowed for a refinement of the fine structure around $4f$, a big advance was gained by measuring not only the integrated photoemission spectra, but the k-dependence of the $4f$ emission. This made it possible to study the band structure renormalization and contribution of the $4f$ to the valence bands. The ARPES measurements and their dispersive

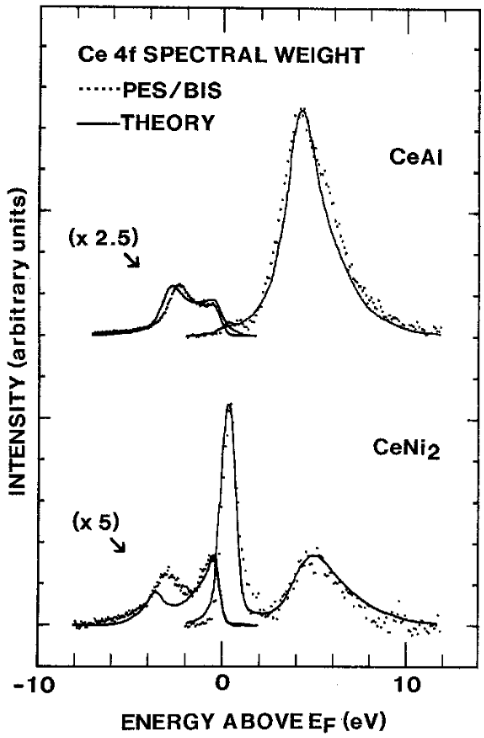

Figure 4.2: Combination of Ce $4f$ resonant photoemission and BIS spectra for CeAl and CeNi$_2$. CeAl is a weakly hybridized $4f$ system with a small T_K, while CeNi$_2$ is a large T_K system. Both materials show a peak at $-2\,\text{eV}$ corresponding approximately to the $4f^1 \to 4f^0$ electron removal and a second peak at 4 eV corresponding to the $4f^1 \to 4f^2$ electron addition. Centered slightly above E_F can be seen the Kondo resonance [85].

structure will be discussed in detail for CeRh$_2$Si$_2$ and CeCo$_2$P$_2$.

4.1.3 Lanthanide ThCr$_2$Si$_2$-type structure

A large number of different Ce-based systems exist. One of the most prominent groups of Ce-based intermetallic systems is the CeT$_2$X$_2$ family with T being a transition element and X a main group element (X = Si, P, As, Ge). Due to the large number of existing members containing from $3d$ up to $5d$ transition elements, this family covers a wide range of properties from weakly- to strongly-hybridized $4f$ electrons, from local-moment AFM ordering to near quantum criticality [86] and heavy-fermion superconductivity [79, 81].

These systems can crystallize in two different structures, usually in the ThCr$_2$Si$_2$- and seldom in the CaBe$_2$Ge$_2$-type structure. The more common ThCr$_2$Si$_2$-type structure belongs to the $I4/mmm$ space group (No. 139), while the CaBe$_2$Ge$_2$-type structure has a reduced symmetry ($P4/nmm$, No. 129). Recently, CeRh$_2$As$_2$, a member of the CaBe$_2$Ge$_2$-type structure, came into focus due to its multiple superconducting phases linked to the local symmetry breaking in the crystal structure [81]. However, for ARPES measurements, the ThCr$_2$Si$_2$-type structure is preferable, since this structure usually only has one cleavage plane perpendicular to the c axis between the Ce ion and the tightly bound X-T-X trilayer block. The cleave of the sample would thus result in either a Ce-terminated surface or a

X-terminated surface.

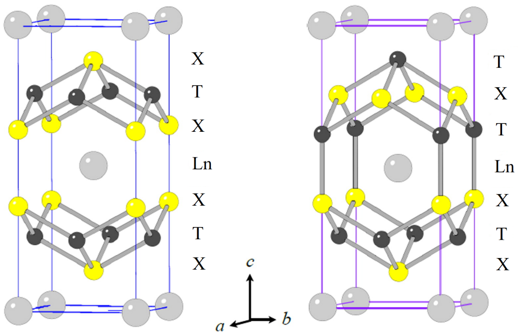

(a) $ThCr_2Si_2$-type

(b) $CaBe_2Ge_2$-type

Figure 4.3: Crystal structures of CeT_2X_2 with the (a) $ThCr_2Si_2$ and (b) $CaBe_2Ge_2$-type. Clearly visible is the missing local inversion symmetry of the $CaBe_2Ge_2$-type structure (based on [87]).

In the following, two ARPES studies for members of the CeT_2X_2 family will be presented. The first one will be $CeRh_2Si_2$, where the Ce is described as an antiferromagnetic Kondo lattice, and the second one will be $CeCo_2P_2$, which behaves differently to all other members of the CeT_2X_2 family with the Ce being best described as tetravalently-behaving.

4.2 Surfaces of $CeRh_2Si_2$

4.2.1 Introduction

The system $CeRh_2Si_2$ is a fascinating member of the CeT_2X_2 family since it exhibits complicated magnetic and electronic properties. First magnetic measurements revealed an antiferromagnetic transition at 36 K [88], while later measurements revealed two magnetic transitions [89, 90]. Neutron diffraction data confirmed two magnetic structures with $T_{N_1} = 36\,\mathrm{K}$ and $T_{N_2} = 24\,\mathrm{K}$. These magnetic phases are suppressed under pressure and the system becomes superconducting at $p = 0.9\,\mathrm{GPa}$ and $T_c = 0.4\,\mathrm{K}$.

Based on inelastic neutron scattering, the Kondo temperature was estimated as $T_\mathrm{K} = 33\,\mathrm{K}$ [91, 92], while nuclear magnetic resonance measurements suggest a Kondo temperature $T_\mathrm{K} \sim 100\,\mathrm{K}$ [93]. From a combination of neutron scattering and RIXS measurements, the crystal electric field scheme was determined to be $\Delta_1 \approx 30\,\mathrm{meV}$ and $\Delta_2 \approx 53\,\mathrm{meV}$ [94].

Lastly, previous ARPES measurements [95] of our group determined the existence of two different surface terminations, namely the Ce-terminated surface and the Si-terminated surface. The different spectra could be separated by a surface state around the $\overline{\mathrm{M}}$ point of the SBZ which is primarily located in the Si-Rh-Si surface block and thus absent in case of the Ce-terminated surface. Going to the $4f$ resonant spectra (on-resonance) at a photon energy of 121 eV, the typical double peaked structure becomes apparent as shown in Figure 4.4. Starting with the off-resonance spectra at a photon energy of 114 eV, the intensity strongly shifts from the strongly dispersive bands to features at E_F and around binding energies around 1 eV to 2 eV. This is not only a result of the $4f$ enhancement but also a suppression of the Rh $4d$ states at 121 eV due to a Cooper minimum in this energy range.

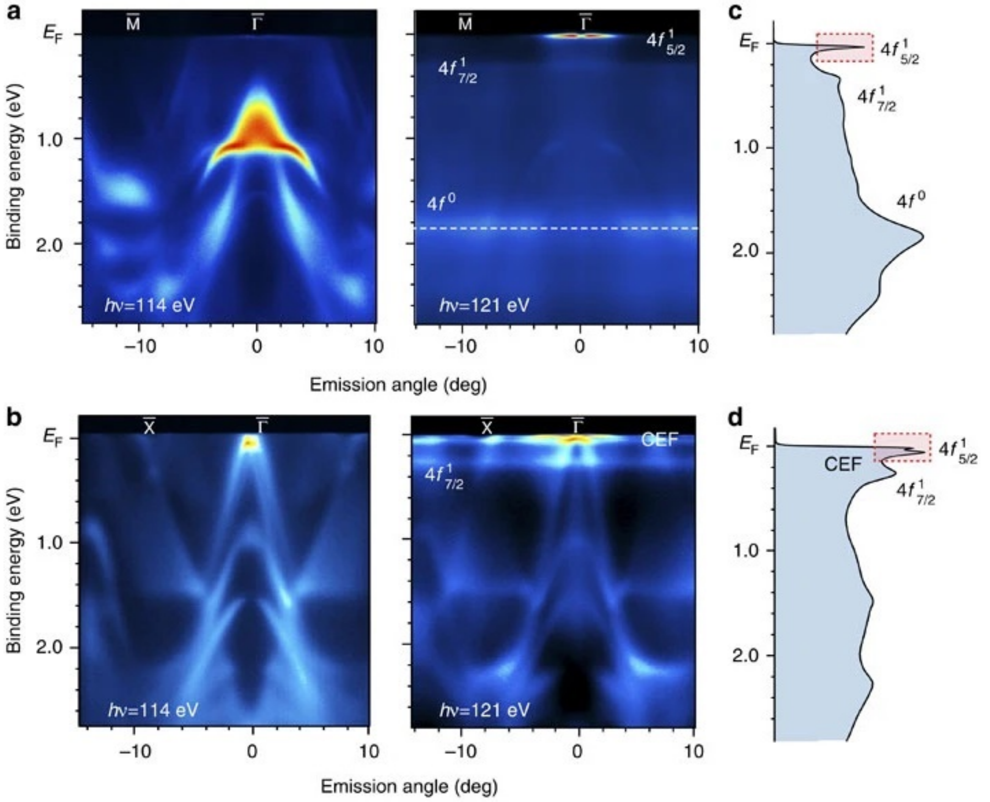

Figure 4.4: ARPES spectra for a (a) Ce-terminated surface and (b) Si-terminated surface for photon energies of 114 eV, and 121 eV. (c) and (d) show the corresponding integrated photoemission profiles of the spectra at 121 eV, respectively [95].

The direct comparison of the on-resonance spectra for both terminations intuitively shows the degree of the $4f$ localization. While for the Ce-terminated surface, barely any intensity can be seen besides two discussed non-dispersive features, the Si-terminated surface shows a richer structure with also the two features looking more dispersive pointing to a stronger interacting between the $4f$ and the valence band. Finally, in Figure 4.4(c,d), the integrated photoemission spectra are shown. The spectra are reminiscent of the spectra shown in Figure 4.2 were the Ce-terminated surface with a strongly defined $4f^0$ peak looks like a weakly hybridized γ-like Ce and the Si-terminated surface like a more strongly hybridized (more α-like) Ce. The work presented in this thesis aims at continuing and completing the understanding of both terminations by performing temperature-dependent measurements studying the Kondo resonance peak at E_F.

4.2.2 Electronic structure characterization

In connection to the previous ARPES study of our group, the first step was the detection of the two distinct surface terminations with a respective Ce- and a Si-terminated surface. The presented measurements were performed at the I05 beamline of the Diamond Light Source facility [96]. The samples of $\mathrm{CeRh_2Si_2}$ were cleaved in situ under ultra-high vacuum conditions better than 10^{-10} mbar. In Figure 4.5(a,b), two clearly different spectra are shown belonging to the Ce- and Si-terminated surface, respectively. The spectra were taken around $\overline{\Gamma}$ along the $\overline{\mathrm{M}} - \overline{\Gamma} - \overline{\mathrm{M}}$ direction of the SBZ in the $4f$ resonance. Further, the main intensities of the spectra are situated around the $\overline{\Gamma}$ point making this the area of interest for an in-depth analysis. Other interesting areas like the surface state around $\overline{\mathrm{M}}$ as well as the dominant bulk band feature called donut were also looked at, however, the intensities around these points were to low to gain definitive answers about there respective temperature behaviors.

A closer look at the corresponding photoemission profiles around $\overline{\Gamma}$ with an angle-integration over $\pm 4^\circ$ shown in Figure 4.5(c,d) reveals the Ce $4f^1$ emission in form of two spin-orbit split peaks with the $4f^1_{5/2}$ hybridization peak at E_F and the $4f^1_{7/2}$ peak in an energy interval of $-300\,\mathrm{meV}$ to $-250\,\mathrm{meV}$. Notable is the shift of the $4f^1_{7/2}$ satellite between the two terminations. In case of the Ce-terminated surface, this satellite is situated at an energy of $-300\,\mathrm{meV}$ while for the Si-terminated surface, its energy is $-250\,\mathrm{meV}$. The reduction of the binding energy for the Si-terminated surface is a clear sign of an enhanced interaction with similar changes of the $4f^n$ final-multiplet splittings being observed for other rare-earth compounds and ascribed to hybridization [97] and screening of the core potential [98].

A second clear difference between the two spectra is the existence of a side band around $-50\,\mathrm{meV}$ for the Si-terminated surface. Its characteristic intensity distribution as seen in Figure 4.5(b) can be attributed to two effects. First, a hole-like valence band which approaches E_F hybridizes with the $4f$ and gets bushed down to lower energies which leads to a transfer of intensity away from E_F to the region around $-50\,\mathrm{meV}$ at the $\overline{\Gamma}$ point. This hole-like band can still be nicely seen at lower energies in Figure 4.5(b). However, this alone cannot describe the large extension of the side band in momentum space. It can be explained by hybridization of the aforementioned valence band with the CEF satellites that are situated in an energy interval of $-60\,\mathrm{meV}$ to $-30\,\mathrm{meV}$ [95]. This fits well the assumed CEF splittings determined by RIXS and neutron measurements [94].

On the other hand, the lack of the side band for the Ce-terminated surface, which becomes especially apparent in the normalized spectra shown in Figure 4.6, is the result of the hole-like valence band being shifted to higher binding energies (see DFT calculations in Section 4.2.4) due to charge transfer. This way, the band is far away from E_F an can not hybridize with the Ce $4f$ states. Additionally, no CEF satellites were observed for the Ce-terminated surface [95] which might be understood by the partial replacement of the mirror symmetric CEF of the

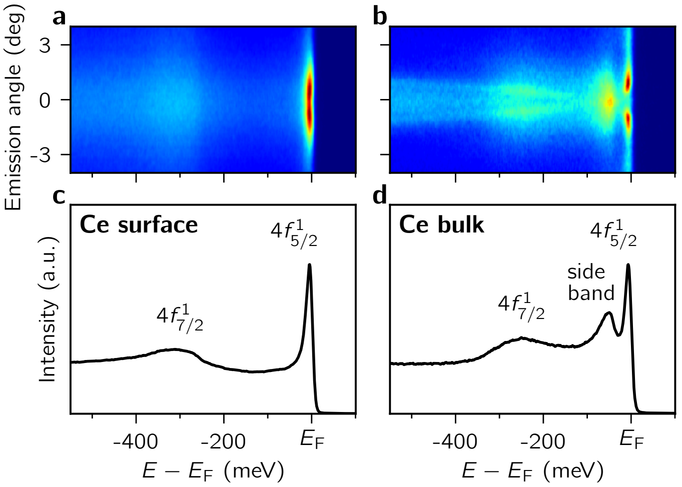

Figure 4.5: On-resonance ARPES spectrum near the $\overline{\Gamma}$ point along the $\overline{M}$-$\overline{\Gamma}$-$\overline{M}$ direction taken at 7 K for (a) Ce- and (b) Si-terminated surfaces of CeRh$_2$Si$_2$, reflecting the properties of surface and bulk Ce atoms, respectively. Photoemission spectra obtained upon integration over the shown k segments (over an emission angle from -4 meV to 4 meV) for each termination are shown in (c) and (d), respectively.

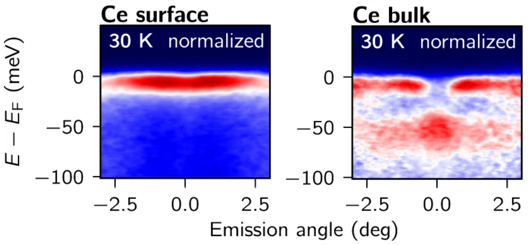

Figure 4.6: Normalized on-resonance ARPES spectra for (left) Ce-terminated and (right) Si-terminated surface at 30 K. Each energy distribution curve (EDC) is normalized to the same intensity clearly visualizing the flat band at E_F and a side band around -50 meV.

bulk by a point-symmetric surface dipole at the surface. This would result in the collapse of the CEF splitting or a CEF splitting that is too small to be resolved. With photonenergies of 121 eV, the photoelectrons only have a inelastic mean free path of the size of a half unit cell (around 5 Å to 8 Å, see universal curve in Figure 3.2), therefore, the emission for the Ce-terminated surface originates by more than 50 % from the surface Ce atoms and can be clearly understood as a probe for the surface Ce. On the other hand, the emission from the Si-terminated surface stems predominantly from the Ce atoms located in the fourth subsurface layer and reflects the bulk-like properties of CeRh$_2$Si$_2$. To emphasize the main contributions, the Ce- and Si-terminated surface are called respectively Ce surface and Ce bulk in all following discussion and figures.

4.2.3 Temperature-dependent behavior

In the next step, the analysis of the temperature dependence of the $4f$ hybridization peaks at E_F and of the side band will be discussed. In Figure 4.7, the $4f$

electronic landscape can be directly compared for different temperatures and reveals well distinguishable modifications for both surface terminations when the temperature is lowered. While the dispersive hybridization peak at E_F is almost not visible at 142 K, its intensity gradually enhances with decreasing temperature and becomes most intense at the lowest temperature (10 K). A similar behavior can be seen for the side band in case of a Si-terminated surface, however the intensity change is weaker and the side band remains visible at 142 K.

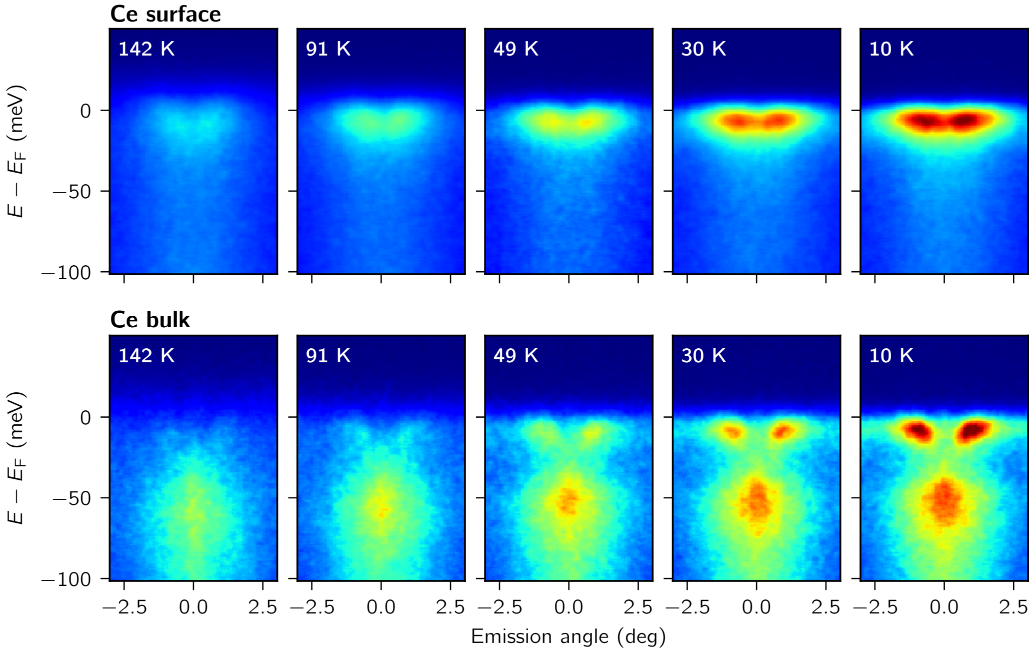

Figure 4.7: Temperature dependence of the k-resolved Ce $4f$-derived states near the $\overline{\Gamma}$ point for (a) Ce- and (b) Si-terminated surfaces of $CeRh_2Si_2$. The ARPES data were taken along the $\overline{M}$-$\overline{\Gamma}$-$\overline{M}$ direction of of the SBZ.

Looking at the photoemission profiles around $\overline{\Gamma}$ over a small angle integration of $\pm 2^\circ$ as shown in Figure 4.8, the temperature dependence can be directly studied. The profiles are normalized below the $4f^1_{5/2}$ emission where they follow the same T-dependent behavior. The aspect that all profiles can be normalized in such a way highlights that the same sample spots were measured over the whole temperature range. Such a measurement is especially tricky due the temperature-dependent length contraction of the manipulator.

As expected, the profiles show the already discussed temperature dependence of the E_F peak and the side band. For later distinction, the E_F peak for the Ce-terminated surface is labeled (1), while the E_F peak is labeled (3) and the side band (2) for the Si-terminated surface. For a quantitative analysis, the intensity of theses peaks needs to be determined, which requires the knowledge of the intensity background which can be subtracted from the measured profiles to

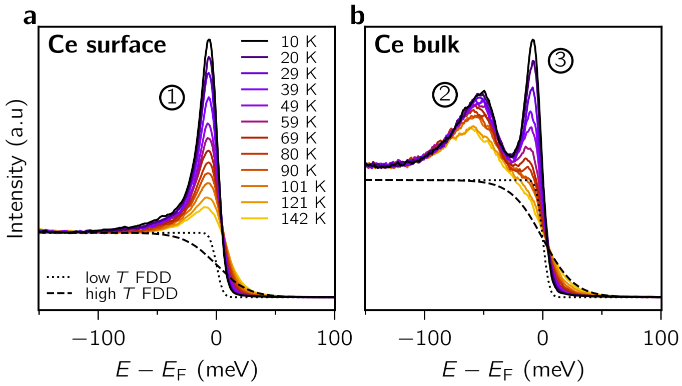

Figure 4.8: Photoemission k-integrated profiles of the $4f$-derived states for various T taken from (a) Ce- and (b) Si-terminated surfaces of $CeRh_2Si_2$. The corresponding FDD backgrounds (convoluted with a Gaussian resolution broadening) are shown for the highest and lowest T as dotted and dashed lines, respectively.

acquire the peak intensity. There are multiple ways to assume a background and our used methods bare a resemblance to the temperature-dependent analysis done for $CeCoIn_5$ [99].

A simple approach for the background is using the FDD which, from a physical standpoint, models an energy-constant intensity that is added to the peak intensity. This seems reasonable as the Rd $4d$ valence band can be in first approximation seen as an intensity-constant band crossing E_F. The FDD backgrounds for the highest and lowest temperature are shown in Figure 4.8 as dashed and dotted lines, respectively. To account for resolution broadening, the FDD backgrounds are convolved with a Gaussian of finite width. The standard deviation σ was defined as the Pythagorean addition of a temperature-independent term σ_{const} accounting for the machine resolution and a temperature-dependent term $\sigma_T(T)$ for temperature-broadening effects like the temperature dependence of the scattering rates. In the depicted case, the two contributions were defined as $\sigma_{\text{const}} = 4\,\text{meV}$ and $\sigma_T(T) = 0.05\,\text{meV}\,\text{K}^{-1} \cdot T$. These values are chosen to be close to the ones determined by the fit model approach discussed in Section 4.2.4. However, different values for σ_{const} and σ_T in a reasonable range can lead to small changes of T_0 in the range of $\pm 2\,\text{K}$.

The resulting profiles after FDD subtraction can be seen in Figure 4.9(a,b). By integrating, the peak intensity is determined and shown in Figure 4.9(c,d). For peak (1), the integration is performed over the shown energy range from $-150\,\text{meV}$ to $100\,\text{meV}$, for peak (2) from $-150\,\text{meV}$ to $-26\,\text{meV}$ and for peak (3) from $-26\,\text{meV}$ to $100\,\text{meV}$. The separating interval bound between peak (2) and (3) at an energy of $-26\,\text{meV}$ is shown as blue dashed line in Figure 4.9(b). This approach to separate the intensities of the E_F peak and the side band introduces a possible error because their tails may extend beyond the integration window. However, these contributions should either cancel out or be small enough to be negligible.

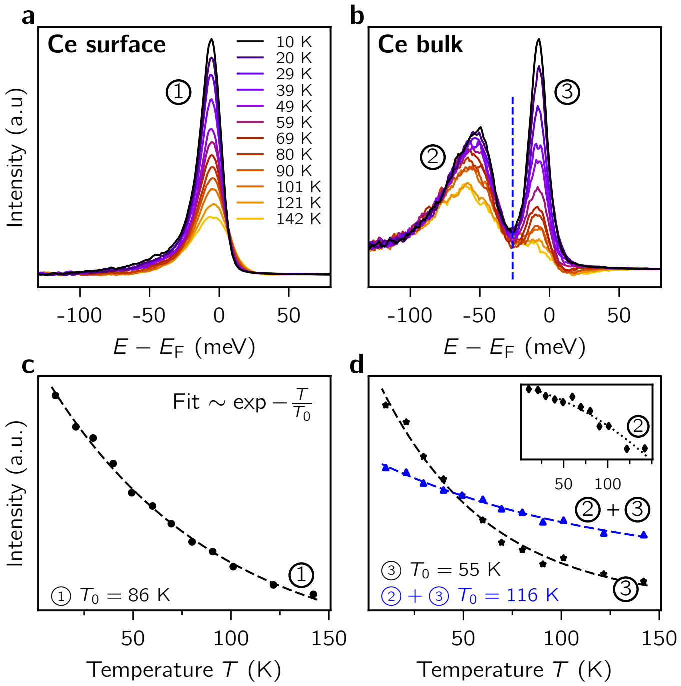

Figure 4.9: Photoemission k-integrated profiles of the $4f$-derived states for various T taken after subtraction of the corresponding FDD backgrounds from (a) Ce- and (b) Si-terminated surfaces of CeRh$_2$Si$_2$. T dependence of the $4f^1_{5/2}$ peak intensity for (c) Ce- and (d) Si-terminated surfaces. The integral intensity of the photoemission peaks were obtained by integration the data shown in (a) and (b). For the E_F peak (3) as well as the side band (2), the integration was performed over the respective intervals left and right of the blue line in (b). The total intensity of peaks (2+3) in blue was scaled by an factor of 1/4 to directly compare the T behavior to peak (2) in black. Inset: the T dependence of the integral intensity of the peak (2) alone.

Finally, the temperature-dependent intensities are fitted by an exponential function of the form $A \exp\left(-\frac{T}{T_0}\right) + C$ which can nicely describe the observed temperature behavior of the E_F peaks (1) and (3) as well as for the total intensity of (2)+(3). As mentioned before, the temperature-dependent change of the side band (2) is weaker and follows more closely a linear behavior as shown in the inset of Figure 4.9(d). By comparing the exponential attenuation T_0, a clear quantitatively-different temperature behavior is seen for the two surface terminations with $T_{0,\mathrm{FDD}}^{①} = 86\,\mathrm{K}$, $T_{0,\mathrm{FDD}}^{③} = 55\,\mathrm{K}$ and $T_{0,\mathrm{FDD}}^{②+③} = 116\,\mathrm{K}$.

To make sure that these values are not an artifact of the background subtraction method, additional backgrounds were explored. First, in contrast with the FDD profile, a temperature-independent linear background was tested as shown in Figure 4.10(a). In case of the E_F peak (1) of the Ce-terminated surface, the linear background simply reaches from low energies, where all profiles are normalized, to higher energies, where the profiles go to zero. However, for the Si-terminated surface, two different linear backgrounds are possible with one including both the E_F peak (3) and the side band (2) and one only for the E_F peak (3). The lower row in Figure 4.10(a) shows the profiles after subtraction of the background. The nonphysical jumps of the slopes at the bounds of the linear background clearly indicate that this subtraction is only a crude approximation. However, the total intensity of the profiles, obtained by integrating after subtraction of the linear background, shows again an exponential behavior with similar values for the exponential attenuation T_0. In case of the Ce-terminated surface, the value for T_0 only differs by less than 5 % from the result of the FDD subtraction with $T^{①}_{0,\mathrm{linear}} = 90\,\mathrm{K}$. In case of the Si-terminated surface, theses deviations are slightly larger with 27 % ($T^{③}_{0,\mathrm{linear}} = 40\,\mathrm{K}$ and $T^{②+③}_{0,\mathrm{linear}} = 97\,\mathrm{K}$).

Finally, a third background subtraction method was explored, using the profile of the measured spectrum at 142 K (highest temperature) as background. Since the contribution of the Ce $4f$ should be barely visible at large temperatures, the profile at 142 K should mainly consist of the valence band emission, and thus, be a good approximation for the background. The spectra before and after subtraction are shown in Figure 4.10(b). A clear nonphysical behavior with negative intensities above E_F can be observed for profiles of lower temperatures because of the corresponding thermal narrowing of the FDD. However, the total intensity, determined by integrating the spectra like in the case of the FDD background, increases and stays positive for all temperatures. The temperature-dependent intensities are shown in Figure 4.10(d) and follow again an exponential behavior. The obtained values of the exponential attenuation T_0 are in good accordance to the ones of the other background subtraction methods. In case of the Ce-terminated surface, the same T_0 was obtained as for the FDD background. Further for the Si-terminated surface, the same value of T_0 was obtained too for the temperature behavior of the sum of both peaks (2)+(3). Only T_0 of the E_F peak of the Si-terminated surface deviates by 12 % from the one obtained by FDD subtraction, underlying the credibility and consistency of the used background subtraction methods.

So far, only the exponential attenuation T_0, which varies only slightly between the different methods, was directly compared. The intensity itself, however, changes strongly between the different methods as shown in Figure 4.11, where the peak intensities are normalized to one at the lowest temperature. Because the assumed backgrounds differ considerably in there assumptions, the corresponding intensities are different. Inherently, in case of the highest temperature profile as background, the intensity at 142 K must be zero. On the other hand, the intensity with a linear background is already larger than 0.5 at the highest temperature for the Ce-terminated surface, since it underestimates the intensity of the background. Hence, the high-temperature profile gives a lower limit and the linear background an estimation of the upper limit of the intensity. In between lies the data after the FDD subtraction, which thus gives probably the closest estimate to the real intensity. Because of this, the values of T_0 as obtained for the FDD

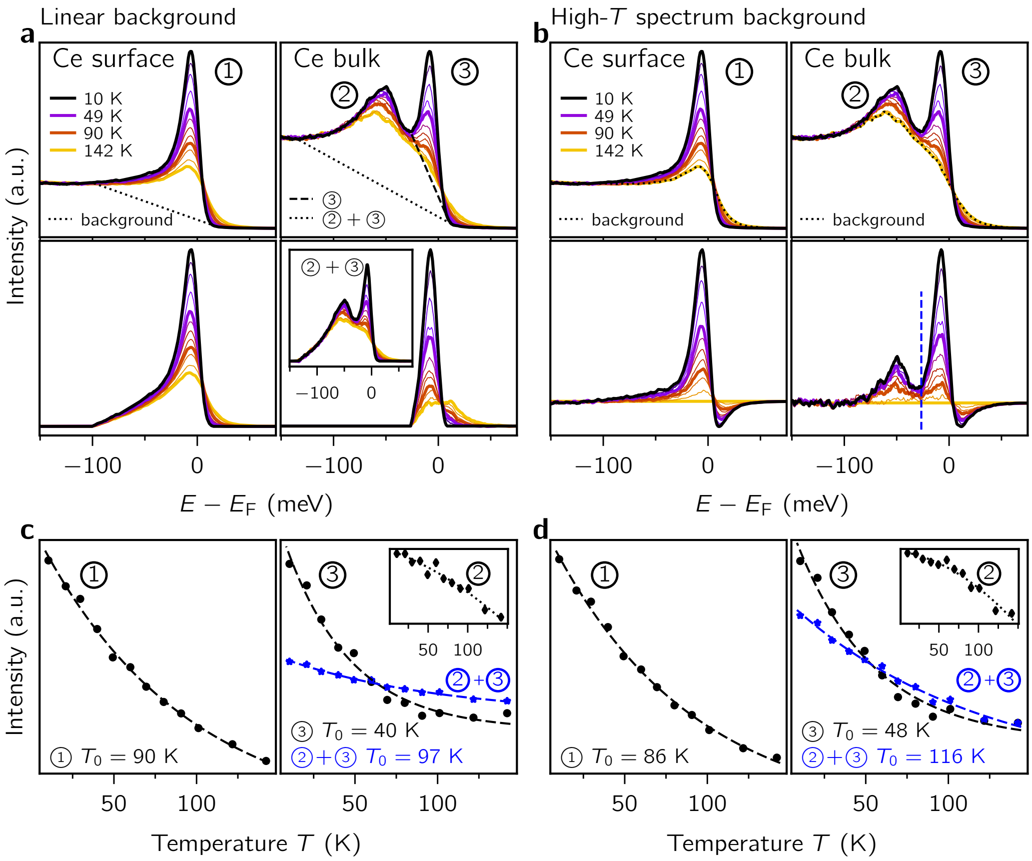

Figure 4.10: *Upper panels (a, b)*: k-integrated profiles of the $4f$-derived states for various T before (upper row) and after (lower row) subtraction of different backgrounds for Ce-terminated (left) and Si-terminated (right) surfaces with (a) linear background and (b) spectrum measured at highest T taken as background. In the upper row the used background is shown as black dotted and dashed lines. The hybridization peak for the Ce-terminated surface is labeled (1), while (2) and (3) refer to the side band and E_F peak in case of Si termination, respectively. In (a) different linear backgrounds were considered for the Si-terminated surface with one applied to the E_F peak (dashed line), and the other involving both the side band and the E_F peak (dotted line). The inset in the lower row shows the resulting spectra for the latter after background subtraction.
Lower panels (c, d): Integrated intensities of the hybridization peaks after subtraction of the (c) linear background and (d) high-T spectrum plotted over T. In case of the Si termination, integration over the E_F peak (3) in black, the side band (2) in the inset and both (2)+(3) in blue were performed. The separation into E_F peak (3) and side band (2) in (d) is indicated by a blue dashed line in (b). Exponential fits with the exponential attenuation T_0 are shown as black and blue dashed lines. The insets show the results for the side band (2) with a dotted line serving as guide to the eye.

background are henceforth used for this study.

Another aspect, which Figure 4.11 demonstrates, is that even though intensities

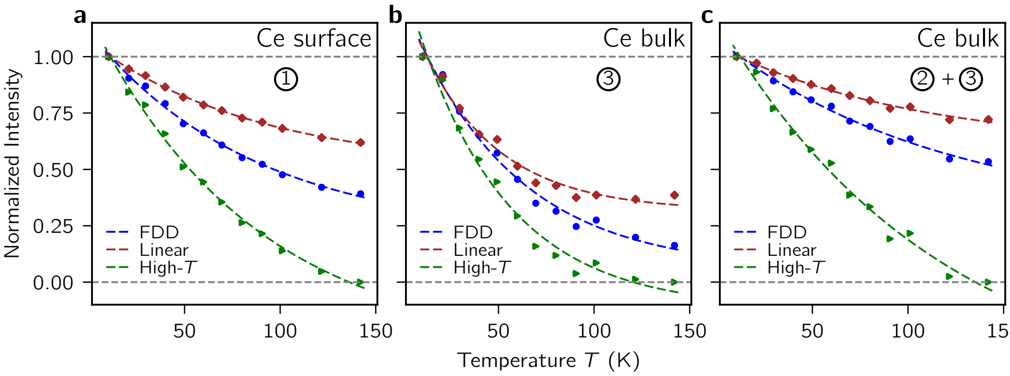

Figure 4.11: Peak intensity normalized to one at 10 K after FDD (blue), linear (dark red) and high-T (green) background subtraction with regards to T for (a) the hybridization peak of the Ce-terminated surface (1), (b) the E_F peak (3) and (c) the side band (2) plus the E_F peak (3) of the Si-terminated surface. The corresponding exponential fits are plotted in the same color as dashed lines.

vary strongly, all temperature behaviors of one peak follow nearly the same attenuation which underlines that T_0 is the ideal parameter to describe and compare the temperature behavior for the different terminations.

So far, an exponential function was used to describe the temperature behavior. However, the properties of Kondo problems are in some temperature range associated with a logarithmic temperature dependence (see Section 2.4), which calls into question the used exponential fitting. The reason for choosing an exponential function instead of a logarithmic one becomes obvious when plotting the intensities of the hybridization peaks (as determined by FDD subtraction) in logarithmic scale as shown in Figure 4.12. Here, a logarithmic temperature dependence would corresponds to a straight line while the intensity data deviates for low and high temperatures from such a line. Instead, only for a limited temperature range, an approximate linear behavior can be attributed to all three peaks in (a), (b) and (c), respectively.

The departure from a simple logarithmic temperature dependence is quite universal for properties of Kondo systems, and its origin is in so far trivial that a logarithmic dependence would result in a positive divergence of the property towards very low temperatures and a negative divergence towards high temperatures. However, since the properties of a Kondo systems remain finite, the logarithmic temperature behavior has to level out at high and at low temperatures. Hence, the temperature dependence of properties of Kondo systems follow in general a S-shaped curve. This shape can be directly seen in Figure 4.12(b), where the Kondo scale is shifted to small enough temperatures so that the the leveling out can be seen for high and low temperatures. While a logarithmic function cannot describe such an behavior, the exponential fit follows such an S shape and describes the experimental data nicely in the full investigated temperature

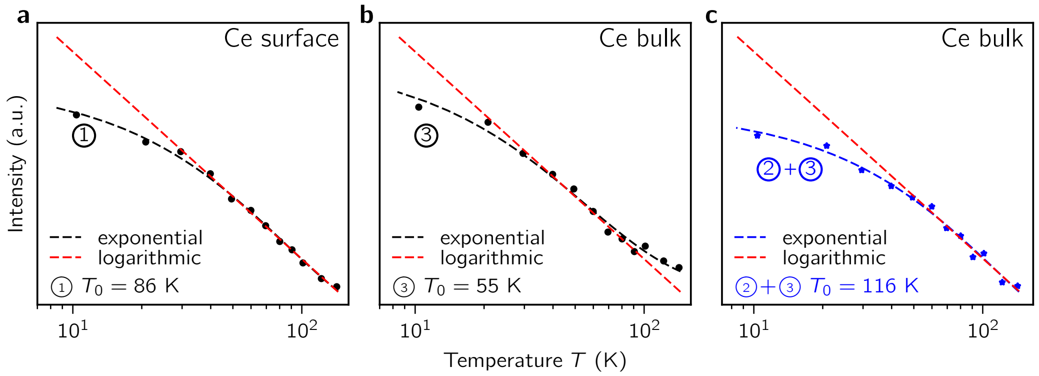

Figure 4.12: The peak intensities after FDD background subtraction in logarithmic T scale for (a) the hybridization peak (1) of the Ce-terminated surface, (b) the E_F peak (3) and (c) the total intensity of the E_F peak and the side band (2)+(3) of the Si-terminated surface. The black or blue dashed line corresponds to the exponential fit while the red dashed line corresponds to the logarithmic fit in the range of a logarithmic behavior.

range. As characteristic temperature of this behavior, we already introduced the exponential attenuation T_0. In a logarithmic temperature scale, this temperature corresponds exactly with the inflection point and thus T_0 corresponds to the center of the temperature range in which the experimental data follow a logarithmic behavior. In this way, the exponential attenuation T_0 connects the fitted exponential behavior of the measured data with the characteristic logarithmic behavior which is associated for Kondo problems over a limited T range making T_0 a good characteristic temperature. However, since the connection between T_0 and other Kondo scales is not known, we cannot directly connect our values to these scales and to the Kondo temperature T_K.

With the fact that a logarithmic function cannot describe the properties of a Kondo system over a large temperature range explored in detail, a justification for an exponential fit is still missing. For this reason, the exact results of a property of a Kondo system is compared to an exponential behavior. This property is the specific heat $C(T)$ of a single Kondo ion because it can be calculated numerically with high precision [100–102], and is in an indirect way related to the intensity of the E_F peaks since $C(T)/T$ probes the electronic density of states at the Fermi level. The exact numerical results for the normalized specific heat C/T of a single $S = 1/2$ Kondo ion are plotted with respect to the temperature in a logarithmic scale and with C/T scaled to T_K/R in Figure 4.13. The numerical results were provided to us by H.U. Desgranges [103]. Accordingly, the definition of T_K as used in [103] will be applied here.

The normalized specific heat C/T follows the aforementioned S shape. Around the inflection point of C/T in the logarithmic temperature scale at a temperature T_K/π, an exponential and logarithmic function can be applied. Clearly, the exponential function can reproduce the exact result quite nicely within one decade

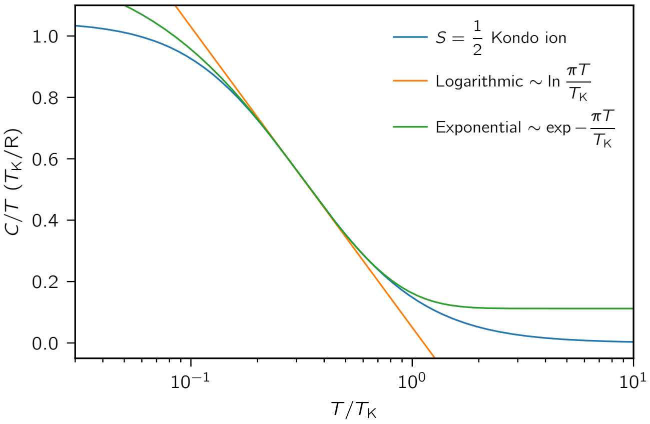

Figure 4.13: The exact numerical result for the specific heat C/T of the $S = 1/2$ single ion Kondo mode in a logarithmic T scale. C/T is normalized to T_K/R. The orange and the green lines are respectively a logarithmic and an exponential fit to the exact results in the vicinity of the inflection point.

in temperature around the inflection point. Because our measured temperature range corresponds to such an interval around the inflection point, a simple exponential function is able to describe the intensity behavior. On contrary, the logarithmic function can describe the temperature dependence only over a much narrower interval and is thus less suitable to be used for our analysis.

Having seen a clearly distinct temperature behavior between the two terminations, the question about the origin this difference remains. From experience of early photoemission studies of polycrystalline samples [14] it is known that T_K for the surface is always smaller than for the bulk. This is understood as a consequence of the reduced atomic coordination at the surface, which leads both to a reduction of the strength of $4f$-conduction band hybridization V and an increase of the $4f$ electron binding energy ε_f. Hence, the Kondo coupling constant $J \sim \frac{N_f V^2}{\varepsilon_f}$ is decreased, where N_f is the ground state degeneracy [14]. And with a decreased coupling J, the Kondo temperature $T_K \sim \exp\left(-\frac{1}{J}\right)$ (see Equation (2.19)) is decreased, too.

However, our observed temperature dependences of the E_F peaks suggest the opposite conclusion, meaning that the characteristic temperature T_0 of the Si-terminated surface ($\sim$ 55 K) is by a factor of one and a half smaller than that of the Ce-terminated surface ($\sim$ 86 K). As discussed before, the characteristic temperature T_0 cannot be directly associated with T_K, but a correspondence of a clearly larger T_0 to a larger T_K is expected. A close relation was found in [99], where the temperature dependence of the ARPES E_F amplitude of a specific point in k space was qualitatively similar to what is found here and compared well with the T dependence of the E_F amplitude of the k-integrated spectrum of a calculation using DMFT. This underlines that a difference in T_0 should reflect a change of T_K .

This new and unexpected difference in the surface and bulk values of T_0 can be traced to the reduction of the surface CEF splittings, pointed out already above. The exact values for the CEF splittings at the surface are not known, but they are certainly less than our energy resolution $\approx 10\,\text{meV} = 116\,\text{K}$. Within that framework, two limiting cases will be discussed below.

For the first case we simply note that, whatever the splittings are, the E_F peak intensity that we measured certainly includes that of the Kondo resonance and the CEF sidebands. Thus for the surface spectrum there is an increase of the effective degeneracy to $N_f = 6$ relative to that in the bulk spectrum ($N_f = 2$). We propose that the increase of N_f overcomes the effects of the decreased surface coordination so that the net effect is an increase of J, leading to an increase of T_K (and T_0). In support of this basic understanding, we observe that the T_0 value obtained for the bulk using the total intensity of the E_F peak and its CEF side band (curve (2+3) in Figure 4.9(d)) is $\sim$ 116 K, which is larger than the one obtained for the surface $\sim$ 86 K and is consistent with the expected effect of a reduced $\frac{\langle V^2 \rangle}{\epsilon_f}$ on the surface for constant N_f. Indeed, for the case of spin-orbit sideband features in impurity Anderson model, it was noticed long ago [85] that, although there is no rigorous proof, numerical calculations indicate that the total weight of the near E_F resonance, including its spin-orbit sideband, is roughly the same as would occur if the spin-orbit splitting were zero with no other change in the parameters, in which case T_K would be much larger and all the weight would lie in the E_F peak. This property should be essentially the same for the CEF sidebands.

The argumentation of the first case nicely reconciles the basic finding of a larger characteristic temperature for the E_F peak of the surface spectrum than for that of the bulk. But the discussion can be extended to a stronger and more interesting limiting case as follows. Working in the framework of the impurity Anderson model, Cornut and Coqblin [104] showed that as increasing T successively populates excited CEF states, the effective T_K is successively increased as N_f is successively increased. Since the CEF splittings all lie within the T range of our measurements, one might expect fairly abrupt changes in the peak shape or temperature dependence to accompany such jumps in T_K. However, as Figure 4.9(a,c) shows, neither of these changes can be observed and the temperature dependence looks qualitatively similar to that of the bulk, where no CEF states become occupied in the measured temperature range. This suggests that the CEF splittings could be as small as the lower limit of our T range, $\sim$ 1 meV, in which case, over the T range of our measurements, the CEF splittings can be entirely neglected so that the ground-state degeneracy is effectively $N_f = 6$. That the CEF splittings could be so small is consistent with our argumentation above for the role of the changed symmetry on the surface. In this case there will be a significant T range for which the surface magnetic moment remains Kondo quenched well after the bulk magnetic moments have begun to manifest.

Finally, we note that besides the degeneracy N_f, the Kondo temperature further depends on the density of the itinerant states at E_F to which the local $4f$ states can couple. Indeed, a much larger density for the Ce-terminated surface would have the same effect as the increase of the degeneracy N_f. However, while one might expect small differences, our measurements as well as ab-initio band structure calculation do not point to any strong discrepancies in the density of states at E_F for the two terminations. Therefore, the density of states does not seem to be main origin of the unexpected characteristic temperature relations.

4.2.4 Dispersion model

With the concentration on the angle-integrated photoemission profiles, no statements about the dispersion of the Kondo peak are possible. Additionally, for the background subtraction in Section 4.2.3, no model was applied to describe the obtained profiles in a more sophisticated way. The main reason for that was the complexity of the peak shapes which makes it impossible to reliably model and achieve convergence with a fitting procedure. This can be understood since an integration over strongly dispersive bands as seen around the $\overline{\Gamma}$ point in Figure 4.5(a,b) leads to non-Lorentzian peak shapes in the profiles that cannot be described in a simple manner. However, this problem can be circumvented by fitting individual profiles which are obtained by integrating over tiny angle intervals. This way, the peak shapes still closely resemble Lorentzians but the main disadvantage of this approach is the strongly reduced signal-to-noise ratio of the profiles. Therefore, a fit procedure is needed that can fit multiple of these profiles simultaneously in a correlated manner to increase the underlying information.

Starting point of such a fitting procedure is the general approach to model the intensity $I^{term}(\Phi, E, T)$ of the measured spectrum of a single surface termination based on Equation (3.13) at temperature T with the emission angle Φ and the kinetic energy E as

$$I^{term}(\Phi, E, T) = \big(f(E - E_\mathrm{F}, T)\, A^{term}(\Phi, E, T)\big) * G(\sigma_E, E, T) + I^{term}_{\mathrm{bkgd}}(\Phi, E, T) \tag{4.1}$$

with the FDD $f(E - E_\mathrm{F}, T)$ multiplied by the spectral function A^{term}, a convolution with a Gaussian G due to a finite resolution σ_E and an addition of the background I^{term}_{bkgd}. By concentrating our evaluation around $\overline{\Gamma}$, the variations in the matrix elements can be neglected.

To model the spectral function A, a number of Lorentzian peaks L is needed. First, a broad peak L_{val_1} for the underlying valence bands and a narrow peak L_{val_2} to model the strong valence band emission at the Fermi level. For the $4f$ emissions, one Lorentzian L_K is added to model the Kondo peak above the Fermi level as well as L_SO for the spin-orbit satellite between −300 meV to −250 meV. In case of the Si-terminated surface, an additional peak L_SB is added to account for the side band. Because dispersive bands will be modeled, the aforementioned Lorentzians should change based on the emission angle Φ, and since the electronic structure changes with temperature, they should further depend on the the temperature T. Hence our spectral structure A takes the form

$$A^{term}(\Phi, E, T) = \sum L_i^{term}(\Phi, E, T) \tag{4.2}$$

with L_i^{term} being the Lorentzians for the corresponding surface termination, i.e. $term =$ Si or Ce.

However, to reduce the number of free parameters of the fit and achieve convergence, constraints need to be set. Since the underlying valence band emission should not depend strongly on the temperature T, the corresponding Lorentzians L_{val_i} will not depend on T ($L_{\mathrm{val}_1} = L_{\mathrm{val}_1}(\Phi, E)$, $L_{\mathrm{val}_2} = L_{\mathrm{val}_2}(\Phi, E)$). Additionally, the T dependence of the side band, which is small in comparison to that of the E_{F} peak, can be neglected with $L_{\mathrm{SB}}^{\mathrm{Si}} = L_{\mathrm{SB}}^{\mathrm{Si}}(\Phi, E)$. As final assumption, the spin-orbit satellite L_{SB} will not change with Φ and T as this peak is far below E_{F} and nearly non-dispersive. Then the spectral function is defined as

$$A^{\mathrm{Ce}}(\Phi, E, T) = L_{\mathrm{val}_1}^{\mathrm{Ce}}(\Phi, E) + L_{\mathrm{val}_2}^{\mathrm{Ce}}(\Phi, E) + L_{\mathrm{K}}^{\mathrm{Ce}}(\Phi, E, T) + L_{\mathrm{SO}}^{\mathrm{Ce}}(E) \tag{4.3}$$

$$A^{\mathrm{Si}}(\Phi, E, T) = L_{\mathrm{val}_1}^{\mathrm{Si}}(\Phi, E) + L_{\mathrm{val}_2}^{\mathrm{Si}}(\Phi, E) + L_{\mathrm{SB}}^{\mathrm{Si}}(\Phi, E) + L_{\mathrm{K}}^{\mathrm{Si}}(\Phi, E, T) + L_{\mathrm{SO}}^{\mathrm{Si}}(E) \tag{4.4}$$

As second step, the background term I_{bkgd} needs to be defined. To model the contribution of inelastic scattering, a simple smooth function based on the integral background was added. Although the inelastic scattering does not preserve momentum, the overall shape of the background should follow in first approximation the same shape as a Shirley background, but with an emission angle dependent scaling factor $\alpha(\Phi)$. In the case of the Ce-terminated surface, a small contribution of the deeper Ce layers to the measured spectrum can be expected. To account for this contribution in our model, the measured intensity of the Si-terminated surface $I_{\mathrm{measured}}^{\mathrm{Si}}$ is added to the background with a scaling factor β since the spectrum from the deeper Ce layer should be very similar to the spectrum of the Si-terminated surface. Additionally, the background term can compensate any unwanted small admixtures of the Si-terminated surface to the measured Ce-terminated surface spectrum. As this contribution might change with temperature due to slight changes of the beam spot on the sample, the scaling factor $\beta(T)$ is temperature dependent. The background I_{bkgd} is thus defined as

$$I_{\mathrm{bkgd}}^{\mathrm{Si}}(\Phi, E, T) = \alpha^{\mathrm{Si}}(\Phi) \int_{\infty}^{E} f(E' - E_{\mathrm{F}}, T) A^{\mathrm{Si}}(\Phi, E', T) dE' \tag{4.5}$$

$$I_{\mathrm{bkgd}}^{\mathrm{Ce}}(\Phi, E, T) = \alpha^{\mathrm{Ce}}(\Phi) \int_{\infty}^{E} f(E' - E_{\mathrm{F}}, T) A^{\mathrm{Ce}}(\Phi, E', T) dE' + \beta(T) I_{\mathrm{measured}}^{\mathrm{Si}} \tag{4.6}$$

Lastly, this model is applied to a number of small angle slices of the measured ARPES spectra, consisting of the summation over three energy distribution curves (EDCs), which corresponds to an angular integration over 0.15°, in contrast to the integration over 4° that was used in Section 4.2.3. For convergence in reasonable time, the number of slices was set to 21, meaning slices for angles $\Phi \in [-1.5, 1.5]$ centered on the $\overline{\Gamma}$ point for each termination. Minimizing the total residual of all angles at all measured temperatures for both terminations, shared parameters between multiple spectra can be determined with high precision in a small number of iterations. For instance, E_F should have the same value for all temperatures, angles and terminations. Hence, E_F is determined by optimizing 504 (21 slices × 2 termination × 12 temperatures) spectra simultaneously, which allows us to gain a sound initial insight even in the region above E_F where the signal-to-noise ratio is small.

However, fitting a Lorentzian peak above E_F is still problematic as nearly the same peak after multiplication with the FDD can be achieved by simply moving the peak further away from E_F and changing the amplitude and width of the Lorentzian, which leads to many local minima. Thus, the degrees of freedom of L_K need to be reduced by either setting the amplitude or the width temperature independent (but still variable with Φ). Fast convergence was achieved with a temperature-independent width, which is reasonable, because a strong temperature-dependent change is expected for the amplitude with the formation of the Kondo resonance. The model was implemented in PYTHON with the least-squares optimizing routine of the SCIPY library [105] using the *Trust Region Reflective* method which is based on [106]. Reasonable bounds were defined for all parameters. The standard deviations of the obtained parameters were estimated by using the modified Jacobian matrix at the solution. The resulting fit is shown for one angle slice Φ in Figure 4.14.

The position of the L_K peak at 21 K is shown in Figure 4.15(c,d) for the Ce- and Si-terminated surface, respectively. At this temperature, which is significantly below T_0, clear and different dispersive structures can be seen when comparing both terminations. At 10 K, the FDD becomes very narrow and the full pattern of the dispersive structure cannot be resolved as good as at 21 K, but the dispersions for 21 K and 10 K still look qualitatively similar showing a weakly dispersive arch-like structure for the Ce-terminated and a cone-like structure for the Si-terminated surface. This difference cannot be explained just by differences in the hybridization strength that lead to narrower or broader dispersions, but instead the Kondo peak must be formed by the hybridization with different bands.

To explore the question of the coupling of the $4f$ to different valence bands for the two terminations, a simple hybridization model could give further inside. For a hybridization model, a number of unhybridized bands are needed for the initial states. In our case, this would mean a localized $4f$ band at an energy ε_f as well es a number of dispersive valence bands with their k-dependent energy $\tilde{\varepsilon}_k$. For the Si-terminated surface, a hole-like band can be seen in Figure 4.5(b) and was already discussed as participating in the hybridization in the context of the formation of the side band. By coupling with the localized $4f$ states, the hole-like band will push the $4f$ state to higher energies, which can be seen in the fitted dispersion of the Kondo peak, while on the other hand the avoided crossing

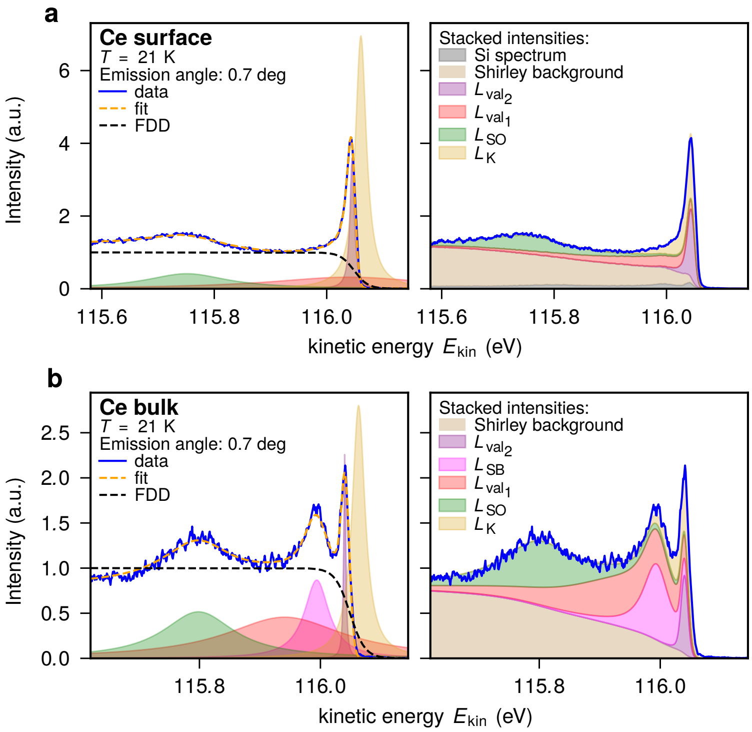

Figure 4.14: Measured intensity profiles and fits at an angle slice around the emission angle of 0.7° at 21 K for a (a) Ce- and (b) Si-terminated surface. The left panel shows the measured profile (blue), the result of the corresponding fit (orange), the FDD (black) and the Lorentzian peaks used for fitting. The right panel shows the same data, but the Lorentzian peaks are shown as stacked plots after multiplication with the FDD and resolution convolution added onto the background of the fit.

will push the hole-like itinerant band to lower energies. Therefore, this band as well as the local $4f$ level are the obvious candidates for such a two band model with the both initial unhybridized bands shown in Figure 4.15(b). Note that a similar behavior was observed for a CEF state in the heavy-fermion compound $\mathrm{YbRh_2Si_2}$, which lies below E_{F} and is pushed above E_{F} by hybridizing with a hole-like valence band [107]. For the Ce-terminated surface, the participating valence bands are not as obvious to identify. The off-resonance spectrum, which is shown in Figure 4.4 shows strong emission at E_{F} stemming from electron-like valence bands at E_{F}. Testing such a band in the hybridization model with the localized $4f$ level, a dispersive structure as obtained by fitting the data can be reproduced. However, adding a second electron-like band achieves an even better agreement. The DFT calculations, which will be discussed later in this section, show that there are indeed two electron-like bands for the Ce-terminated surface which can couple to the $4f$. With these two bands, which are shown in Figure 4.15(a) as well as the $4f$ level, all initial bands for the hybridization model are defined. These states can be described in an non-interactive Hamiltonian H_0 defined as

$$H_0 = \sum_{i,k} \tilde{\varepsilon}_{i,k} c^{\dagger}_{i,k} c_{i,k} + \sum_{k} \varepsilon_f f^{\dagger}_k f_k \tag{4.7}$$

by summing over all valence bands with the corresponding annihilation operators c_i and their energies $\tilde{\varepsilon}_i$ and adding the one local state at energy ε_f with the annihilation operator f.

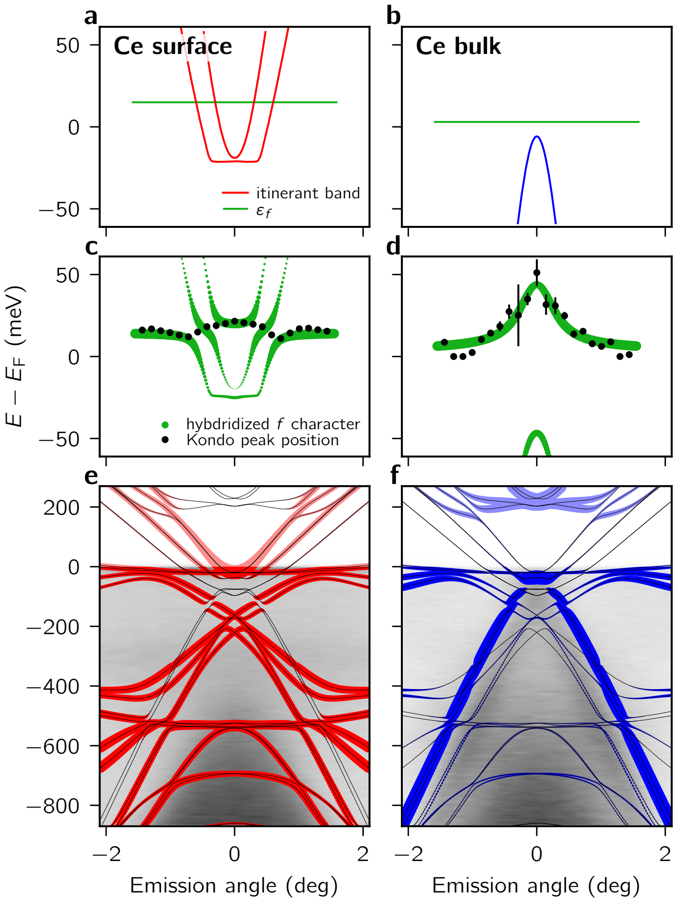

Figure 4.15: Hybridization model with the unhybridized states showing the localized state ε_f in green and the (a) two electron-like bands in red for the Ce-terminated surface and (b) one hole-like band in blue for the Si-terminated surface. The f character of the hybridized bands for the (c) three-band model ($V = 10\,\text{eV}$, $\varepsilon_f = 15\,\text{meV}$) and (c) two-band model ($V = 40\,\text{meV}$, $\varepsilon_f = 3\,\text{meV}$) superimposed by the derived Kondo peak dispersion for $T = 21\,\text{K}$ for the respective terminations. The results of the ab-initio band-structure calculations are further shown with the itinerant bands stemming from the first few layers of the (e) Ce-terminated surface shown in red and of the (f) Si-terminated surface shown in blue. Note that the calculated bands are slightly shifted upwards (55 meV) in order to coincide with the ARPES data taken off-resonance ($h\nu = 112\,\text{eV}$) and shown as gray-scale background.

By introducing an interaction term H_I with a coupling constant V between the itinerant and local bands of the form $V_i c^\dagger_{i,k} f_k + h.c.$, the bands can hybridize. For simplicity, a k- and band-independent coupling constant V will be used. This results in the full Hamiltonian

$$H = H_0 + H_\mathrm{I} = \sum_{i,k} \varepsilon_{i,k} c^\dagger_{i,k} c_{i,k} + \sum_k \varepsilon_f f^\dagger_k f_k + V \sum_{i,k} \left(c^\dagger_{i,k} f_k + h.c. \right) \tag{4.8}$$

which can be diagonalized to gain the eigenstates and eigenenergies. Note the similarity of this Hamiltonian to the more complex impurity Anderson Hamiltonian in Equation (2.17) which further contains the Coulomb repulsion term, which is neglected for this simple approach. The f character of the hybridized bands is shown in green in Figure 4.15(c,d) for both terminations. The coupling constant V as well as the energy level of the $4f$ was changed in such a way that it agrees nicely with the obtained dispersion from the fit model at 21 K shown in black superimposed on the hybridization model. For the Ce-terminated surface, the used parameters are $V = 10\,\mathrm{meV}$, $\varepsilon_f = 15\,\mathrm{meV}$ and for the Si-terminated surface $V = 40\,\mathrm{meV}$, $\varepsilon_f = 3\,\mathrm{meV}$. While the exact values of these parameters have to treated with caution, the overall trend corresponds nicely with our study so far. For the Ce-terminated surface, the coupling and thus the interaction is weaker as expected due to the reduction of the atomic coordination at the surface. The absolute position of the Kondo resonance needs to be interpreted carefully due to restrictions in the fit model, however, the Kondo resonance seems to be shifted to higher energies for the Ce-terminated surface, which would be in accordance with a larger T_K.

To explore the origin of the itinerant bands which couple to the $4f$, ab-initio band structure calculations were performed. This was done in the framework of DFT within the LDA using FPLO [108]. To account for the surface sensitivity of UV-ARPES and thus the two distinct terminations, an asymmetric slab of 16 atomic layers was considered, having one surface terminated with the Si layer and the other side with the Ce layer to account for the possible surface terminations. For the lattice parameters and atomic positions, experimental data were used and the four outermost layers were additionally force minimized along the surface normal to include surface relaxation effects. The Ce $4f$ states were moved from the valence basis to the core (open core approximation) and the occupancy of all $4f$ states was set equal with a total occupancy of one.

The resulting band structure is shown in Figure 4.15(e,f) for both terminations in black lines. To see, which bands stem from what surface, the weights of the different orbitals which form the bands were added up for different atomic layers. In case of the Ce-terminated surface, the weights of all orbitals from the four topmost layers (Ce-Si-Rh-Si) were added and shown as red fat bands. For the Si-terminated surface, the weights of the three topmost layers of the Si-terminated side of the slab (Si-Rh-Si) were added and shown in blue fat bands. As gray scale, the measured off-resonance spectrum ($h\nu = 114\,\mathrm{eV}$) is shown under the calculated bands. To achieve a good agreement between the calculations and measurements, E_F of the computed bands is shifted by 55 meV.

Clearly visible in the DFT calculations are the two electron-like bands of the Ce-terminated surface which were used in the hybridization model. Indeed, in case of the Si-terminated model, these bands are not observed. Instead, the hole-like band is strongly visible, being pinned to E_F. A similar, but more complex hole-like band can be also seen for the Ce-terminated surface, however at higher binding energies far away from E_F. Therefore, with the help of the ab-initio calculations, the main bands that hybridize with the $4f$ have been identified.

4.2.5 Summary and outlook

Our above presented findings showed that it is possible to disentangle the different surface and bulk contributions to the Kondo scale at a high level of detail, and may also provide an important clue in the better understanding of the Kondo problem when including a CEF term. Thereby our study brings into reach the ultimate goal of quantitatively testing many-body theories that link spectroscopy and transport properties, for both the bulk and the surface, separately.

The fact that two clearly different Ce environments were found and measured may give insight into the more general problem of a Kondo lattice with two different local moment sublattices. Theoretically, this problem was studied [76], indicating a complex behavior with either competing or cooperative Kondo effects depending on the model parameters. With the discovery of the coexistence of AFM order and superconductivity in the heavy-fermion systems Ce_3PdIn_{11} [109] and Ce_3PtIn_{11} [110], this problem gained relevance. These compounds contain two crystallographic different Ce sites, raising the question if one site is responsible for the AFM order and the other one for the superconductivity. However, separating the contributions and properties of the different Ce sites turned out to be complicated and not totally decisive.

With our study, independent insight into the correlated electronic states of each site is possible. No evidence for an interplay between the Kondo effects at the different Ce sites was found as the temperature behavior differs over the whole temperature range. Further, with bands which hybridize with the $4f$ states being different, a strong direct cross talk between the Kondo effects on the different sites should not be possible. A similar situation might prevail in compounds with different Ce sublattices, and could be one of the reasons why clear evidences for a cross talk of Kondo effects in such systems are yet lacking.

4.3 Surface region of $CeCo_2P_2$

4.3.1 Introduction

Having studied $CeRh_2Si_2$, we focused on the complementary system $CeCo_2P_2$. Instead of a magnetic order of the Ce $4f$ moments, in $CeCo_2P$ the cobalt sublattice orders antiferromagnetically at a very high temperature of 440 K while the Ce $4f$ sublattice behaves passive and shows no sign of heavy-fermion physics.

In Figure 4.16(a) we illustrate the bulk unit cell of $CeCo_2P_2$. As shown, the magnetic moments of the Co atoms order ferromagnetically within the *ab* planes and stack in AFM fashion along the *c* axis [111]. The Ce atomic layers are separated by P-Co-P blocks. The bulk properties of $CeCo_2P_2$ and isostructural lanthanide materials $LnCo_2P_2$ were intensively studied in the past [111–113]. It was established that their properties can be elucidated from the cell volume analysis, or more explicitly, from the distance between the phosphorus atoms, $d_{\mathrm{P-P}}$ along the *c* axis. For $CeCo_2P_2$, the $d_{\mathrm{P-P}}$ value of 2.45 Å, labeled in Figure 4.16(a), is similar to the native P-P single bond length of 2.21 Å. The cell volume of $CeCo_2P_2$ is considerably smaller than that of the isostructural lanthanide materials as $LaCo_2P_2$, $PrCo_2P_2$ and $NdCo_2P_2$. In these neighboring systems, the lanthanides are found in a trivalent state Ln^{3+} with magnetic order not only on the Co sites but in the case of Nd and Pr on the lanthanides, too. In that regard, the apparent anomaly in the cell volume, the short $d_{\mathrm{P-P}}$ distance, the missing magnetic order on Ce as well as a much higher T_{N} for $CeCo_2P_2$ [111–113], gives reason to describe Ce as being close to the tetravalent Ce^{4+} with a non-magnetic $4f^0$ configuration.

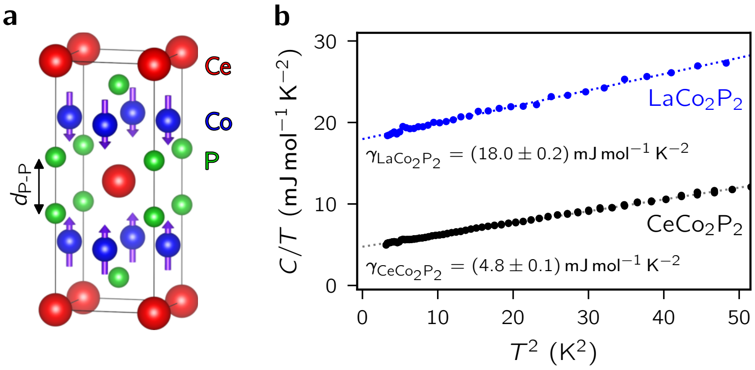

Figure 4.16: (a) Tetragonal crystal structure with short P-P bonds along the *c* axis. The long-range antiferromagnetic order at $T_{\mathrm{N}} = 440$ K is due to magnetic $3d$ ions of cobalt. (b) The Sommerfeld-coefficients $\gamma_{\mathrm{LaCo_2P_2}}$ and $\gamma_{\mathrm{CeCo_2P_2}}$ are determined from the heat-capacity measurements $C(T)$ between 1.8 and 10 K.

This is in agreement with recent magnetization data on $CeCo_2P_2$ single crystals [114], which show a small temperature independent susceptibility below 300 K incompatible with local $4f$ moments. Further evidence for a tetravalent behavior of the Ce $4f$ in the bulk of $CeCo_2P_2$ comes from the heat-capacity measure-

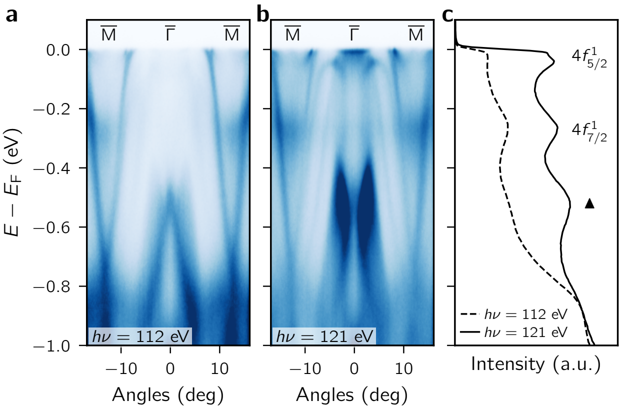

Figure 4.17: Comparison of the ARPES spectra taken from the P-Co-P surface of $CeCo_2P_2$ with photon energies of (a) 112 eV and (b) 121 eV along the $\overline{M}$–$\overline{\Gamma}$–$\overline{M}$ direction at 7 K. (c) Photoemission (PE) spectra integrated over the shown ARPES data.

ments presented in Figure 4.16(b). There we show C/T as function of T^2 at low temperatures for both $LaCo_2P_2$ and $CeCo_2P_2$. From these data, the Sommerfeld coefficient of $CeCo_2P_2$ was determined, $\gamma_{CeCo_2P_2} = 4.8(1)\,\mathrm{mJ\,mol^{-1}\,K^{-2}}$, which is even smaller than the value found for $LaCo_2P_2$, $\gamma_{LaCo_2P_2} = 18.0(2)\,\mathrm{mJ\,mol^{-1}\,K^{-2}}$, where no contributions from $4f$ electrons are present. Both values are typical for intermetallic systems without strongly-enhanced effective masses and prove the absence of sizable Kondo interactions in the bulk of $CeCo_2P_2$. While a formal tetravalent configuration is only expected in insulating compounds [14] and thus a strongly hybridized intermediate Ce can be expected, the $4f$ properties are reminiscent of a tetravalent configuration and therefore we will from hereon describe $CeCo_2P_2$ as behaving tetravalently without claiming that the Ce is in a full tetravalent configuration. In the following, the properties of Ce at the surface determined by ARPES measurements will be presented.

4.3.2 Electronic structure characterization

Let us turn to the results of ARPES measurements performed on $CeCo_2P_2$ at a temperature of 7 K. Due to its layered structure, it is anticipated that $CeCo_2P_2$ predominantly cleaves between Ce and the P-Co-P trilayer block. Therefore, we expect the surface of the cleaved samples to consist of a mosaic of P- and Ce-terminated terraces. To emphasize the Ce-$4f$ emission, we used the cross-section effect of the Ce $4f$ resonance allowing fo a resonant enhancement of the Ce-$4f$ emission with photon energies of around 121 eV, corresponding to the Ce $4d \rightarrow 4f$ X-ray absorption threshold [14]. It is worth noting that at these photon energies the inelastic mean free path of the photoelectrons is only of the order of 5 Å, making these measurements only sensitive to the Ce layers close to the crystal surface.

In Figure 4.17(a,b), we present the ARPES data taken from a freshly cleaved surface of $CeCo_2P_2$ along the $\overline{M}$–$\overline{\Gamma}$–$\overline{M}$ direction for photon energies of $h\nu = 112\,eV$ and $h\nu = 121\,eV$, respectively. Scrutinizing first the off-resonance ARPES data shown in Figure 4.17(a), we find widely-extended parabolic electron-like bands residing around the $\overline{M}$-points. These states are Shockley-type surface-electron states that spread through the topmost P-Co-P-Ce surface block and will be theoretically discussed later in the framework of our DFT calculations. The surface states look similar to those found in the isostructural RET_2Si_2 materials which were intensively studied in the recent past by us [115–120]. Similar to $CeRh_2si_2$, surface states around the $\overline{M}$ point are intrinsic features of the P-terminated $CeCo_2P_2$ crystal and are missing for the Ce-terminated surface. An additional hole-like band can be seen centered at the $\overline{\Gamma}$-point with its maximum at an energy of $-0.5\,eV$. Close to the Fermi level (E_F) the ARPES spectrum does not show a rich spectral pattern. This, however, is changing strongly when tuning the photon energy to the $4f$ resonance as will be shown in the following.

To understand the $4f$-derived spectral pattern, we will first look at the angle-integrated spectra shown in Figure 4.17(c) which were obtained through summation of the k-distributed spectral weight of the off- and on-resonance ARPES data. In the energy interval down to $-1\,eV$, three peaks can be seen and attributed to the $4f$ emission. We resolve a $4f^1_{5/2}$ peak at E_F with its $4f^1_{7/2}$ spin-orbit split satellite seen at about $-280\,meV$ as well as a strong emission at around $-0.5\,eV$ marked with a solid triangle. The quite obvious and strong observation of $4f$ photoemission signals and particularly the appearance of a $4f^1_{5/2}$ peak, which is usually attributed to the tail of the Kondo resonance, allows us to conclude that the studied system, namely the P-terminated surface of $CeCo_2P_2$, cannot be in a tetravalent $4f^0$ state and behaves strongly different to what would be expected from the bulk. Especially the observation of flat and therefore heavy bands at E_F is not compatible with the small Sommerfeld coefficient $\gamma_{CeCo_2P_2}$. Since, as a result of the short mean free path of the photoelectrons, the $4f$ photoemission spectrum is dominated by emissions from Ce atoms below the outermost P-Co-P block, we can conclude that the properties of this subsurface Ce layer must differ significantly from those of the bulk.

The third $4f$ feature observed at around $-0.5\,eV$ and marked by the solid triangle can be explained within the Anderson model as a $4f^0$ derived hybrid. While the $4f^1$ structure described above is a $f-d$ hybridization effect with a related configurational mixing that admixes $4f^0$ character to the $4f^1$, the $4f^1$ photoionization results in the $4f^1 \rightarrow 4f^0$ final state at higher binding energies, too. This is a consequence of the strong on-site Coulomb interaction due to the strong spatial localization of the Ce-$4f$ orbitals, which is not properly described in band structure theory, but should be handled in light of the Anderson model [121]. The fact that its occurrence in the shown part of the spectrum is limited to a region close to the $\overline{\Gamma}$-point and that its binding energy deviates significantly from the value of 2 eV usually observed for Ce systems is related to the complex band structure and the k-dependent mixing of the $4f^0$ and $4f^1$ configurations. An explanation requires a detailed analysis in the framework of a periodic Anderson model, which

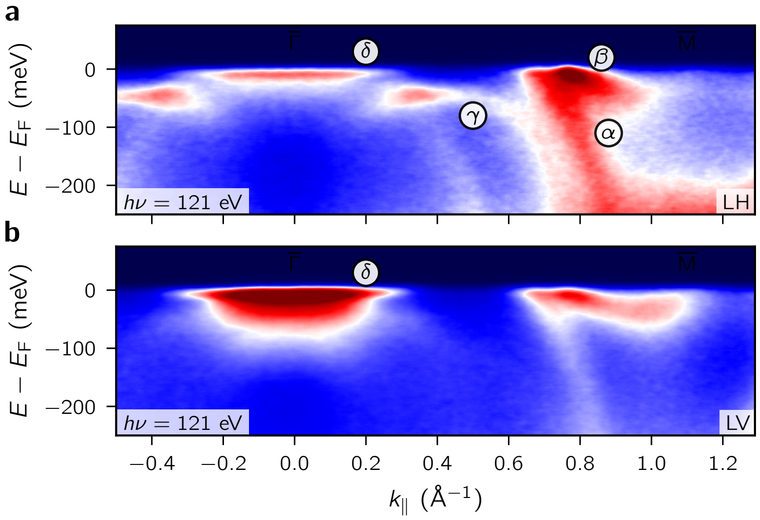

Figure 4.18: Comparison of the ARPES data taken from P-terminated CeCo$_2$P$_2$ with photon energies of 121 eV using (a) linear horizontal (LH) and (b) vertical (LV) light polarization. The data were obtained along the $\overline{\mathrm{M}}$–$\overline{\Gamma}$–$\overline{\mathrm{M}}$ direction at 7 K.

is beyond the scope of the present work and will be presented in a forthcoming publication.

Let us now return to the $4f^1$ emission and discuss in detail the observed f-derived bands at E_F, which can be well seen in the on-resonance ARPES band maps shown in Figure 4.18(a,b). The enlarged section around the E_F region measured with linear horizontal (Figure 4.18(a)) and linear vertical (Figure 4.18(b)) light polarization with respect to the storage-ring plane allows us to comprehensively study the electronic structure and unveil electronic states with different parities with respect to the incidence plane which intensities could otherwise be suppressed. Comparing the spectra of both light polarizations, we observe a clear dichroic behavior of the f-derived spectral features underlining a well-defined hybridization with the valence band with distinct orbital compositions. Further, our DFT calculations, which will be discussed later, indicate that all labeled features in Figure 4.18 reveal surface properties. The first of these features is the band α, which seems to have a partner labeled as the band β. Both bands show quite similar properties, they are both parabolic, electron-like and centered around the $\overline{\mathrm{M}}$-point. The minimum of the β band is not well seen in ARPES. Further, we resolve a hole-like band, called γ which has its valence-band maximum at about 50 meV below E_F. Finally, there is a spectral feature labeled δ which can be seen near E_F. It is centered at the $\overline{\Gamma}$-point and shows with its flat dispersion the intrinsic property of heavy-fermion systems. Based on the calculated charge density distributions, we conclude that the bands δ and γ reveal a surface-resonant behaviour while α and β are surface states situated in the bulk band gap around $\overline{\mathrm{M}}$. Keeping in mind that the Co in the P-Co-P-Ce surface block is ferromagnetically ordered, α

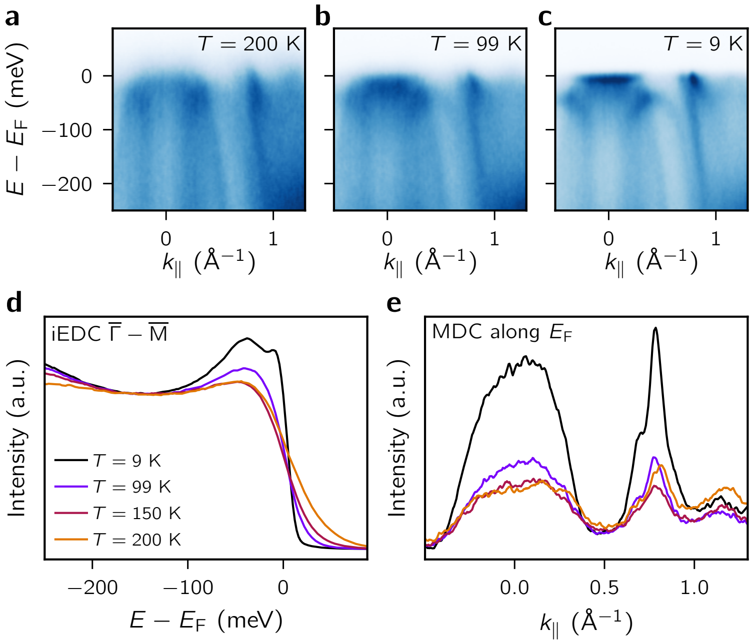

Figure 4.19: (a)-(c) Temperature dependence of the k-resolved Ce $4f$-derived states taken along $\overline{\Gamma}$–$\overline{\mathrm{M}}$ direction. (d) Temperature dependence of the integrated PE spectra over the shown ARPES patterns. (e) The same as in (d) but for the MDC spectra integrated near the E_F.

and β can be understood as a pair of spin-split bands due to the strong exchange interaction of the FM Co lattice. The strong Ce-$4f$ contribution to the spin-split α and β bands implies an interesting interlayer magnetic coupling between Ce and Co layers.

4.3.3 Temperature-dependent behavior

While the weakly-dispersive and strongly-localized $4f$ emission at E_F clearly indicates heavy-fermion behavior, additional support can be found when looking at its temperature dependence. In Figure 4.19(a) we display the evolution of the electronic structure near E_F taken with $h\nu = 121$ eV at 200, 99 and 9 K along the $\overline{\mathrm{M}}$–$\overline{\Gamma}$–$\overline{\mathrm{M}}$ direction. They clearly illustrate how the $4f$ spectral structure emerges for the discussed bands. By decreasing the temperature from 200 K, the initially hidden spectral features near E_F gradually sharpen into the clear picture where the weakly dispersive $4f$-derived bands are well resolved. The absence of any strong $4f$ contribution at higher temperature becomes obvious when looking at the integrated PE profile shown in Figure 4.19(d). There, we can clearly see how the E_F peak emerges upon reducing the temperature down to 9 K.

Similar temperature dependences were not only observed for $\mathrm{CeRh_2Si_2}$ (see Section 4.2), but are commonly measured for other f materials and canonical heavy-fermion systems, e.g. as seen for $CeCoIn_5$ [122] and $CeRhIn_5$ [123], as well as for the famous "hidden-order" material URu_2Si_2 [124]. However, in contrast to the just mentioned three materials, which exhibit the exotic f-related properties in the bulk, $CeCo_2P_2$ behaves tetravalently in the bulk as shown before. Hence, its Ce $4f$-derived spectral structure and temperature dependence are intrinsic only to the P-Co-P-Ce surface and thus, have a true two-dimensional (2D) origin. The key issue for understanding the appearance of this 2D Kondo lattice within the P-Co-P-Ce surface block is the strong reorganization of the electronic structure linked with the symmetry breaking of the AFM order of the Co lattice at the surface as discussed later. Thus, our experimental data might indicate that there is a significant cross talk between the FM Co layer with the Ce 2D Kondo lattice.

4.3.4 X-ray absorption measurements

For directly probing the moments of the Ce $4f$, we performed XMCD measurements. The measurements were performed at the La and Ce $M_{4,5}$ absorption edges of $LaCo_2P_2$ and $CeCo_2P_2$ at low temperature, $T = 5\,\mathrm{K}$, and in an applied field of 9 T at the ID32 XMCD branch at the ESRF. The spectra were taken at a grazing angle of 65° using the total electron yield and are thus strongly surface sensitive. The results are shown in Figure 4.20(a,b). For $LaCo_2P_2$, no clear XMCD signal was detected at either edge, as expected. In comparison, $CeCo_2P_2$ shows a sizable XMCD signal at both edges which changes sign when reversing the field direction. At the M_4 edge, where the XMCD signal is strongest, it reaches a size as high as 5 % of the X-ray absorption signal. The clear presence of an XMCD signal directly shows that the Ce atoms, unlike their La counterparts, do not behave in a strictly tetravalent matter across all probed layers.

While the presence of an XMCD signal clearly implies a magnetic moment on Ce, we cannot make a clear statement about the local origin of this signal. Due to the small free path of the electrons measured in total electron yield, the recorded signal originates mostly from the first few Ce layers. Since there is no clear way to distinguish the two surface terminations in X-ray absorption, we cannot exclusively assign the XMCD signal to the subsurface Ce layer of the P-terminated surface. However, the measured XMCD signal strongly supports our ARPES results in that it confirms that the Ce in the subsurface area of $CeCo_2P_2$ strongly deviates from the non-magnetic, tetravalent bulk behavior. A direct valence determination from the shape of the X-ray absorption spectra is not easily achievable due to final state effects. The X-ray absorption core-hole potential can strongly influence the spectral weights when the Ce $4f^0$ and $4f^1$ configurations are very close in energy [125–128].

Additionally to the XMCD spectra of the Ce $M_{4,5}$ absorption edge shown in Figure 4.20, measurements in the same geometry were also performed for Co $L_{2,3}$ edge with an applied magnetic field of $B = 9\,\mathrm{T}$ along the incidence direction. Comparing XMCD signals for grazing ($\theta = 65°$) and normal ($\theta = 0°$) incidence as shown in Figure 4.21, no significant changes in either the intensity or shape

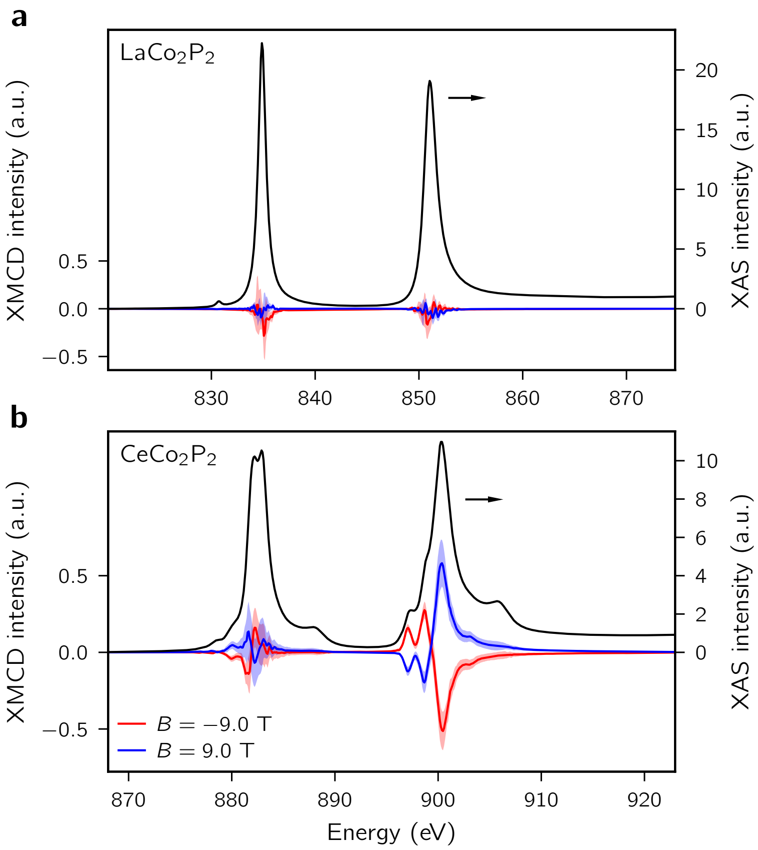

Figure 4.20: X-ray absorption and XMCD spectra of $LaCo_2P_2$ and $CeCo_2P_2$ taken at $T = 5\,K$ and $B = 9\,T$. The right axis shows the X-ray absorption intensity (black) measured in total electron yield. The left axis shows the corresponding XMCD intensities plotted in blue and red. The lightly shaded areas around the XMCD signals indicate the uncertainty intervals determined by the standard deviations of the mean X-ray absorption spectra of multiple scans.

can be observed. However, this is in contrast to the expected anisotropic behavior of an antiferromagnetic Co sublattice oriented along the *c* direction. Instead, the observed isotropic behavior of the Co moments in the XMCD measurements suggests the existence of an uncompensated Co layer which magnetic moments can be easily rotated. The same behavior can be found when examining the Ce XMCD signal which stays unchanged in both geometries, too. Thus, the measured XMCD signals are in line with the interpretation of an uncompensated subsurface Co layer and show the same behavior for the Co and Ce sublattices supporting a coupling between the two subsurface layers.

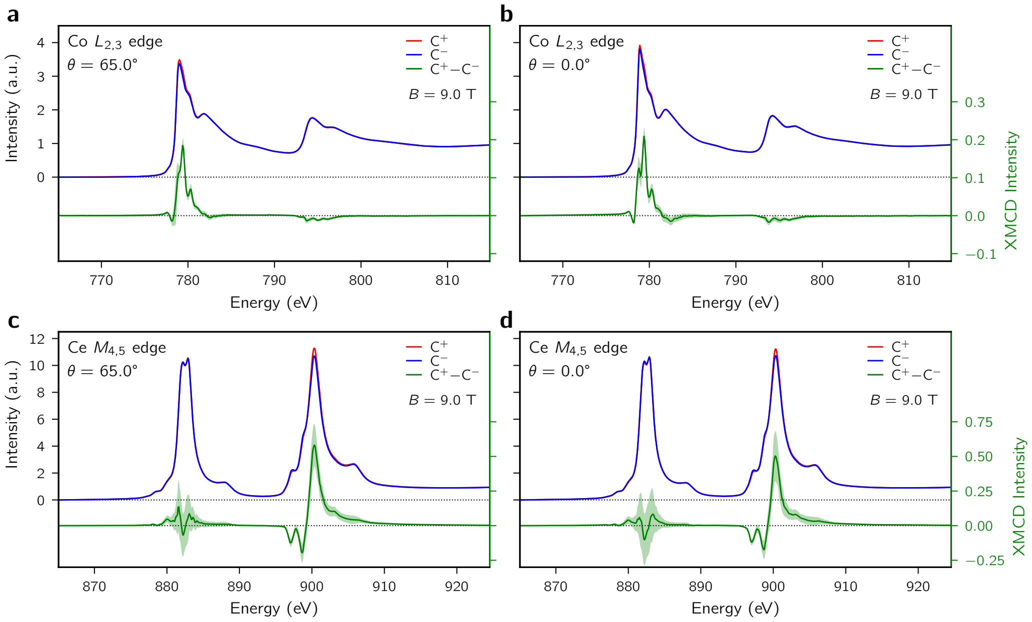

Figure 4.21: X-ray absorption spectroscopy and corresponding XMCD spectra of $CeCo_2P_2$ taken at $T = 5\,K$ for the (a, b) Co $L_{2,3}$ and (c, d) Ce $M_{4,5}$ edge in the total electron yield measured with an applied magnetic field $B = 9\,T$ oriented along the incidence beam. The absorption spectra with opposite circular light polarizations are shown in the upper part (intensity axis on the left) while the corresponding XMCD signal is shown directly below in green (intensity axis on the right). The lightly shaded area around the dichroism signal represents the combined standard deviation of the two spectra with opposite light polarization which are the mean of multiple individual absorption scans.

4.3.5 Possible origin of subsurface Kondo lattice

To understand the obtained experimental findings, we performed ab-initio electronic and magnetic structure calculations for the bulk and surfaces of $CeCo_2P_2$ using a first-principles pseudopotential approach [129] and a multiple scattering Green function method, designed for bulk, surface and interfaces [130]. To describe the strongly correlated Co 3d states, the GGA+U approach was used and the value of the Hubbard U parameter was chosen to provide a good agreement in magnetic properties with experiments for bulk $CeCo_2P_2$. Thus, for $U = 3\,eV$ the calculated magnetic order was found to be layerwise AFM and the derived Néel temperature ($T_N^{calc} = 400\,K$) agrees well with experimental value ($T_N^{exp} = 440\,K$).

First, starting with the bulk properties, the calculated electronic structure of the bulk of $CeCo_2P_2$ shows that the spectrum near the Fermi level is mostly composed of Co 3d and Ce 4f orbitals. Looking at the density of states (DOS) of the bulk as shown in Figure 4.22(a), we can see that the Co 3d orbitals are spread out in a wide energy range from -6 to $2\,eV$, while the Ce 4f orbitals are mostly located in the unoccupied part of the spectrum with a small tail in the valence

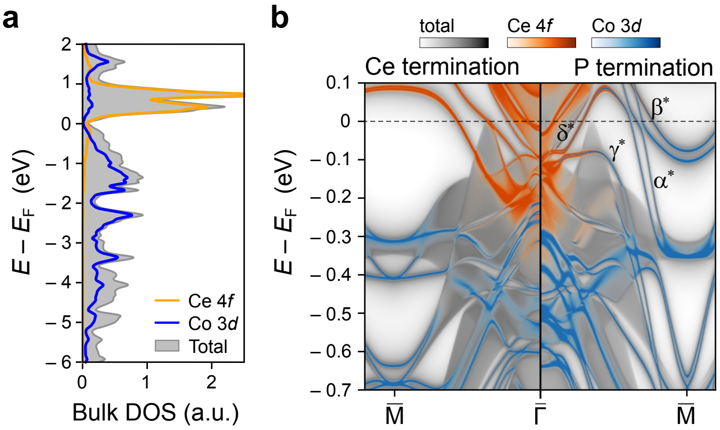

Figure 4.22: (a) Total density of states (DOS) in gray with partial Ce 4f DOS in orange and Co 3d DOS in blue shown for the bulk of $CeCo_2P_2$. (b) Comparison of the electronic structures for both Ce- and P-terminated surfaces of $CeCo_2P_2$. The total spectral density is shown in gray-scale and the spectral contributions of the uppermost Co and Ce atoms in blue and orange intensities, respectively.

band region occupying an energy window down to 1 eV below E_F. Thus, Ce was found to be close to tetravalent in the $CeCo_2P_2$ bulk in good agreement with experiment. Importantly, the $f-d$ hybridization is induced by the states located near the Fermi level, where the DOS forms a minimum. Looking at the magnetic moments, our calculations show that in the bulk, the Ce atoms are non-magnetic and the Co magnetic moments are of 1.06 μ_B.

Next, we calculated the electronic structure of the $CeCo_2P_2$(001) surface for both P- and Ce-terminated surfaces. In both cases, the Ce atoms near the surface possess a non-zero magnetic moment. For the Ce-terminated surface, the Ce magnetic moments on the surface ($\mu_{Ce} = 0.82\,\mu_B$) are antiparallel to the nearest Co moments, which are slightly smaller than in the bulk. At the surface, the Ce atoms lose electronic bonds and, therefore, the Ce electronic states hybridize less with the states of other atoms in the environment. Hence, due to symmetry and bond reduction at the surface, the Ce 4f states are getting more localized and partially occupied with Ce becoming trivalent. However, the subsurface Ce atoms remain nonmagnetic and behave bulk-like.

More interesting for the comparison with our APRES measurements is the P-terminated surface. In spite that the first Ce layer is buried by the P-Co-P surface block, the Ce atoms are magnetic with $\mu_{Ce} = 0.18\,\mu_B$ and couple ferromagnetically to the subsurface Co moments, which are substantially smaller than in the bulk ($\mu_{Co} = 0.45\,\mu_B$). The Ce magnetic moments are induced by a nonzero magnetic field, which arises due to the uncompensated Co magnetic moments in the P-Co-P surface block. Using the disordered local moment (DLM) approach, we investigated the behavior of the Ce magnetic moments with temperature and found that they vanish with increasing temperature, which indicates their induced nature.

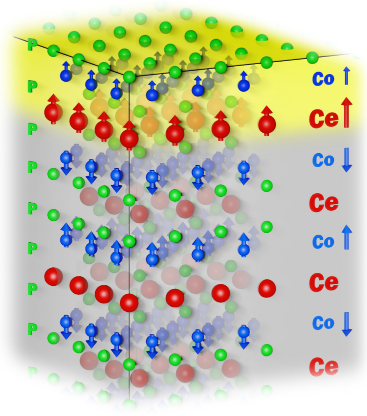

Figure 4.23: Schematic of the crystal and magnetic structure of the P-terminated surface of $CeCo_2P_2$. The direction of the magnetic moments is shown by arrows. The size of the Co and Ce arrows corresponding to the magnetic moments is not in the same scale. The surface area is highlighted in yellow.

A schematic view of this surface is given in Figure 4.23 highlighting the single subsurface Ce layer with magnetic moments.

A direct comparison of the band structure of the P- and Ce-terminated surface of $CeCo_2P_2$ is shown in Figure 4.22(b) along the $\overline{\mathrm{M}}$–$\overline{\Gamma}$–$\overline{\mathrm{M}}$ high-symmetry direction. We can see that the metallic character of the bulk spectrum is provided by states located in the vicinity of the $\overline{\Gamma}$-point of the surface Brillouin zone shown in gray. The surface metallicity is guaranteed by the discrete features near the $\overline{\mathrm{M}}$-point, in the area of the local bulk band gap with a width of 0.5 eV. The presented spectra contain a variety of surface features with their nature not only depending strongly on the surface termination but also on their energy and momentum scales.

Around the $\overline{\mathrm{M}}$-point in the bulk band gap, two pairs of split surface states with parabolic dispersion can be seen for the P-terminated surface while no such states exist for the Ce-terminated surface. These states labeled α^* and β^* correspond well with the α and β bands observed in ARPES proving that our measurements were performed on a P-terminated surface. Additionally, a good agreement is also found between the experimentally observed γ band and the γ^* band, while the strongly hybridized δ feature around the $\overline{\Gamma}$ point seems to be also reproduced by the area around δ^* which shows strong $4f$ contribution.

Looking in detail at the surfaces states around the $\overline{\mathrm{M}}$ point as shown in Figure 4.24, the calculated surface states α^* and β^* reveal an additional splitting which was not resolved in ARPES. For the upper surface state β^* close to E_{F}, this splitting is well separated over the momentum range and the bands are composed of both Co-3d ($d_{z^2-r^2}$, d_{xy}) and Ce-4f ($f_{5xz^2-xr^2}$, $f_{5yz^2-yr^2}$) orbitals, within four layers near the vacuum boundary. At the $\overline{\mathrm{M}}$-point, the splitting of the bands is induced by spin-orbit coupling (SOC), which has been proven by our additional calculations without SOC shown in Figure 4.24(c) where no splitting in the $\overline{\mathrm{M}}$-point is observed. Away from the $\overline{\mathrm{M}}$-point, the splitting of these two bands is caused by the crystal electric field. The difference between the split bands can be disentangled by considering the spectral contribution of Co-3d ($d_{xy} \pm d_{z^2-r^2}$) hybrids closest to the vacuum boundary (see corresponding spectrum in Fig-

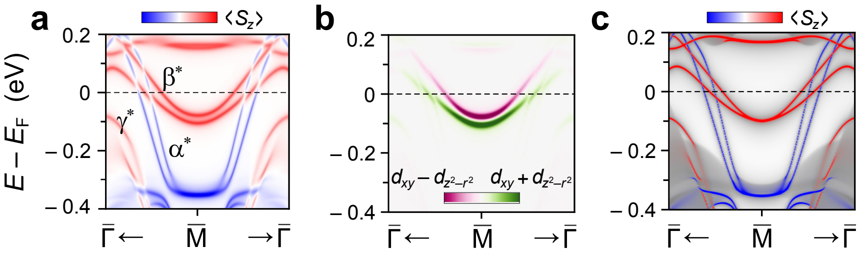

Figure 4.24: (a) Out-of-plane component of the spin-resolved spectral density $\langle S_z \rangle$ of the P-terminated surface around the $\overline{\mathrm{M}}$ point in red (blue) color representing positive (negative) sign of $\langle S_z \rangle$, and (b) the orbital composition where the Co $3d_{xy} - d_{z^2-r^2}$ and $d_{xy} + d_{z^2-r^2}$ character are shown by burgundy and green colors, respectively. (c) The same spin-resolved spectral structure as in (a) but calculated without spin-orbit interaction. The projected bulk bands are shown in gray-scale.

ure 4.24(b)). This demonstrates that the split bands are distinguishable by these hybrid orbital contributions, which in turn confirms their crystal field splitting. The discussed surface features have an out-of-plane spin-momentum direction which is related to the magnetization of the Ce layer closest to the vacuum and can be seen in Figure 4.24(a).

While the above described pair resides closely around E_F, the surface state α^* has a stronger dispersion and extends over a much larger energy range. In the small vicinity around the $\overline{\mathrm{M}}$-point at an energy of ~ 0.35 eV below E_F, the pair has the character of a surface resonance with a sizable contribution stemming from the second Co layer below the surface and without any contributions from Ce atoms. Along the $\overline{\Gamma} - \overline{\mathrm{M}}$ direction and close to E_F, α^* starts to hybridize with the β^* bands forming an avoided crossing induced by the spin-orbit interaction implying their similar nature. This becomes especially apparent when looking at the out-of-plane spin momentum shown in Figure 4.24(a) with both pairs exhibiting an opposite spin polarization induced by the exchange interaction of the Co layer.

Lastly, focusing on the area around the $\overline{\Gamma}$-point in Figure 4.22(b), both surface and bulk states can be seen. When going from the bulk to the surface, the contributions from the Ce-4f orbitals increase. The surface states are no longer strongly localized at the surface but the charge density of these states extends into deeper layers and decays only weakly. Hence, these states can be understood as surface resonances which couple to the Ce-4f states situated at the surface.

4.3.6 Summary and outlook

Investigating the electronic structure and magnetic properties of the Co-based antiferromagnetic material $\mathrm{CeCo_2P_2}$, we found that in the bulk this system does not exhibit any significant 4f-driven properties. Instead the Ce-4f sublattice is passive and behaves tetravalently. At the P-terminated surface, however, the symmetry breaking leads to an uncompensated ferromagnetic Co layer resulting in an effective magnetic field within the P-Co-P-Ce surface block, which in turn causes the Ce-$4f$ states to become partially occupied and spin-polarized. With the appearance of a magnetically active Ce $4f$ state, a clear and weakly-dispersive $4f^1$ emission at E_F can be seen in the ARPES data. The temperature-dependent ARPES measurements reveal a clear Kondo lattice behavior for the P-Co-P-Ce surface.

Further, our calculations show that the Ce-$4f$ moments experience a ferromagnetic coupling with the single FM-ordered Co layer within the P-Co-P-Ce surface block. Our findings demonstrate how rich and diverse f-driven properties can exist at the surface of materials without f properties in the bulk. Based on our obtained results, we propose $CeCo_2P_2$ as an ideal model system where the interlayer coupling between a 2D Kondo lattice and a ferromagnetic layer can be investigated in detail. We anticipate that similar or more advanced 2D magnetic properties can exist at surfaces of many strongly correlated systems possessing a layered quasi-2D structure and containing f and d elements.

5 Spin excitations in $CeCo_2P_2$

This chapter presents the results of our RIXS study on $CeCo_2P_2$. The corresponding manuscript G. Poelchen et al. Undamped spin waves in an itinerant antiferromagnet *is currently in preparation.*

The samples were provided by the group of C. Krellner. K. Kummer and I performed the RIXS measurements. I performed initial DFT and linear spin wave theory calculations based on exchange parameters provided by A. Ernst. However, for a consistent theoretical treatment all calculations presented in the following were performed by A. Ernst.

5.1 Introduction

Based on the ARPES study presented in Section 4.3, the first principle calculation predicted a reduced density of states at E_F. This, as well as the missing the contribution of the Ce $4f$ makes the study of the magnetic bulk properties interesting. From previous bulk measurements, it was found that the Co moments have a stacked AFM order along the c axis with each layer being ferromagnetically (FM) ordered along c below $T_N \approx 440\,K$ [111]. Not only is the ordering temperature extraordinarily high in comparison to similar systems with large Co moments of $0.94\,\mu_B$, but this makes this material interesting also as basis for practical applications.

One very promising field of study for new quantum devices is the field of magnonics which is focused on the usage of spin waves to transport a spin current [131–134]. This spin flow requires no electrical charge transport and therefore no electrical losses creating Joule heating. Spin waves enclose a wide frequency range, from gigahertz up to a few hundreds of terahertz [135]. The larger the excitation frequency, the faster are the magnon processes. However, the utilization of magnons in magnonic applications can be limited by their lifetime, which can range from a few tenths of a microsecond down to tens of femtoseconds, depending on their frequency and some features of the electronic structure [136]. Low-frequency (GHz) magnons usually posses longer lifetimes than THz magnons and are therefore currently considered as the most promising for magnonic applications [133, 137, 138]. But one of the exciting prospects of magnonics is clearly the potential to eventually be able to design ultrafast magnonic devices pushing far into the THz regime [139]. To this end, materials with high ordering temperatures and high magnon energies, and at the same time long magnon lifetimes, i.e. weak magnon damping, are required.

In general, magnon lifetimes can be affected by various scattering processes such as electron-magnon, phonon-magnon, magnon-magnon interactions, spin-orbit damping or impurity scattering [139, 140]. In metals, the most significant one is the electron-magnon interaction, meaning the interaction between magnons and the Stoner continuum, which represents single-particle excitations in the same energy range as the magnons [141–144]. However, since Stoner spin flip excitations are governed by transitions between occupied and unoccupied bands with different spins, large Stoner gaps can strongly increase the energy needed for such excitations.

In Figure 5.1, the connection between the size of the spin gap and the onset spin wave damping is schematically presented. For a small spin gap, the Stoner continuum is at very low energies and thus a spin wave gets damped at low energies when interacting with the Stoner continuum. If the Stoner gap is increased, the Stoner continuum shifts up in energy and the spin waves damping is strongly reduced for low energy excitations leading to long lifetimes of the spin waves. Thus, the occupied and unoccupied electronic states which participate in Stoner excitations between the two spin channels should be separated by a Stoner gap or pseudogap that is larger than the energy range of the spin wave excitations.

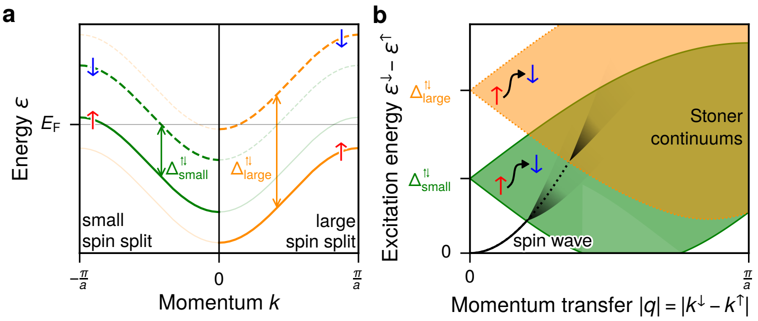

Figure 5.1: Correlation between (a) the size of the spin (Stoner) gap and (b) the onset of spin wave scattering in magnetic metals. Larger spin gaps promote undamped spin waves up to higher energies.

In this regard, $CeCo_2P_2$ seems to be a promising candidate for undamped magnons up to the THz regime because it has a large magnetic moment and high ordering temperature suggesting a strong exchange coupling of the Co moments resulting in large spin excitations as discussed in form of the Heisenberg Hamiltonian in Section 2.5. The predicted reduced density of states and thus a large spin gap would result in a weak electron-magnon interaction and thus long lifetimes of the spin excitations.

Besides our calculations, a recent theoretical study proposed $CeCo_2P_2$ to be an enforced semi-metal with topological properties [145]. While from the transport properties, $CeCo_2P_2$ behaves like a good metal, this calculation is still in agreement with a reduced density of states at E_F.

To test our predictive power, we chose for comparison the isostructural $LaCo_2P_2$, which differs from $CeCo_2P_2$ by only one electron, but both the structural as well as the magnetic properties differ strongly. As a result of the the lanthanide contraction going from La to Ce, the c lattice constant is much larger for $LaCo_2P_2$ leading to a larger d_{P-P} shown in Figure 5.2. Hence, $LaCo_2P_2$ can be understood as being in an uncollapsed phase with weaker interlayer couplings and a more two-dimensional character. This becomes apparent in the different magnetic order with the Co moments ordering ferromagnetically in the ab plane. Both the ordering temperature $T_C \approx 135\,\mathrm{K}$ and the Co moments $\mu_{Co} \approx 0.45\,\mu_B$ are significantly lower than in $CeCo_2P_2$ [146–148]. In addition, de Haas-van Alphen measurements [149] as well as the large Sommerfeld coefficient discussed in Section 4.3.1 indicate a large DOS at E_F. We would therefore expect a much weaker magnon dispersion and strong electron-magnon damping.

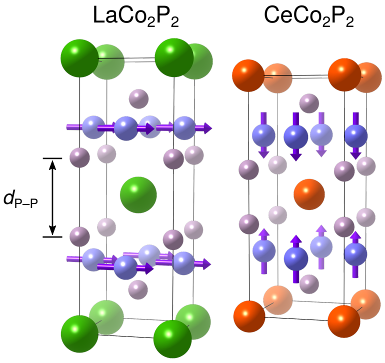

Figure 5.2: Crystal structures of $LaCo_2P_2$ and $CeCo_2P_2$ showing the reduced P-P distance and smaller cell volume leading to a larger magnetic exchange between Co layers in $CeCo_2P_2$. $LaCo_2P_2$ is in the uncollapsed structural phase where the P atoms are not able to form a bonding orbital. Under pressure of 6 GPa, $LaCo_2P_2$ has a first-order phase transition into the collapsed phase with the lattice constants being similar to the one of $CeCo_2P_2$ [150].

5.2 Results

5.2.1 Measurement of magnons

A direct way to confirm our expectations is to use RIXS at the Co L_3 edge to directly measure the spin excitations and their damping over a large q and energy $\hbar\omega_q$ interval. In Figure 5.3a, the geometry of the RIXS process is presented. Incoming light $\vec{k}_{\text{in}}$ under the incidence angle θ is scattered of the sample $\vec{k}_{\text{out}}$ under the scattering angle $2\theta'$ resulting in a momentum transfer $\vec{q} = \vec{k}_{\text{in}} - \vec{k}_{\text{out}}$. Tuning the incoming photon energy to the Co L_3 absorption edge allows for the element specific enhancement while changing the scattering geometry allows measuring the elementary excitations in the sample as a function of momentum transfers $\vec{q}$. The RIXS process is schematically shown in Figure 5.3b and describes the absorption of an photon $\hbar\omega_{\text{in}}$ leading to an intermediate state with a $2p$ core hole which then decays raditively into the final state emitting a photon with energy $\hbar\omega_{\text{out}}$. The process is discussed in more detail in Section 3.4. The final state can be different then the initial state leaving the system for instance with a collective excitation like a magnon.

In Figure 5.3(c), we show for $CeCo_2P_2$ the experimentally observed RIXS intensity as a function of energy loss $\hbar\omega_{\text{in}} - \hbar\omega_{\text{out}}$ at fixed $\vec{q} = (-0.12, 0, 1)$. The

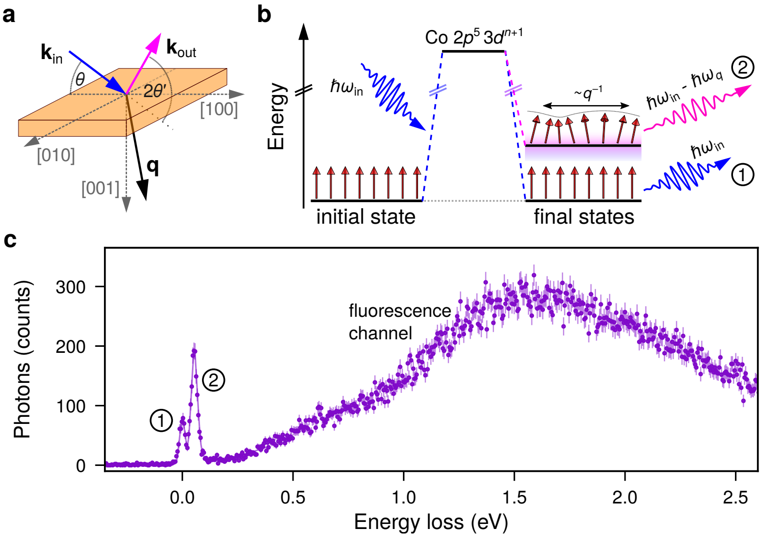

Figure 5.3: RIXS measurements of the magnon excitations in CeCo$_2$P$_2$. (a) Experimental geometry. (b) Schematic of the RIXS process, showing elastic scattering associated with no energy loss and magnon excitations at finite energy loss. (c) Experimentally observed RIXS spectra.

measured spectrum is dominated by two features, a double peak structure around zero energy loss and a broad peak around 1 eV to 3 eV. Slightly tuning the incident photon energy, the peaks in the low energy region will remain at the same position as expected for Raman-like quasi-particle excitations. By contrast, the broad feature centered around 1.5 eV will move on the energy loss axis with incident photon energies which identifies it as stemming from fluorescence decay of the core hole. This very intense fluorescence feature due to local, intraatomic decay of the RIXS intermediate state is a characteristic of RIXS spectra taken from metallic systems with very high electron mobility [151–153]. The RIXS measurements were performed at the ID32 beamline of the ESRF [73]. The samples were freshly cleaved before the measurements and then cooled down to 20 K.

In the following, we will concentrate on the low energy region of the RIXS spectra shown in Figure 5.4(a) with the quasi-elastic peak at zero energy loss and an additional peak which varies in energy position as a function of $\vec{q}$ and can be attributed to magnon excitations. The dispersion along the $(H\,0\,1)$ direction with H going from -0.24 to 0.2 in reciprocal lattice units (r.l.u.), i.e. the full H range accessible to Co L_3 edge RIXS in this compound, is shown in Figure 5.4(b). The dispersion seems to follow a linear relation as expected for antiferromagnets (see Section 2.5). Due to the magnetic Bragg condition, measurements close to $\vec{q} = (0, 0, 1)$ are dominated by the elastic peak and omitted here.

In order to determine both the energy position $\hbar\omega_q$ and the damping of the magnetic excitations, we fitted the spectra using a model with two peaks, an elastic peak and a magnon peak, and a background function as shown in Figure 5.3(c).

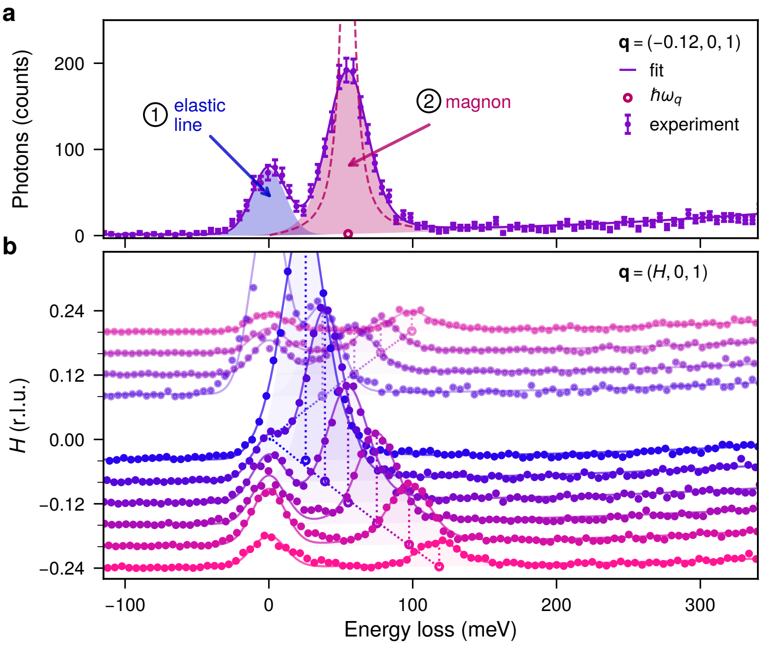

Figure 5.4: (a) RIXS spectrum zoomed into the low energy region decomposed into the quasielastic line around zero energy loss (1) and a sharp loss feature due to magnon excitations (2). (b) q dependence of the RIXS spectra along (H 0 1).

The elastic line is described by a single line at zero energy loss, while the magnon peak is generally described by function based on the damped harmonic oscillator

$$I(E_{\text{loss}} > 0, \hbar\omega_q, \gamma) = I_0(\hbar\omega_q) \frac{\gamma E_{\text{loss}}}{\left(E_{\text{loss}}^2 - \hbar^2\omega_q^2\right)^2 + 4\gamma^2 E_{\text{loss}}^2} \tag{5.1}$$

with a damping factor γ [154–156]. Both peaks are convolved with a Gaussian with FWHM $\Delta E = 28\,\text{meV}$ to account for the experimental resolution in our experiment. This two peak model gives an excellent description of the experimental data. Some small residual intensity can be seen for larger H values around 30 meV to 40 meV, which corresponds to the typical excitation energies of phonons in this class of systems [157]. Since these contributions are very small, their influence will be neglected.

In the same way as for $CeCo_2P_2$, the RIXS spectra were also measured for $LaCo_2P_2$ which also show an elastic line and an additional energy loss shoulder which can be attributed to the magnon excitation. In contrast to $CeCo_2P_2$ however, this shoulder does not separate for higher q into an isolated peak, making the determination of the $\hbar\omega_q(q)$ dispersion difficult. Instead, we will directly compare the $CeCo_2P_2$ and $LaCo_2P_2$ in Figure 5.8.

5.2.2 Density of states, exchange interactions and magnon dispersions

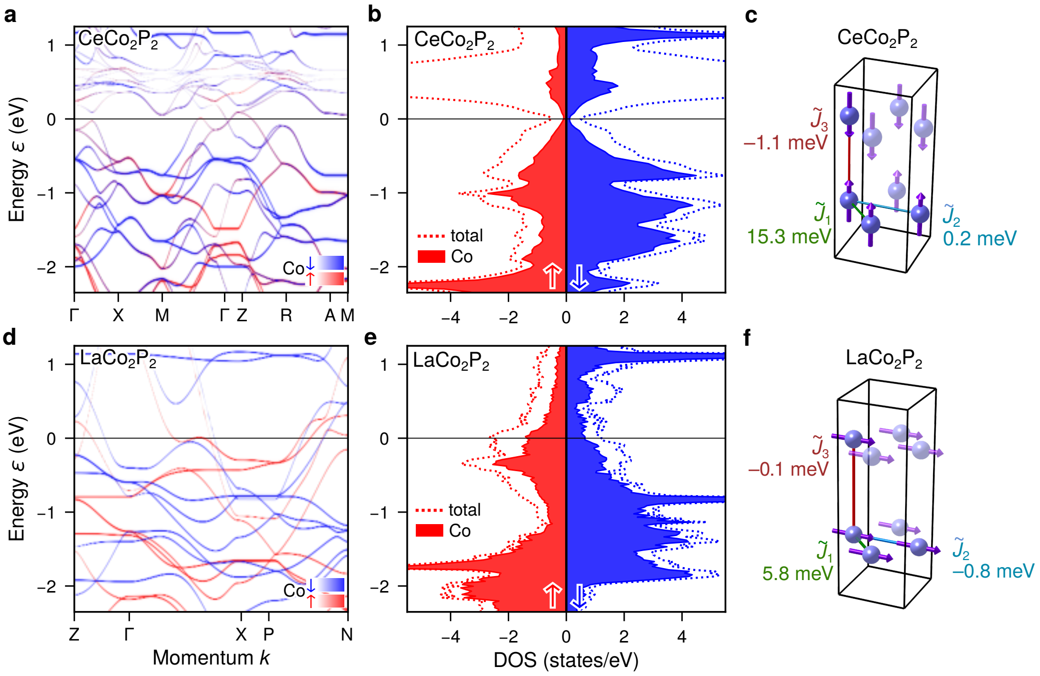

Figure 5.5: (a, d) Spin-resolved band structure and (b, e) density of states of $CeCo_2P_2$ and $LaCo_2P_2$, respectively. The total density of states for both spin channels is shown as dashed lines while the Co contribution is shown as filled area. (c, f) shows the first three normalized exchange constants for $CeCo_2P_2$ and $LaCo_2P_2$.

Having determined the magnon dispersion experimentally, we now want to compare the measurements to the calculations. The electronic structure calculations were performed using a first-principles Green function method [130] within the density functional theory in a generalized gradient approximation [158]. Localized Co 3*d* states were treated with a GGA+U approximation to take into account strong electronic correlations [159, 160]. The effective $U^* = U - J$ value of 3 eV was found to be the best choice to provide a good agreement between experiment and theory for the ordering temperature and magnon frequencies. First, we take a detailed look at the band structure and density of states shown in Figure 5.5. For $CeCo_2P_2$, a few bands can be seen crossing E_F, however, their Co 3*d* contribution is small. Below -0.5 eV, a large number of bands with strong Co contribution can observed while above E_F, flat bands stemming from the Ce 4*f* states are visible. Looking at the density of states, it becomes apparent that in both spin channels, the density of states around E_F is small but still significantly larger than zero. However, the Co 3*d* states, which are responsible for the magnetism, are effectively zero at E_F leading to a gap in both spin channels. On the other hand, $LaCo_2P_2$ exhibits a number of bands crossing E_F with a significant

Co $3d$ contribution. This can be also seen in the density of states at E_F, which is not only large for the majority spin channel but also considerably for the minority channel. These calculations give the basis for a weak electron-magnon interaction in $\mathrm{CeCo_2P_2}$ and a typical metallic electron-magnon interaction in $\mathrm{LaCo_2P_2}$.

In order to describe the magnetic excitations in $\mathrm{CeCo_2P_2}$ theoretically, we determined the exchange coupling constants J by applying the magnetic force theorem as it is implemented within a first-principles multiple scattering theory [130, 161]. In Figure 5.5(c,f), the first three exchange constants $\tilde{J}_i$ are shown ($\tilde{J}_i$ is J_i normalized by the magnetic moment of Co). As can be seen for $\mathrm{CeCo_2P_2}$, a strong intralayer coupling leads to a ferromagnetic coupling in the *ab* plane while the negative interlayer coupling $\tilde{J}_3$ leads to an AFM coupling between neighboring Co layers, in agreement with what is observed experimentally. For $\mathrm{LaCo_2P_2}$, the coupling constants are reduced, especially the interlayer coupling $\tilde{J}_3$ which is close to zero. This theoretical description is in accordance with the ferromagnetic ordering determined experimentally in $\mathrm{LaCo_2P_2}$.

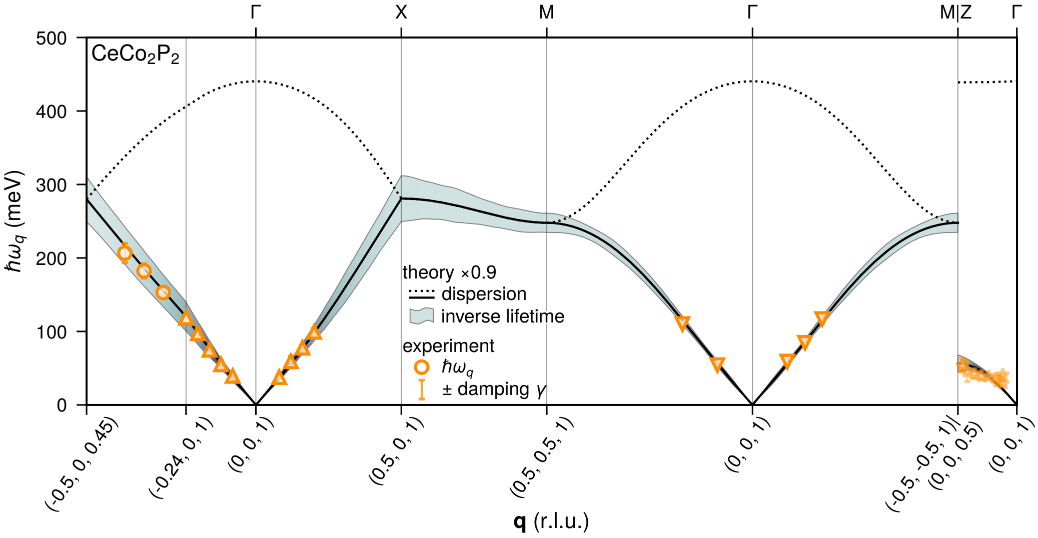

Figure 5.6: Calculated and experimentally observed magnon dispersion and lifetimes in $\mathrm{CeCo_2P_2}$. Dashed lines show backfolded magnon branches with vanishing RIXS cross section. The magnon dispersion and inverse lifetimes are scaled by a factor of 0.9 to coincide with the experimentally determined values.

Using linear spin wave theory, the magnon dispersion for $\mathrm{CeCo_2P_2}$ was calculated and compared to the experimentally determined magnon excitation energies $\hbar\omega_q$ as shown in Figure 5.6. We find good overall agreement between experiment and theory with a linear dispersion $\omega_q \propto q$ for $q_\parallel \to 0$ as expected for AFM order [162]. Along the $(H\,0\,1)$ and $(H\,H\,1)$ directions the spin wave energies extend beyond 400 meV, i.e well into the THz regime. We note that while the shape of the dispersions compares nicely, the calculations slightly overestimated the spin wave energies. Applying a constrained fit with a scaled theoretical dispersion showed that the best agreement with the experiment is achieved when rescaling the theoretical dispersion by a factor of 0.9. The slight disagreement between experiment and theory can be attributed to strong electronic correlation effects, which can not be fully taken into account in DFT+U(Co) calculations. However, the overall agreement with the experimental results is excellent.

As discussed before, for the experimental determination of the magnon dispersion in $LaCo_2P_2$ was not possible due to the low signal and hard to resolve magnon peak. So Figure 5.7 only shows the theoretically determined magnon dispersion. As expected, the magnon dispersion is much weaker than for $CeCo_2P_2$ only barely reaching above 200 meV.

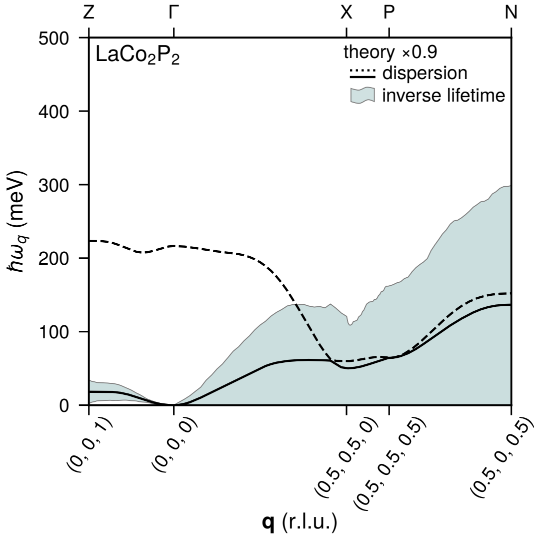

Figure 5.7: Calculated magnon dispersion scaled by a factor of 0.9. The inverse lifetime is shown as interval around the lower magnon branch. The upper branch is the backfolded magnon branch into the crystal unit cell. Around (0, 0, 0), the quadratic q behavior expected for ferromagnetic ordering is visible.

5.2.3 Electron-magnon interaction and damping

Besides the magnon dispersion, the RIXS measurements make it possible to determine the damping factor γ which we introduced in Equation (5.1). Included in Figure 5.6 are the damping factors for all measured q points. For all q, $\gamma \ll \hbar\omega_q$ and thus the damping is minimal with the magnon being in the undamped regime. In this case, the shape of the experimentally observed magnon is peak is nearly fully symmetric and its width determined primarily by the experimental resolution ($\gamma < \sigma_{\mathrm{res}}$). This becomes especially apparent in Figure 5.4 where all magnon peaks up to energies above 100 meV look symmetric and have approximately the same shape and width as the elastic peak. The experimental results are in a good agreement with lifetimes calculated within a first-principles linear response theory for the magnetic susceptibility [163, 164]. We can see that in the calculations notable damping with $\gamma \geq 12$ meV, sets in only for very high magnon energies above 200 meV. In order to confirm these theoretical results, we also acquired RIXS spectra away from the $(H\,0\,1)$ high symmetry direction by fixing the scattering angle to the maximum possible 150° and moving along the path

$\vec{q} = (-0.24,\, 0,\, 1) \rightarrow (-0.5,\, 0,\, 0.45)$ in r.l.u.. This allows for a high enough in-plane momentum transfer able to probe the spin wave excitations up to 200 meV and above, where, in agreement with theory, notable damping can be observed. But even there, it is important to note that the lifetimes are still large in comparison with other metallic magnetic materials, which show a strong damping as a result of scattering of the magnons on the electron-hole continuum [143, 163].

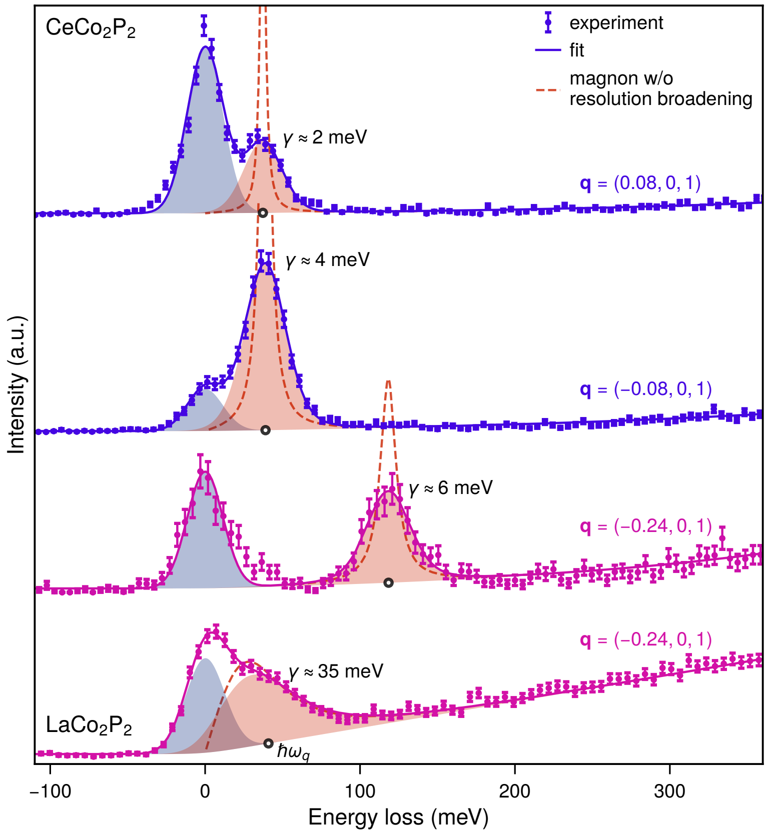

Figure 5.8: Comparison of the $CeCo_2P_2$ and $LaCo_2P_2$ RIXS spectra showing sharp, resolution limited peak shapes in $CeCo_2P_2$ as compared to a broad magnon peak for $LaCo_2P_2$. The magnon dispersion is considerable smaller in $LaCo_2P_2$ in agreement with our calculations.

In Figure 5.8, a direct comparison of the RIXS spectra for $CeCo_2P_2$ and $LaCo_2P_2$ for similar magnon excitation energies and for the same $\vec{q}$ point are shown. Comparing first the $CeCo_2P_2$ spectra measured at $\vec{q} = (\pm 0.08, 0, 1)$ with the $LaCo_2P_2$ spectra at $\vec{q} = (-0.24, 0, 1)$, where the magnon excitations have the same energy of about $\hbar\omega_q = 34\,\text{meV}$, the difference is striking. In $CeCo_2P_2$ the magnon excitations appear as a well separated, symmetric peak with resolution-limited width. In $LaCo_2P_2$, by contrast, the magnon excitations give rise to a broad asymmetric peak merging with the quasielastic line with a width primarily defined by the lifetime (damping) of the magnons. Comparing the same $\vec{q} = (-0.24, 0, 1)$, the difference in the magnon dispersion is clearly visible. For $CeCo_2P_2$, the magnon excitation energy is around 120 meV and thus nearly three times larger than for $LaCo_2P_2$. Note however, that the same q point does not correspond to the same symmetry in $LaCo_2P_2$ and $CeCo_2P_2$ due to the AFM order which increases the size of the primitive cell as discussed in Section 2.5.

Finally, the lifetimes with respect to the excitation energies of $CeCo_2P_2$ are presented in Figure 5.9. For comparison we also added our results for $LaCo_2P_2$ as well as magnon damping reported in the literature for other itinerant magnets [144, 153, 165]. The properties of $CeCo_2P_2$ with its high-energy, long-lifetime magnons and at the same time good metal behavior stand out in this comparison.

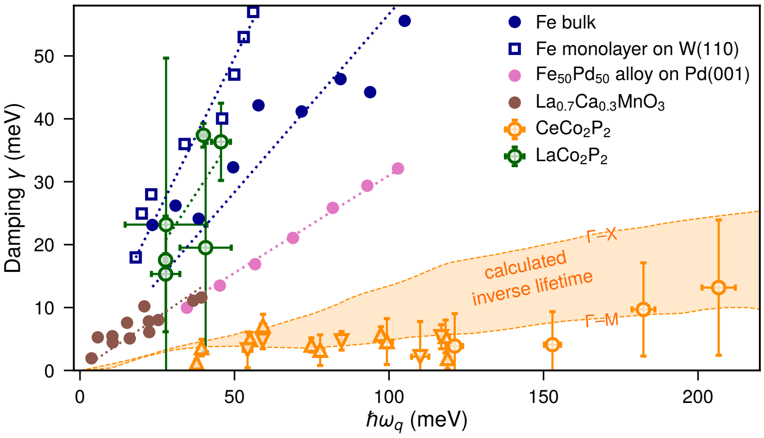

Figure 5.9: Experimental and calculated lifetime broadening of the magnetic excitations in $CeCo_2P_2$ compared to data reported for other itinerant magnets [144, 153, 165].

5.3 Summary and outlook

We have identified a metallic magnet with long-lived magnons up to the THz regime and an ordering temperature well above room temperature. This is in stark contrast to the generally very short life times of high-energy magnons in metals. Based on our magnon lifetime calculations, these long-lived excitations are a result of a weak electron-magnon interaction due to a reduced DOS around E_F. Indeed, for $LaCo_2P_2$ with a large DOS at E_F we observed strongly damped magnetic excitations already well below 100 meV, which is the typical response of magnetic metals. Our results show that long-lived magnons in the THz range can exist in metallic AFM systems. In combination with its large $T_N = 440\,K$ this makes $CeCo_2P_2$ a potentially very interesting material for metallic magnonic devices whose potential should be further explored. The tunability of $CeCo_2P_2$ by doping with La opens up different magnetic phases with competing ferromagnetic and antiferromagnetic order. A reduction of the Ce concentration also leads to an increase of the cell volume which could be connected to a change of the Ce

$4f$ physics becoming more localized.

Additionally, the magnon damping of $LaCo_2P_2$ under pressure is still an open question. After the transition to the collapsed phase, $LaCo_2P_2$ has similar lattice parameters to the one of $CeCo_2P_2$. Expected with the collapse is a change in the electronic structure due to the strong overlap of the P p_z orbitals. On the other hand, the extra electron of the Ce seems to be influential for the formation of the reduced density of states at E_F. In this regard, the Ce(La)Co_2P_2 system still contains fascinating properties that have to be explored further.

6 Summary and outlook

In this work, two members of the CeT_2X_2 family have been studied by means of ARPES, X-ray absorption spectroscopy and RIXS. This family of Ce-based intermetallics makes it possible to study Ce $4f$ properties ranging from magnetic Ce sublattices over quantum criticality and heavy-fermion Kondo lattices combined with superconductivity up to strong intermediate or tetravalent behavior. Thus, in the Doniach picture, this family effectively covers the whole phase diagram. The two members we chose are $CeRh_2Si_2$ and $CeCo_2P_2$. Both compounds differ significantly in their $4f$ physics with $CeRh_2Si_2$ clearly showing the dual nature of the $4f$ electrons with an antiferromagnetic order of the $4f$ moments and at the same time a Kondo temperature in the same order of magnitude. On the other $CeCo_2P_2$ shows no $4f$ physics and instead the Co sublattice orders at an extraordinary high temperature due to the unique structure linked with the reduced volume of the Ce.

Starting with $CeRh_2Si_2$, the work presented here is a continuation of the previous ARPES studies which determined that two different surface terminations of $CeRh_2Si_2$ exist which show the characteristic $4f$ response of weakly hybridized, γ-like Ce for the Ce-terminated surface or a stronger hybridization with α-like character for the Si-terminated surface. Our ARPES study in combination with DFT calculations revealed that both the temperature dependence and the band-dependent hybridization differs between the two terminations. Analyzing the temperature dependences uncovered a higher characteristic temperature for the Ce-terminated surface than for the Si-terminated surface. This surprising behavior can be reconciled by the fact that a strongly reduced crystal-electric field splitting at the surface Ce increases the effective $4f$ degeneracy and thus could lead to a larger Kondo temperature. By modeling the measured spectra, the interaction of the $4f$ states with different valence bands was explored. Using first principle calculations and a two- or three-band model, the $4f$ contribution above the E_F could be followed which differed strongly between the two different terminations due to the different electronic structure around the $\overline{\Gamma}$ point. Based on these conclusions, our measurements highlight the importance of taking surface terminations and surface effects into account when not only studying Ce-based compounds but for general surface sensitive ARPES experiments. Existing and new ARPES measurements on Ce-based systems should carefully be examined from the point of the surface sensitivity of this technique. Furthermore, systems crystallizing in different structures need to be considered too, as our recent study on $CeIrIn_5$ showed [166]. There, similar to $CeRh_2Si_2$, two different $4f$ spectral patterns were found with weakly-hybridized γ-like and more strongly-hybridized Ce $4f$ characteristics, which can be attributed to the CeIn-terminated and In-terminated surface, respectively.

The influence of the surface on the Ce $4f$ properties was further studied in $CeCo_2P_2$. In the bulk, the Ce $4f$ physics are generally described as tetravalently behaving due to the absence of heavy fermions or magnetic moments on the Ce sublattice. On the other hand, the Co moments order antiferromagnetically at an uncommonly high Néel temperature of 440 K. With the help of our ARPES study, we found clear spectral patterns that could be attributed to the P-terminated surface due to the existence of surface states around the $\overline{\mathrm{M}}$ point of the SBZ, which are intrinsic to the electronic structure of this termination. Besides the surface states, the spectrum clearly showed heavy bands around E_F in opposition to the absence of heavy fermions in the bulk. The temperature-dependent measurements revealed that these states vanish with increasing temperature in accordance with Kondo scenario. To explain the observation of these local moment physics in the subsurface Ce layer, which was attributed in $CeRh_2Si_2$ as behaving mostly bulk-like, we turned towards a theoretical description in the framework of DFT+U. While in the bulk, the calculations predicted no magnetic moment on the Ce atoms in accordance with the experimental bulk properties, the subsurface Ce showed a finite magnetic moment in the same direction as the Co moment in the P-Co-P surface trilayer block, which itself exhibited a slightly reduced magnetic moment. To interpret such a change in the surface region, an intuitive picture connected to the antiferromagnetic order of the Co moments was derived. In the bulk, the out-of-plane antiferromagnetic order of the Co moments prevents the Ce $4f$ moments and favors instead a strongly intermediate or close to tetravalent Ce $4f$ configuration. On the other hand, the symmetry breaking at the surface leads to Co moments which are no longer compensated by the neighboring Co layer resulting in an effective magnetic field and electron redistribution at the surface. The resulting effect is a nonzero Ce $4f$ moment oriented in the same way as the uncompensated Co moment in the surface block. To probe the existence of Ce $4f$ moments, we performed X-ray absorption measurements at the Ce $M_{4,5}$ edge sensitive to the Ce $4f$, which revealed at non-zero XMCD signal in accordance with the theoretical description. Note however that we were not able to measure just on surface terminations, thus the origin of the Ce $4f$ moments is not restricted just to the subsurface Ce layer. Additional XMCD measurements on the Co $L_{2,3}$ suggest a coupling between the Ce and Co subsurface sublattices as predicted by the theoretical calculation. Thus, based on our model, $CeCo_2P_2$ gives the unique possibility to study a single buried 2D Kondo lattice layer in detail and its connection to a magnetically ordered Co sublattice in a large temperature range even above room temperature. Similar changes could be expected in other LnT_2X_2 with T = Co, Mn, Fe where magnetic sublattices of the transition elements can interact with magnetic moments on the lanthanides with possible changes expected at surface or interfaces due to symmetry breaking.

The unusual properties of $CeCo_2P_2$ also extend to density of states at E_F, which we predicted to be strongly reduced. While still behaving like a good metal, the Co

3*d* states responsible for the magnetic properties are nearly zero at E_F in both spin channels based on our calculations. Since such a spin gap would lead to a reduced electron-magnon interaction, we performed RIXS measurements to study in detail the spin excitations and their damping. Based on the large ordering temperature and magnetic moments, a strong magnon dispersion with high energies up to the THz regime was expected which we were able to follow experimentally in a significant part of the Brillouin zone. The experimentally determined magnon dispersion corresponded well with the theoretical dispersion calculated based on the linear spin wave theory. The fit of the spin excitation peak allowed us to determine the strength of the magnon damping, which was small over the whole measured energy range up to the THz regime. Only at very high excitation energies in the range of 200 meV were we able to determine a significant, but still small damping. For comparison we used the isostructural $LaCo_2P_2$ which does not have a reduced density of states at E_F. Indeed, for this compound we observed a much larger damping typical for metallic compounds. This comparison further showed the special properties of the one extra electron in Ce in comparison to La which in $CeCo_2P_2$ does not behave localized and instead leads to a strong volume collapse, a very large ordering temperature and a reduced density of states in comparison to $LaCo_2P_2$.

The measurements on both $CeRh_2Si_2$ and $CeCo_2P_2$ visualized how tunable and versatile the Ce 4*f* properties can be in different electronic, chemical or structural environments resulting in competing energy scales and different behaviors. That these physics can be traced back to just one strongly correlated Ce 4*f* electron makes Ce systems the ideal work horse to study many-body effects. In this regard, CeT_2X_2 is one of the most adjustable families that can be studied systematically to improve our understanding of not only Ce physics but also as benchmark to test theoretical approaches and theories. We believe that our ARPES studies presented pedagogically what needs to be considered during measurement and interpretation when studying such systems with surface-sensitive techniques. The combination with 3*d* transition elements allows not only for the coexistence of 3*d* magnetism with 4*f* physics but to a special interaction which can result in a high magnetic ordering temperature, large spin excitations and undamped magnons like we observed in $CeCo_2P_2$.

That the CeT_2X_2 family still has much to offer becomes also apparent in the continuous interest and prediction of new physical properties. While topological properties like for $CeCo_2P_2$ were recently predicted [145], the interplay between CEF splittings, Kondo interaction and local inversion symmetry breaking made $CeRh_2As_2$ to a currently intensely studied system [81, 167–171]. Hence, this thesis should be seen as a puzzle piece trying to improve our knowledge in the large picture of Ce-based intermetallics. And whether it is with the help of new systems, improved sample qualities or measurements under pressure, at surfaces and interfaces, under magnetic fields or under doping, Ce-based intermetallic systems have still so much to offer in finding new properties and phases, testing and improving our many-body models and theories or even creating usable quantum devices.

Acronyms

AFM antiferromagnet

ARPES angle-resolved photoemission spectroscopy

BIS bremsstrahlung isochromat spectroscopy

CEF crystalline electric field

DFT density functional theory

DMFT dynamical mean field theory

EDC energy distribution curve

FDD Fermi-Dirac distribution

GGA generalized gradient approximation

LDA linear density approximation

LEED low-energy electron diffraction

RIXS resonant inelastic X-ray scattering

RKKY Ruderman-Kittel-Kasuya-Yosida

SBZ surface Brillouin zone

SOC spin-orbit coupling

UV ultra violet

XMCD X-ray magnetic circular dichroism

XMLD X-ray magnetic linear dichroism

Bibliography

1. Anderson, P. W. "Local Moments and Localized States". *Science* **201,** 307–316 (1978).
2. Dagotto, E. "Complexity in Strongly Correlated Electronic Systems". *Science* **309,** 257–262 (2005).
3. Kondo, J. "Resistance Minimum in Dilute Magnetic Alloys". *Progress of Theoretical Physics* **32,** 37–49 (1964).
4. de Haas, W., de Boer, J. & van dën Berg, G. "The electrical resistance of gold, copper and lead at low temperatures". *Physica* **1,** 1115–1124 (1934).
5. Jensen, J. & Mackintosh, A. R. "Rare earth magnetism" (Clarendon Press Oxford, 1991).
6. Freeman, A. J. & Watson, R. E. "Theoretical Investigation of Some Magnetic and Spectroscopic Properties of Rare-Earth Ions". *Phys. Rev.* **127,** 2058–2075 (1962).
7. Herbst, J. & Croat, J. "Neodymium-iron-boron permanent magnets". *Journal of Magnetism and Magnetic Materials* **100,** 57–78 (1991).
8. Coleman, P. "Heavy Fermions: Electrons at the Edge of Magnetism". in *Handbook of Magnetism and Advanced Magnetic Materials* (John Wiley & Sons, Ltd, 2007).
9. Lawson, A. W. & Tang, T.-Y. "Concerning the High Pressure Allotropic Modification of Cerium". *Phys. Rev.* **76,** 301–302 (1949).
10. Edelstein, A. S. "Spin Compensation in an Element, Cerium". *Phys. Rev. Lett.* **20,** 1348–1351 (1968).
11. Lavagna, M., Lacroix, C. & Cyrot, M. "The γ-α transition in cerium compounds". *Journal of Physics F: Metal Physics* **13,** 1007–1015 (1983).
12. Allen, J. W. & Liu, L. Z. "α-γ transition in Ce. II. A detailed analysis of the Kondo volume-collapse model". *Phys. Rev. B* **46,** 5047–5054 (1992).
13. Andres, K., Graebner, J. E. & Ott, H. R. "$4f$-Virtual-Bound-State Formation in $CeAl_3$ at Low Temperatures". *Phys. Rev. Lett.* **35,** 1779–1782 (1975).
14. Allen, J. W. "The Kondo Resonance in Electron Spectroscopy". *Journal of the Physical Society of Japan* **74,** 34–48 (2005).
15. Schrödinger, E. "Quantisierung als Eigenwertproblem". *Annalen der Physik* **384,** 361–376 (1926).

16. Schrödinger, E. "Quantisierung als Eigenwertproblem". *Annalen der Physik* **385,** 437–490 (1926).
17. Born, M. & Oppenheimer, R. "Zur Quantentheorie der Molekeln". *Annalen der Physik* **389,** 457–484 (1927).
18. Hartree, D. R. "The Wave Mechanics of an Atom with a Non-Coulomb Central Field. Part I. Theory and Methods". *Mathematical Proceedings of the Cambridge Philosophical Society* **24,** 89–110 (1928).
19. Hartree, D. R. "The Wave Mechanics of an Atom with a Non-Coulomb Central Field. Part II. Some Results and Discussion". *Mathematical Proceedings of the Cambridge Philosophical Society* **24,** 111–132 (1928).
20. Fock, V. "Näherungsmethode zur Lösung des quantenmechanischen Mehrkörperproblems". *Zeitschrift für Physik* **61,** 126–148 (1930).
21. Wormer, P. E. S. & de Groot, F. "The potential energy surface of triplet H_3^+: A representation in hyperspherical coordinates". *The Journal of Chemical Physics* **90,** 2344–2356 (1989).
22. Condon, E. U. & Shortley, G. H. "The theory of atomic spectra" (Cambridge University Press, 1935).
23. Slater, J. C. "The Theory of Complex Spectra". *Phys. Rev.* **34,** 1293–1322 (1929).
24. Sievers, J. "Asphericity of $4f$-shells in their Hund's rule ground states". *Zeitschrift für Physik B Condensed Matter* **45,** 289–296 (1982).
25. Stevens, K. W. H. "Matrix Elements and Operator Equivalents Connected with the Magnetic Properties of Rare Earth Ions". *Proceedings of the Physical Society. Section A* **65,** 209–215 (1952).
26. Wigner, E. "Über die Operation der Zeitumkehr in der Quantenmechanik". *Nachrichten von der Gesellschaft der Wissenschaften zu Göttingen, Mathematisch-Physikalische Klasse,* 546–559 (1932).
27. Bloch, F. "Über die Quantenmechanik der Elektronen in Kristallgittern". *Zeitschrift für Physik* **52,** 555–600 (1929).
28. Fermi, E. "Zur Quantelung des idealen einatomigen Gases". *Zeitschrift für Physik* **36,** 902–912 (1926).
29. Dirac, P. A. M. & Fowler, R. H. "On the theory of quantum mechanics". *Proceedings of the Royal Society of London. Series A, Containing Papers of a Mathematical and Physical Character* **112,** 661–677 (1926).
30. Hohenberg, P. & Kohn, W. "Inhomogeneous Electron Gas". *Phys. Rev.* **136,** B864–B871 (1964).
31. Levy, M. "Universal variational functionals of electron densities, first-order density matrices, and natural spin-orbitals and solution of the v-representability problem". *Proceedings of the National Academy of Sciences* **76,** 6062–6065 (1979).

32. Lieb, E. H. “Density functionals for Coulomb systems”. *International Journal of Quantum Chemistry* **24,** 243–277 (1983).
33. Kohn, W. & Sham, L. J. “Self-Consistent Equations Including Exchange and Correlation Effects”. *Phys. Rev.* **140,** A1133–A1138 (1965).
34. Becke, A. D. “Density-functional exchange-energy approximation with correct asymptotic behavior”. *Phys. Rev. A* **38,** 3098–3100 (1988).
35. Becke, A. D. “A new mixing of Hartree–Fock and local density-functional theories”. *The Journal of Chemical Physics* **98,** 1372–1377 (1993).
36. Hewson, A. C. “The Kondo Problem to Heavy Fermions” (Cambridge University Press, 1993).
37. Anderson, P. W. “Localized Magnetic States in Metals”. *Phys. Rev.* **124,** 41–53 (1961).
38. Schrieffer, J. R. & Wolff, P. A. “Relation between the Anderson and Kondo Hamiltonians”. *Phys. Rev.* **149,** 491–492 (1966).
39. Zener, C. “Interaction Between the *d* Shells in the Transition Metals”. *Phys. Rev.* **81,** 440–444 (1951).
40. Suhl, H. “Dispersion Theory of the Kondo Effect”. *Phys. Rev.* **138,** A515–A523 (1965).
41. Anderson, P. W. “A poor man’s derivation of scaling laws for the Kondo problem”. *Journal of Physics C: Solid State Physics* **3,** 2436–2441 (1970).
42. Wilson, K. G. “The renormalization group: Critical phenomena and the Kondo problem”. *Rev. Mod. Phys.* **47,** 773–840 (1975).
43. Vigman, P. B. “Exact solution of s-d exchange model at T = 0”. *Soviet Journal of Experimental and Theoretical Physics Letters* **31,** 392 (1980).
44. Andrei, N. “Diagonalization of the Kondo Hamiltonian”. *Phys. Rev. Lett.* **45,** 379–382 (1980).
45. Nozières, P. “A “fermi-liquid” description of the Kondo problem at low temperatures”. *Journal of Low Temperature Physics* **17,** 31–42 (1974).
46. Suhl, H. “Paramagnetic impurities in metals at finite temperatures”. *Physics Physique Fizika* **2,** 39–59 (1965).
47. Abrikosov, A. A. “Electron scattering on magnetic impurities in metals and anomalous resistivity effects”. *Physics Physique Fizika* **2,** 5–20 (1965).
48. Ruderman, M. A. & Kittel, C. “Indirect Exchange Coupling of Nuclear Magnetic Moments by Conduction Electrons”. *Phys. Rev.* **96,** 99–102 (1954).
49. Kasuya, T. “A Theory of Metallic Ferro- and Antiferromagnetism on Zener’s Model”. *Progress of Theoretical Physics* **16,** 45–57 (1956).
50. Yosida, K. “Magnetic Properties of Cu-Mn Alloys”. *Phys. Rev.* **106,** 893–898 (1957).

51. Doniach, S. "The Kondo lattice and weak antiferromagnetism". *Physica B+C* **91,** 231–234 (1977).
52. Fisk, Z., Ott, H. R., Rice, T. M. & Smith, J. L. "Heavy-electron metals". *Nature* **320,** 124–129 (1986).
53. Heisenberg, W. "Zur Theorie des Ferromagnetismus". *Zeitschrift für Physik* **49,** 619–636 (1928).
54. Bethe, H. "Zur Theorie der Metalle". *Zeitschrift für Physik* **71,** 205–226 (1931).
55. Anderson, P. W. "Limits on the Energy of the Antiferromagnetic Ground State". *Phys. Rev.* **83,** 1260–1260 (1951).
56. Holstein, T. & Primakoff, H. "Field Dependence of the Intrinsic Domain Magnetization of a Ferromagnet". *Phys. Rev.* **58,** 1098–1113 (1940).
57. Toth, S. & Lake, B. "Linear spin wave theory for single-Q incommensurate magnetic structures". *Journal of Physics: Condensed Matter* **27,** 166002 (2015).
58. Dirac, P. A. M. & Bohr, N. H. D. "The quantum theory of the emission and absorption of radiation". *Proceedings of the Royal Society of London. Series A, Containing Papers of a Mathematical and Physical Character* **114,** 243–265 (1927).
59. Fermi, E. "Nuclear physics: a course given by Enrico Fermi at the University of Chicago" (University of Chicago Press, 1950).
60. Wigner, E. "Einige Folgerungen aus der Schrödingerschen Theorie für die Termstrukturen". *Zeitschrift für Physik* **43,** 624–652 (1927).
61. Thole, B. T., Carra, P., Sette, F. & van der Laan, G. "X-ray circular dichroism as a probe of orbital magnetization". *Phys. Rev. Lett.* **68,** 1943–1946 (1992).
62. Carra, P., Thole, B. T., Altarelli, M. & Wang, X. "X-ray circular dichroism and local magnetic fields". *Phys. Rev. Lett.* **70,** 694–697 (1993).
63. Chen, C. T. *et al.* "Experimental Confirmation of the X-Ray Magnetic Circular Dichroism Sum Rules for Iron and Cobalt". *Phys. Rev. Lett.* **75,** 152–155 (1995).
64. Gunnarsson, O. & Schönhammer, K. "Electron spectroscopies for Ce compounds in the impurity model". *Phys. Rev. B* **28,** 4315–4341 (1983).
65. Abbate, M. *et al.* "Probing depth of soft x-ray absorption spectroscopy measured in total-electron-yield mode". *Surface and Interface Analysis* **18,** 65–69 (1992).
66. Hertz, H. "Ueber einen Einfluss des ultravioletten Lichtes auf die electrische Entladung". *Annalen der Physik* **267,** 983–1000 (1887).
67. Einstein, A. "Zur Theorie der Lichterzeugung und Lichtabsorption". *Annalen der Physik* **325,** 199–206 (1906).
68. Hüfner, S. & Huber, T. "Photoelectron Spectroscopy: Principles and Applications" (Springer, 2003).

69. Damascelli, A. "Probing the Electronic Structure of Complex Systems by ARPES". *Physica Scripta* **T109,** 61 (2004).
70. Hedin, L. & Lee, J. "Sudden approximation in photoemission and beyond". *Journal of Electron Spectroscopy and Related Phenomena* **124.** Frontiers in photoemission spectroscopy of solids and surfaces, 289–315 (2002).
71. Kramers, H. A. & Heisenberg, W. "Über die Streuung von Strahlung durch Atome". *Zeitschrift für Physik* **31,** 681–708 (1925).
72. Ament, L. J. P., van Veenendaal, M., Devereaux, T. P., Hill, J. P. & van den Brink, J. "Resonant inelastic x-ray scattering studies of elementary excitations". *Rev. Mod. Phys.* **83,** 705–767 (2011).
73. Brookes, N. *et al.* "The beamline ID32 at the ESRF for soft X-ray high energy resolution resonant inelastic X-ray scattering and polarisation dependent X-ray absorption spectroscopy". *Nuclear Instruments and Methods in Physics Research Section A: Accelerators, Spectrometers, Detectors and Associated Equipment* **903,** 175–192 (2018).
74. Burdin, S., Georges, A. & Grempel, D. R. "Coherence Scale of the Kondo Lattice". *Phys. Rev. Lett.* **85,** 1048–1051 (2000).
75. Burdin, S. & Zlati ć, V. "Multiple temperature scales of the periodic Anderson model: Slave boson approach". *Phys. Rev. B* **79,** 115139 (2009).
76. Benlagra, A., Pruschke, T. & Vojta, M. "Finite-temperature spectra and quasiparticle interference in Kondo lattices: From light electrons to coherent heavy quasiparticles". *Phys. Rev. B* **84,** 195141 (2011).
77. Kang, H., Haule, K., Kotliar, G., Coleman, P. & Shim, J.-H. "Energy scales of the doped Anderson lattice model". *Phys. Rev. B* **99,** 165115 (2019).
78. Ōnuki, Y. & Komatsubara, T. "Heavy fermion state in $CeCu_6$". *Journal of Magnetism and Magnetic Materials* **63-64,** 281–288 (1987).
79. Steglich, F. *et al.* "Superconductivity in the Presence of Strong Pauli Paramagnetism: $CeCu_2Si_2$". *Phys. Rev. Lett.* **43,** 1892–1896 (1979).
80. Petrovic, C. *et al.* "Heavy-fermion superconductivity in $CeCoIn_5$ at 2.3 K". *Journal of Physics: Condensed Matter* **13,** L337–L342 (2001).
81. Khim, S. *et al.* "Field-induced transition within the superconducting state of $CeRh_2As_2$". *Science* **373,** 1012–1016 (2021).
82. Dzero, M., Sun, K., Galitski, V. & Coleman, P. "Topological Kondo Insulators". *Phys. Rev. Lett.* **104,** 106408 (2010).
83. Lai, H.-H., Grefe, S. E., Paschen, S. & Si, Q. "Weyl-Kondo semimetal in heavy-fermion systems". *Proceedings of the National Academy of Sciences* **115,** 93–97 (2018).
84. Johansson, L., Allen, J., Gustafsson, T., Lindau, I. & Hagstrom, S. "Giant enhancement of the valence band photoemission intensity in γ-Ce". *Solid State Communications* **28,** 53–55 (1978).

85. Allen, J. *et al.* "Electronic structure of cerium and light rare-earth intermetallics". *Advances in Physics* **35,** 275–316 (1986).

86. Gegenwart, P. *et al.* "Non-Fermi-Liquid Effects at Ambient Pressure in a Stoichiometric Heavy-Fermion Compound with Very Low Disorder: $\mathrm{CeNi_2Ge_2}$". *Phys. Rev. Lett.* **82,** 1293–1296 (1999).

87. Hosono, H. *et al.* "Exploration of new superconductors and functional materials, and fabrication of superconducting tapes and wires of iron pnictides". *Science and Technology of Advanced Materials* **16,** 033503 (2015).

88. Quezel, S., Rossat-Mignod, J., Chevalier, B., Lejay, P. & Etourneau, J. "Magnetic ordering in $\mathrm{TbRh_2Si_2}$ and $\mathrm{CeRh_2Si_2}$". *Solid State Communications* **49,** 685–691 (1984).

89. Grier, B. H., Lawrence, J. M., Murgai, V. & Parks, R. D. "Magnetic ordering in $\mathrm{Ce}M_2\mathrm{Si_2}$ (M =Ag,Au,Pd,Rh) compounds as studied by neutron diffraction". *Phys. Rev. B* **29,** 2664–2672 (1984).

90. Kawarazaki, S. *et al.* "Neutron diffraction study on the magnetism of the $\mathrm{Ce(Ru_{1-x}Rh_x)_2Si_2}$ mixed compound system". *Physica B: Condensed Matter* **206-207,** 298–300 (1995).

91. Severing, A., Holland-Moritz, E. & Frick, B. "Spin dynamics of $\mathrm{CeX_2Si_2}$ (X=Au, Pd, Rh, Ru)". *Phys. Rev. B* **39,** 4164–4174 (1989).

92. Willers, T. *et al.* "Spectroscopic determination of crystal-field levels in $\mathrm{CeRh_2Si_2}$ and $\mathrm{CeRu_2Si_2}$ and of the $4f^0$ contributions in $\mathrm{Ce}M_2\mathrm{Si_2}$ (M=Cu, Ru, Rh, Pd, and Au)". *Phys. Rev. B* **85,** 035117 (2012).

93. Kawasaki, Y., Ishida, K., Kitaoka, Y. & Asayama, K. "Si-NMR study of antiferromagnetic heavy-fermion compounds $\mathrm{CePd_2Si_2}$ and $\mathrm{CeRh_2Si_2}$". *Phys. Rev. B* **58,** 8634–8639 (1998).

94. Amorese, A. *et al.* "Crystal electric field in $\mathrm{CeRh_2Si_2}$ studied with high-resolution resonant inelastic soft X-ray scattering". *Phys. Rev. B* **97,** 245130 (2018).

95. Patil, S. *et al.* "ARPES view on surface and bulk hybridization phenomena in the antiferromagnetic Kondo lattice $\mathrm{CeRh_2Si_2}$". *Nature Communications* **7,** 11029 (2016).

96. Hoesch, M. *et al.* "A facility for the analysis of the electronic structures of solids and their surfaces by synchrotron radiation photoelectron spectroscopy". *Review of Scientific Instruments* **88,** 013106 (2017).

97. Kucherenko, Y. *et al.* "Giant hybridization effects in $4f$ photoemission spectra of Pr and Nd transition-metal compounds". *Phys. Rev. B* **65,** 165119 (2002).

98. Laubschat, C., Grentz, W. & Kaindl, G. "$4f$ multiplets in bremsstrahlung-isochromat spectroscopy as a probe for local electron density in Ce compounds". *Phys. Rev. B* **36,** 8233–8236 (1987).

99. Jang, S. *et al.* "Evolution of the Kondo lattice electronic structure above the transport coherence temperature". *Proceedings of the National Academy of Sciences* **117,** 23467–23476 (2020).
100. Rajan, V. T., Lowenstein, J. H. & Andrei, N. "Thermodynamics of the Kondo Model". *Phys. Rev. Lett.* **49,** 497–500 (1982).
101. Mel'nikov, V. I. "Thermodynamics of the Kondo problem". *ZhETF Pisma Redaktsiiu* **35,** 414 (1982).
102. Desgranges, H.-U. & Schotte, K. "Specific heat of the Kondo model". *Physics Letters A* **91,** 240–242 (1982).
103. Desgranges, H.-U. "Crystal fields and Kondo effect: Specific heat for Cerium compounds". *Physica B: Condensed Matter* **454,** 135–140 (2014).
104. Cornut, B. & Coqblin, B. "Influence of the Crystalline Field on the Kondo Effect of Alloys and Compounds with Cerium Impurities". *Phys. Rev. B* **5,** 4541–4561 (1972).
105. Jones, E., Oliphant, T., Peterson, P., *et al. SciPy: Open source scientific tools for Python* [Online; accessed 2019-08-14]. 2001–.
106. Branch, M., Coleman, T. & Li, Y. "A Subspace, Interior, and Conjugate Gradient Method for Large-Scale Bound-Constrained Minimization Problems". *SIAM Journal on Scientific Computing* **21,** 1–23 (1999).
107. Vyalikh, D. V. *et al.* "k Dependence of the Crystal-Field Splittings of $4f$ States in Rare-Earth Systems". *Phys. Rev. Lett.* **105,** 237601 (2010).
108. Koepernik, K. & Eschrig, H. "Full-potential nonorthogonal local-orbital minimum-basis band-structure scheme". *Phys. Rev. B* **59,** 1743–1757 (1999).
109. Kratochvílová, M. *et al.* "Coexistence of Antiferromagnetism and Superconductivity in Heavy Fermion Cerium Compound Ce_3PdIn_{11}". *Scientific Reports* **5** (2015).
110. Prokleška, J., Kratochvílová, M., Uhlířová, K., Sechovský, V. & Custers, J. "Magnetism, superconductivity, and quantum criticality in the multisite cerium heavy-fermion compound Ce_3PtIn_{11}". *Phys. Rev. B* **92,** 161114 (2015).
111. Reehuis, M., Jeitschko, W., Kotzyba, G., Zimmer, B. & Hu, X. "Antiferromagnetic Order in the $ThCr_2Si_2$ Type Phosphides $CaCo_2P_2$ and $CeCo_2P_2$". *J. Alloys Compd.* **266,** 54–60 (1998).
112. Jeitschko, W., Meisen, U., Möller, M. H. & Reehuis, M. "Über $LaCo_2P_2$ und andere Neue Verbindungen mit $ThCr_2Si_2$- und $CaBe_2Ge_2$-Struktur". *Z. anorg. allg. Chem.* **527,** 73–84 (1985).
113. Reehuis, M. & Jeitschko, W. "Structure and Magnetic Properties of the Phosphides $CaCo_2P_2$ and LnT_2P_2 with $ThCr_2Si_2$ Structure and LnTP with PbFCl Structure (Ln = Lanthanoids, T = Fe, Co, Ni)†". *J. Phys. Chem. Solids* **51,** 961–968 (1990).

114. Kliemt, L. *et al.* "Crystal Growth of Materials with the $ThCr_2Si_2$ Structure Type". *Cryst. Res. Technol.* **55,** 1900116 (2020).

115. Usachov, D. Y. *et al.* "Photoelectron Diffraction for Probing Valency and Magnetism of 4f-Based Materials: A View on Valence-Fuctuating $EuIr_2Si_2$". *Phys. Rev. B* **102,** 205102 (2020).

116. Generalov, A. *et al.* "Spin Orientation of Two-Dimensional Electrons Driven by Temperature-Tunable Competition of Spin–Orbit and Exchange–Magnetic Interactions". *Nano Lett.* **17,** 811–820 (2017).

117. Güttler, M. *et al.* "Robust and Tunable Itinerant Ferromagnetism at the Silicon Surface of the Antiferromagnet $GdRh_2Si_2$". *Sci. Rep.* **6,** 24254 (2016).

118. Danzenbächer, S. *et al.* "Insight into the f-Derived Fermi Surface of the Heavy-Fermion Compound $YbRh_2Si_2$". *Phys. Rev. Lett.* **107,** 267601 (2011).

119. Generalov, A. *et al.* "Strong Spin-Orbit Coupling in the Noncentrosymmetric Kondo Lattice". *Phys. Rev. B* **98,** 115157 (2018).

120. Schulz, S. *et al.* "Emerging 2D-Ferromagnetism and Strong Spin-Orbit Coupling at the Surface of Valence-Fluctuating $EuIr_2Si_2$". *npj Quantum Mater.* **4,** 26 (2019).

121. Gunnarsson, O. & Schönhammer, K. "Photoemission from Ce Compounds: Exact Model Calculation in the Limit of Large Degeneracy". *Phys. Rev. Lett.* **50,** 604–607 (1983).

122. Chen, Q. Y. *et al.* "Direct Observation of how the Heavy-Fermion State Develops in $CeCoIn_5$". *Phys. Rev. B* **96,** 045107 (2017).

123. Chen, Q. Y. *et al.* "Band Dependent Interlayer f-Electron Hybridization in $CeRhIn_5$". *Phys. Rev. Lett.* **120,** 066403 (2018).

124. Santander-Syro, A. F. *et al.* "Fermi-Surface Instability at the 'Hidden-Order' Transition of URu_2Si_2". *Nature Phys.* **5,** 637–641 (2009).

125. Sergentu, D.-C., Booth, C. H. & Autschbach, J. "Probing Multiconfigurational States by Spectroscopy: The Cerium XAS L_3-edge Puzzle". *Chem. Eur. J.* **27,** 7239–7251 (2021).

126. Kaindl, G., Wertheim, G. K., Schmiester, G. & Sampathkumaran, E. V. "Mixed Valency versus Covalency in Rare-Earth Core-Electron Spectroscopy". *Phys. Rev. Lett.* **58,** 606–609 (1987).

127. Kotani, A., Jo, T. & Parlebas, J. C. "Many-Body Effects in Core-Level Spectroscopy of Rare-Earth Compounds". *Adv. Phys.* **37,** 37–85 (1988).

128. Michels, G. *et al.* "Final-State Effects in Divalent Eu Pnictides". *J. Phys. Condens. Matter* **6,** 1769–1778 (1994).

129. Ozaki, T. "Variationally Optimized Atomic Orbitals for Large-Scale Electronic Structures". *Phys. Rev. B* **67,** 155108 (2003).

130. Hoffmann, M. *et al.* "Magnetic and Electronic Properties of Complex Oxides from First-Principles". *Phys. Status Solidi B* **257,** 1900671 (2020).
131. Kruglyak, V. V., Demokritov, S. O. & Grundler, D. "Magnonics". *J. Phys. D: Appl. Phys.* **43,** 264001 (2010).
132. Lenk, B., Ulrichs, H., Garbs, F. & Münzenberg, M. "The building blocks of magnonics". *Physics Reports* **507,** 107–136 (2011).
133. Chumak, A. V., Vasyuchka, V. I., Serga, A. A. & Hillebrands, B. "Magnon spintronics". *Nature Physics* **11,** 453–461 (2015).
134. Barman, A. *et al.* "The 2021 Magnonics Roadmap". *J. Phys. Condens. Matter* **33,** 413001 (2021).
135. Van Kranendonk, J. & van Vleck, J. H. "Spin Waves". *Rev. Mod. Phys.* **30,** 1–23 (1958).
136. Prabhakar, A. & Stancil, D. D. "Spin Waves: Theory and Applications" (Springer, 2009).
137. Chumak, A. V., Serga, A. A. & Hillebrands, B. "Magnon transistor for all-magnon data processing". *Nat. Commun.* **5,** 4700 (2014).
138. Mahmoud, A. *et al.* "Introduction to spin wave computing". *Journal of Applied Physics* **128,** 161101 (2020).
139. Zakeri, K. "Terahertz magnonics: Feasibility of using terahertz magnons for information processing". *Physica C: Superconductivity and its Applications* **549,** 164–170 (2018).
140. Zakeri, K. "Elementary spin excitations in ultrathin itinerant magnets". *Physics Reports* **545,** 47–93 (2014).
141. Costa, A. T., Muniz, R. B. & Mills, D. L. "Spin waves and their damping in itinerant ultrathin ferromagnets: Intermediate wave vectors". *Phys. Rev. B* **74,** 214403 (2006).
142. Liu, C., Mewes, C. K. A., Chshiev, M., Mewes, T. & Butler, W. H. "Origin of low Gilbert damping in half metals". *Applied Physics Letters* **95,** 022509 (2009).
143. Buczek, P., Ernst, A. & Sandratskii, L. M. "Different dimensionality trends in the Landau damping of magnons in iron, cobalt, and nickel: Time-dependent density functional study". *Phys. Rev. B* **84,** 174418 (2011).
144. Qin, H. J. *et al.* "Long-living terahertz magnons in ultrathin metallic ferromagnets". *Nat. Commun.* **6,** 6126 (2015).
145. Xu, Y. *et al.* "High-Throughput Calculations of Magnetic Topological Materials". *Nature* **586,** 702–707 (2020).
146. Imai, M., Michioka, C., Ueda, H. & Yoshimura, K. "Static and dynamical magnetic properties of the itinerant ferromagnet $LaCo_2P_2$". *Phys. Rev. B* **91,** 184414 (2015).

147. Kovnir, K., Thompson, C. M., Zhou, H. D., Wiebe, C. R. & Shatruk, M. "Tuning Ferro-and Metamagnetic Transitions in Rare-Earth Cobalt Phosphides $La_{1-x}Pr_xCo_2P_2$". *Chem. Mater.* **22,** 1704–1713 (2010).

148. M., R., Ritter, C., Ballou, R. & Jeitschko, W. "Ferromagnetism in the $ThCr_2Si_2$ type phosphide $LaCo_2P_2$". *J. Magn. Magn. Mater.* **138,** 85–93 (1994).

149. Teruya, A. *et al.* "De Haas-van Alphen Effect and Fermi Surface Properties in Ferromagnet $LaCo_2P_2$ and Related Compounds". *Physics Procedia* **75.** 20th International Conference on Magnetism, ICM 2015, 876–883 (2015).

150. Huhnt, C., Schlabitz, W., Wurth, A., Mewis, A. & Reehuis, M. "First- and second-order phase transitions in ternary europium phosphides with $ThCr_2Si_2$-type structure". *Physica B: Condensed Matter* **252,** 44–54 (1998).

151. Yang, W. L. *et al.* "Evidence for weak electronic correlations in iron pnictides". *Phys. Rev. B* **80,** 014508 (2009).

152. Rahn, M. C. *et al.* "Paramagnon dispersion in β-FeSe observed by Fe L-edge resonant inelastic x-ray scattering". *Phys. Rev. B* **99,** 014505 (2019).

153. Brookes, N. B. *et al.* "Spin waves in metallic iron and nickel measured by soft x-ray resonant inelastic scattering". *Phys. Rev. B* **102,** 064412 (2020).

154. Monney, C. *et al.* "Resonant inelastic x-ray scattering study of the spin and charge excitations in the overdoped superconductor $La_{1.77}Sr_{0.23}CuO_4$". *Phys. Rev. B* **93,** 075103 (2016).

155. Peng, Y. Y. *et al.* "Dispersion, damping, and intensity of spin excitations in the monolayer $(Bi,Pb)_2(Sr,La)_2CuO_{6+\delta}$ cuprate superconductor family". *Phys. Rev. B* **98,** 144507 (2018).

156. Robarts, H. C. *et al.* "Anisotropic damping and wave vector dependent susceptibility of the spin fluctuations in $La_{2-x}Sr_xCuO_4$ studied by resonant inelastic x-ray scattering". *Phys. Rev. B* **100,** 214510 (2019).

157. Doležal, P. *et al.* "Lattice dynamics in $CePd_2Al_2$ and $LaPd_2Al_2$". *Scientific Reports* **11,** 20878 (2021).

158. Perdew, J. P., Burke, K. & Ernzerhof, M. "Generalized Gradient Approximation Made Simple". *Phys. Rev. Lett.* **77,** 3865–3868 (1996).

159. Anisimov, V. I., Zaanen, J. & Andersen, O. K. "Band theory and Mott insulators: Hubbard U instead of Stoner I". *Phys. Rev. B* **44,** 943–954 (1991).

160. Dudarev, S. L., Botton, G. A., Savrasov, S. Y., Humphreys, C. J. & Sutton, A. P. "Electron-energy-loss spectra and the structural stability of nickel oxide: An LSDA+U study". *Phys. Rev. B* **57,** 1505–1509 (1998).

161. Liechtenstein, A. I., Katsnelson, M. I., Antropov, V. P. & Gubanov, V. A. "Local spin density functional approach to the theory of exchange interactions in ferromagnetic metals and alloys". *Journal of Magnetism and Magnetic Materials* **67,** 65–74 (1987).

162. Des Cloizeaux, J. & Pearson, J. J. "Spin-Wave Spectrum of the Antiferromagnetic Linear Chain". *Phys. Rev.* **128,** 2131–2135 (1962).
163. Buczek, P., Ernst, A., Bruno, P. & Sandratskii, L. M. "Energies and Lifetimes of Magnons in Complex Ferromagnets: A First-Principle Study of Heusler Alloys". *Phys. Rev. Lett.* **102,** 247206 (2009).
164. Marmodoro, A., Mankovsky, S., Ebert, H., Minár, J. & Šipr, O. "Electric field control of magnons in magnetic thin films: Ab initio predictions for two-dimensional metallic heterostructures". *Phys. Rev. B* **105,** 174411 (2022).
165. Zhang, J. *et al.* "Magnons in ferromagnetic metallic manganites". *Journal of Physics: Condensed Matter* **19,** 315204 (2007).
166. Mende, M. *et al.* "Strong Rashba Effect and Different $f - d$ Hybridization Phenomena at the Surface of the Heavy-Fermion Superconductor $CeIrIn_5$". *Advanced Electronic Materials* **8,** 2100768 (2022).
167. Kitagawa, S. *et al.* "Two-Dimensional XY-Type Magnetic Properties of Locally Noncentrosymmetric Superconductor $CeRh_2As_2$". *Journal of the Physical Society of Japan* **91,** 043702 (2022).
168. Möckli, D. & Ramires, A. "Two scenarios for superconductivity in $CeRh_2A_2$". *Phys. Rev. Research* **3,** 023204 (2021).
169. Kimura, S.-i., Sichelschmidt, J. & Khim, S. "Optical study of the electronic structure of locally noncentrosymmetric $CeRh_2A_2$". *Phys. Rev. B* **104,** 245116 (2021).
170. Nogaki, K., Daido, A., Ishizuka, J. & Yanase, Y. "Topological crystalline superconductivity in locally noncentrosymmetric $CeRh_2As_2$". *Phys. Rev. Research* **3,** L032071 (2021).
171. Mishra, S., Liu, Y., Bauer, E. D., Ronning, F. & Thomas, S. M. "Anisotropic magnetotransport properties of the heavy-fermion superconductor $CeRh_2As_2$". *Phys. Rev. B* **106,** L140502 (2022).

List of Figures

Acknowledgments

Even though this chapter is at the very end of my thesis, it is a very important chapter for me! Without the help and support from all the people below, this work would not have been possible.

In first place, I would like to thank my supervisor Kurt Kummer. After my start, which was unfortunately postponed several times due to COVID, my work here at the ESRF has been filled with openness and kindness. Kurt always has an open ear to discuss new ideas no matter how naive or feasible they are. And he always gave my the freedom to try things on my own, whether it was playing with data sets or performing calculations, which unfortunately did not always lead to a successful conclusion and often took longer than expected. I thank him for his patients and for the nice time we had together. The same can be said about my official supervisor Nicholas Brookes who is always ready to answer questions and help when possible.

Besides Kurt and Nick, I want to say thank you to the other (current and also former) members of ID32, especially Roberto, Davide, Flora and Pamela, who have created such a friendly and enjoyable environment in the ESRF and at the beamline.

For my time at the TU Dresden, I first and foremost want to thank Professor Laubschat for the fruitful years in his group starting from my Bachelor thesis. I am very grateful for his continual willingness to support and help, especially during the time when my start at the ESRF was delayed. His readiness to discuss and talk, whether scientific or not, is something I will never forget.

And then there is Denis Vyalikh, to whom I am deeply thankful for all the encouragement, guidance and productive work together. His believe and strive for sharp bands, high motivation and optimism are something that is inspiring and has always resulted in beamtimes with outstanding data. I am also grateful for all the uncomplicated and honest discussions and the willingness to support new ideas and stories. I am grateful to Denis and all the members of the TU Dresden group, namely Susanne, Monika, Max and Steffen, as well as Alexander Generalov, for the successful beamtimes we spent together. I am especially thankful to Susanne for the making many of the long and exhausting night shifts more bearable. I will fondly remember all the nice times with this group, not only at beamtimes, but also at conferences, workshops or just eating donuts together.

All the measurements would not have been possible without the groups around Cornelius Krellner and Christoph Geibel who not only grew the samples, but gave important inputs for the preparation of the manuscripts. For the great theoretical support and many discussions, I would like to thank Arthur Ernst, Evgueni

Chulkov, Igor Rusinov and Yuri Kucherenko. Special thanks also to Jim Allen who significantly improved our manuscript with his extensive knowledge.

Finally, I wish to thank my family for their ongoing and unconditional support.

List of Publications

In the following, a list of all peer-reviewed publications published at the date of the submission is given.

1. Tarasov, A. V., Glazkova, D., Schulz, S., Poelchen, G., Kliemt, K., Kraiker, A., Muntwiler, M., Laubschat, C., Generalov, A., Polley, C., Krellner, C., Vyalikh, D. V. & Usachov, D. Y. "Crystal electric field and properties of $4f$ magnetic moments at the surface of the rare-earth compound $TbRh_2Si_2$". *Phys. Rev. B* **106**, 155136 (2022).

2. Usachov, D. Y., Glazkova, D., Tarasov, A. V., Schulz, S., Poelchen, G., Bokai, K. A., Vilkov, O. Y., Dudin, P., Kummer, K., Kliemt, K., Krellner, C. & Vyalikh, D. V. "Estimating the Orientation of 4f Magnetic Moments by Classical Photoemission". *J. Phys. Chem. Lett.* **13**, 7861–7869 (2022).

3. Tarasov, A. V., Mende, M., Ali, K., Poelchen, G., Schulz, S., Vilkov, O. Y., Bokai, K. A., Muntwiler, M., Mandic, V., Laubschat, C., Kliemt, K., Krellner, C., Vyalikh, D. V. & Usachov, D. Y. "Structural instability at the In-terminated surface of the heavy-fermion superconductor $CeIrIn_5$". *Surf. Interfaces* **32**, 102126 (2022).

4. Poelchen, G., Rusinov, I. P., Schulz, S., Güttler, M., Mende, M., Generalov, A., Usachov, D. Y., Danzenbächer, S., Hellwig, J., Peters, M., Kliemt, K., Kucherenko, Y., Antonov, V. N., Laubschat, C., Chulkov, E. V., Ernst, A., Kummer, K., Krellner, C. & Vyalikh, D. V. "Interlayer Coupling of a Two-Dimensional Kondo Lattice with a Ferromagnetic Surface in the Antiferromagnet $CeCo_2P_2$". *ACS Nano* **16**, 3573–3581 (2022).

5. Mende, M., Ali, K., Poelchen, G., Schulz, S., Mandic, V., Tarasov, A. V., Polley, C., Generalov, A., Fedorov, A. V., Güttler, M., Laubschat, C., Kliemt, K., Koroteev, Y. M., Chulkov, E. V., Kummer, K., Krellner, C., Usachov, D. Y. & Vyalikh, D. V. "Strong Rashba Effect and Different $f-d$ Hybridization Phenomena at the Surface of the Heavy-Fermion Superconductor $CeIrIn_5$". *Adv. Electron. Mater.* **8**, 2100768 (2022).

6. Fedorov, A. V., Poelchen, G., Eremeev, S. V., Schulz, S., Generalov, A., Polley, C., Laubschat, C., Kliemt, K., Kaya, N., Krellner, C., Chulkov, E. V., Kummer, K., Usachov, D. Y., Ernst, A. & Vyalikh, D. V. "Insight into the Temperature Evolution of Electronic Structure and Mechanism of Exchange Interaction in EuS". *J. Phys. Chem. Lett.* **12**, 8328–8334 (2021).

7. Kim, T. K., Pervakov, K. S., Evtushinsky, D. V., Jung, S.W., Poelchen, G., Kummer, K., Vlasenko, V. A., Sadakov, A. V., Usoltsev, A. S., Pudalov, V. M., Roditchev, D., Stolyarov, V. S., Vyalikh, D. V., Borisov, V., Valentí, R., Ernst, A., Eremeev, S. V. & Chulkov, E. V. "Electronic structure and coexistence of superconductivity with magnetism in $RbEuFe_4As_4$". *Phys. Rev. B* **103**, 174517 (2021).

8. Schulz, S., Vyazovskaya, A. Y., Poelchen, G., Generalov, A., Güttler, M., Mende, M., Danzenbächer, S., Otrokov, M. M., Balasubramanian, T., Polley, C., Chulkov, E. V., Laubschat, C., Peters, M., Kliemt, K., Krellner, C., Usachov, D. Y. & Vyalikh, D. V. "Classical and cubic Rashba effect in the presence of in-plane $4f$ magnetism at the iridium silicide surface of the antiferromagnet $GdIr_2Si_2$". *Phys. Rev. B* **103**, 035123 (2021).

9. Poelchen, G., Schulz, S., Mende, M., Güttler, M., Generalov, A., Fedorov, A. V., Caroca-Canales, N., Geibel, C., Kliemt, K., Krellner, C., Danzenbächer, S., Usachov, D. Y., Dudin, P., Antonov, V. N., Allen, J.W., Laubschat, C., Kummer, K., Kucherenko, Y. & Vyalikh, D. V. "Unexpected differences between surface and bulk spectroscopic and implied Kondo properties of heavy fermion $CeRh_2Si_2$". *npj Quantum Mater.* **5**, 70 (2020).

10. Usachov, D. Y., Tarasov, A. V., Schulz, S., Bokai, K. A., Tupitsyn, I. I., Poelchen, G., Seiro, S., Caroca-Canales, N., Kliemt, K., Mende, M., Kummer, K., Krellner, C., Muntwiler, M., Li, H., Laubschat, C., Geibel, C., Chulkov, E. V., Fujimori, S. I. & Vyalikh, D. V. "Photoelectron diffraction for probing valency and magnetism of $4f$-based materials: A view on valence-fluctuating $EuIr_2Si_2$". *Phys. Rev. B* **102**, 205102 (2020).

11. Usachov, D. Y., Güttler, M., Schulz, S., Poelchen, G., Seiro, S., Kliemt, K., Kummer, K., Krellner, C., Laubschat, C., Chulkov, E. V. & Vyalikh, D. V. "Spin structure of spin-orbit split surface states in a magnetic material revealed by spin-integrated photoemission". *Phys. Rev. B* **101**, 245140 (2020).

12. Usachov, D. Y., Nechaev, I. A., Poelchen, G., Güttler, M., Krasovskii, E. E., Schulz, S., Generalov, A., Kliemt, K., Kraiker, A., Krellner, C., Kummer, K., Danzenbächer, S., Laubschat, C.,Weber, A. P., Sánchez-Barriga, J., Chulkov, E., Santander-Syro, A., Imai, T., Miyamoto, K., Okuda, T. & Vyalikh, D. "Cubic Rashba Effect in the Surface Spin Structure of Rare-Earth Ternary Materials". *Phys. Rev. Lett.* **124**, 237202 (2020).

13. Schulz, S., Nechaev, I. A., Güttler, M., Poelchen, G., Generalov, A., Danzenbächer, S., Chikina, A., Seiro, S., Kliemt, K., Vyazovskaya, A. Y., Kim, T. K., Dudin, P., Chulkov, E. V., Laubschat, C., Krasovskii, E. E., Geibel, C., Krellner, C., Kummer, K. & Vyalikh, D. V. "Emerging 2D-ferromagnetism and strong spin-orbit coupling at the surface of valence-fluctuating $EuIr_2Si_2$". *npj Quantum Materials* **4**, 26 (2019).